Motion Estimation from Tagged MR Images and Application to Cardiac Strain Evaluation and Functional Analysis of Ocular Tissues

by

Ming Li

A Dissertation submitted to the Graduate Faculty of
Auburn University
in partial fulfillment of the
requirements for the Degree of
Doctor of Philosophy

Auburn, Alabama
Dec 12, 2015

Keywords: Motion analysis, tagged MRI, cardiac strain, ophthalmology

Approved by

Thomas S. Denney Jr., Professor of Electrical and Computer Engineering
Stanley J. Reeves, Professor of Electrical and Computer Engineering
Jitendra K. Tugnait, Professor of Electrical and Computer Engineering

Abstract

Tagged MRI is a magnetic resonance imaging technique that has been widely applied to tissue functional evaluation, especially the myocardium. Unlike traditional anatomical imaging methods, tagged MRI spatially encodes the motion of underlying tissue by modulating the longitudinal magnetization periodically before deformation. The visual appearance is dark strips or grids that follow along with the tissue motion. Therefore, by investigating the apparent changing of the tag pattern, one can estimate the deformation pattern and mechanical properties of the target tissue. Previous motion estimation methods either manually or automatically reconstruct the deformation field from tagged MRI. However, most of them have limitations such as low computational efficiency or accuracy, or the inability to reconstruct a 3D deformation. In this dissertation, we develop three motion estimation methods that reduce manual intervention rate and computation time, while retaining a relatively high accuracy.

The first introduced method improves a previous unwrapped phase-based method by automatically optimizing the branch cut configuration using simulated annealing. Then a quality-guided phase unwrapping follows after the application of branch cuts to unwrap the harmonic phase image. The unwrapped phase values provide displacement measurement and can be used to reconstruct a 3D deformation field. Although this method reduces manual intervention greatly compared to the previous manual method, it is time consuming. Then, we introduce a second method, which unwraps the harmonic phase image using integer optimization with graph cuts. The resulting unwrapped phase is both spatially and temporally smooth, as we assume the underlying deformation is continuous and smooth. We also use a dynamic model with a Kalman filter to improve the performance on biventricular studies. This method largely reduces the computation time and is highly automated. The third method is a feature-based method that first detects tag points using Gabor filter banks. Then this method classifies detected tag line points using a graph cuts method. Displacement measurements can be computed from the classified tag points and these measurements are interpolated to yield a denser 3D deformation field.

Besides cardiac application, we also used tagged MRI for functional analysis of ocular tissues, including extraocular muscles and vitreous humour. For study of the extraocular muscles, we evaluated and compared the strain patterns of different muscle layers (global and orbital) under controlled eye motion. For the vitreous humour study, we measured the deformation pattern of the vitreous humour, and we quantitatively evaluated the shear strain within the vitreous cavity. The results suggest a significant influence of the geometry and inhomogeneity in the material properties of the vitreous humour on its deformation pattern.

Acknowledgments

I would like to thank Dr. Thomas S. Denney Jr., my PhD advisor, for his professional guidance and consistent support. During my study at Auburn he has shared me with tremendous insightful suggestions and ideas, as well as invaluable experience that helped me in becoming a good researcher. His responsible and dedicated working attitudes inspired and influenced me in many ways. I have learned to be prudent about my own work and to be organized for my projects. With a considerate personality, he spared no effort to fulfill my research and career targets. It has been a great honor and pleasure to work with him.

I greatly thank my other two committee members, Dr. Stanley J. Reeves and Dr. Jitendra Tugnait, for providing professional insights and help for my research work development. I have taken classes from both of them. The coursework was enlightening and the discussion was in depth. I found the classes to be enjoyable as most of the talking broadened my views and drove me to reach out for more research opportunities. I would also like to thank Dr. Gopi Deshpande for his expertise in statistics and machine learning that I have benefited from during our seminars.

I would also like to express my gratitude to other staff members at AU MRI research center: Dr. Ronald J. Beyers, for his professional guidance on MRI experiment and machine operation; Dr. Nouha Salibi, for her technical support for the optimal performance of our machines; and Mrs. Julie Rodiek, for her timely coordinating of scan documents and event planning.

I appreciate the collaborative work with Dr. Mark S. Bolding and Dr. Paul Gamlin at University of Alabama at Birmingham. With their professional knowledge and suggestions on ophthalmology, our experiments have been successfully conducted with meaningful results. Parts of my research work could not be fulfilled without the help from them.

My thanks also goes to my friends who came to Auburn before me: Wei Zha, Chun G. Schiros, Bharath Ambale Venkatesh, Wei Feng, Wenting Deng, and Tao Ma, and those who came at the same time or after: Chenxi Hu, Nikhil Jha, Xiaoxia Zhang, Karthik Sreenivasan, Sreenath Pruthvi, Wenjing Yan, and Sinan Zhao. We shared each other with stories and experience, and I have learned a lot from them.

Finally, I would like to thank my family for unconditional support and love. They always encourage me and respect my decisions. My special thanks go to my dear wife, Wenyue Wang, for illuminating my life with caring, tolerance, happiness and surprise. I am grateful to have her by my side and walk through difficulties in life.

The research in this dissertation was supported in part by NIH grant 1R01HL104018.

Table of Contents

List of Figures

List of Tables

Chapter 1

INTRODUCTION

Magnetic resonance imaging (MRI) is a widely used medical imaging technique for the purposes of both clinical application and research experiment. Compared to other well established medical imaging methods like CT, ultrasound and PET, MRI provides images with high spatial resolution and is non-invasive and non-radioactive, which makes it potentially a safer medical diagnostic tool. On the other hand, the development of imaging techniques such as anatomical MRI, tagged MRI, functional MRI (fMRI), and diffusion tensor imaging (DTI) has made MRI applicable to a variety of situations, including soft-tissue imaging, dynamic motion measurement and function evaluation. Due to a relatively high spatial resolution and the ability of encoding displacement or velocity during the motion of tissue, MRI has been considered a gold standard method for regional deformation measurement.

Among the MR imaging techniques, tagged MR imaging is one of the most widely used spatial encoding methods that can be applied for qualitative and quantitative evaluation of the regional deformation pattern. MR tagging uses a special pulse sequence to spatially modulate the longitudinal magnetization, prior to image acquisition using traditional cine MR. Tagged MR images have periodic dark strips or grids as a result of the modulation. The modulated signal is a material property and will change accordingly with the deformation of the tagged tissue. The appearance of this change is denser tag lines with smaller tag spacing while tissue is contracting or sparser tag lines during expansion. By investigating the deformed tag lines one can measure the underlying deformation pattern. However, a quantitative measurement of the deformation field not only can reveal the regional motion with higher precision, but also can be used for comparison and generalization with a large dataset.

There are numerous motion estimation methods developed for quantitative measurement using tagged MR images. While some of these methods try to solve the problem within the spatial domain, others utilize the image within frequency domain after Fourier transformation. Most of these methods computed the material displacement at sparse and nonuniform points, like tag points along tag lines and tag intersections. Therefore, an interpolation based on smoothness assumptions after the displacement measurement is necessary in order to get a dense displacement map. For a single slice of tagged images, a 2D dense deformation field can be estimated or computed. For a tagged MR study composed of several slices with different orientations, a 3D dense deformation field is generated based on the sparse displacement measurements. A typical situation for the 3D motion estimation is the cardiac tagged MRI, which is used for the myocardial function evaluation. For either 2D or 3D deformation field, a corresponding strain can be computed, which reflects the regional tissue deformation pattern like contraction, expansion and shearing.

Despite the fact that the motion estimation method using tagged MR images has been intensively developed in recent decades, most of the widely used techniques have their own limitations that prevent the estimated motion field from being perfect. One such limitation is the probability of local optima. This is often a problem for feature-based methods, whose accuracy relies on the detection and tracking of the true tag features like tag lines or intersections. Once the algorithm mistracks the tag feature, either due to the grayscale intensity ambiguity or a large interframe deformation, the estimated motion field becomes incorrect. Another type of limitation is the propagation error when tracking tag features from time to time. Since a material point can have a displacement component perpendicular to the image plane, the tracked tag features may disappear or reappear and the tracking errors will be exaggerated over time. Though some advanced methods have been proposed to overcome the above limitations, the processing time is too long for clinical application.

In this dissertation, we summarize some of these advanced motion estimation methods. Then three new methods are proposed that improve time efficiency as well as measurement accuracy. The first motion estimation method uses a phase unwrapping technique with simulated annealing for the displacement measurement. The second method is also a phase unwrapping-based method, but the unwrapping process is achieved by an integer optimization technique. The third method uses a Gabor filter bank to extract feature tag points and a specially designed point classification algorithm to calculate the correspondence between deformed tag points and reference tag lines. For the last two methods, a combinatorial optimization problem was framed and a graph cuts technique was used for optimization.

Since MR tagging was originally introduced for cardiac motion analysis and later found extended applications like tongue imaging and skeletal muscle imaging, the major part of this dissertation will focus on a discussion of the myocardium motion using tagged MRI, which is a research area of long history and still under development. At the later part of this dissertation, we discussed the potential usage of tagged MRI for motion analysis of other tissues, which are the extraocular muscles and vitreous humour in the eye, specifically.

The remaining content of this dissertation is organized as follows. In this chapter, we briefly introduce the motion problems involved in cardiology and ophthalmology. Chapter 2 introduces the basis of tagged MR imaging and existing motion estimation methods. Chapter 3 presents the objectives of this dissertation. In Chapter 4, we exploite a computer-assisted branch cut placement method for harmonic phase unwrapping and deformation measurement, which is then applied to 3D+time biventricular strain reconstruction. In Chapter 5, we propose a phase unwrapping method based on integer optimization with graph cuts and dynamic model with Kalman filter and apply it to cardiac motion measurement. In Chapter 6 another motion estimation method using Gabor filter banks and a point classification algorithm is introduced for the application of cardiac analysis. Chapter 7 and Chapter 8 describe applications to measuring the deformation of ocular tissues. In Chapter 7, we use tagged MR imaging to measure deformation and strain in extraocular muscles. In Chapter 8, we use similar techniques to measure deformation and strain in the vitreous humour. In Chapter 9 we present conclusion drawn from this dissertation and discuss about future work.

1.1 Myocardial Mechanics

1.1.1 Heart Anatomy

The heart is a muscular organ which is responsible for receiving blood from the venous blood vessels at low pressure and imparting energy to the blood and pumping up the blood to the rest of body through the arterial blood vessels of the circulatory system [61]. The human heart has four chambers (Figure 1.1): two atria and two ventricles. The left atrium collects oxygenated blood from pulmonary veins, and this venous return passes to the left ventricle through the mitral valve. The left ventricle pumps the blood to the systemic circulation through the aorta. Deoxygenated blood flow from the venous system to the right atrium and goes into the right ventricle through the tricuspid valve. Then the right ventricle pumps the deoxygenated blood to the pulmonary artery and the lungs. The circulation is controlled by four heart valves: pulmonary, aortic, mitral, and tricuspid. The mitral valve and the tricuspid valve close and prevent blood from flowing back to the atria while ventricles deliver blood to the arteries. The pulmonary valve and the aortic valve control the blood flow from ventricles to arteries. The two atrioventricular valves have fibrous strands on their leaflets that attach to papillary muscles located on the respective ventricular wall. The papillary muscles contract while the ventricles develop pressure and the generated tension prevents the atrioventricular valves from bulging back and leaking blood into the atria.

The rhythmic heart muscle contraction and relaxation is controlled by the action potentials conducted across the heart. When action potentials are first generated with polarization of the sinoatrial (SA) node, they spread out across the atria and activate the atrial contraction. Then these electrical impulses are collected by the atrioventricular (AV) node located in the inferior-posterior region of the interatrial septum and the conduction through the AV node further excites the ventricular contraction. The electrical conduction from the AV node to ventricles is significantly slower than that within the atria, which allows the completion of the atrial contraction and relaxation before the ventricle contraction. The

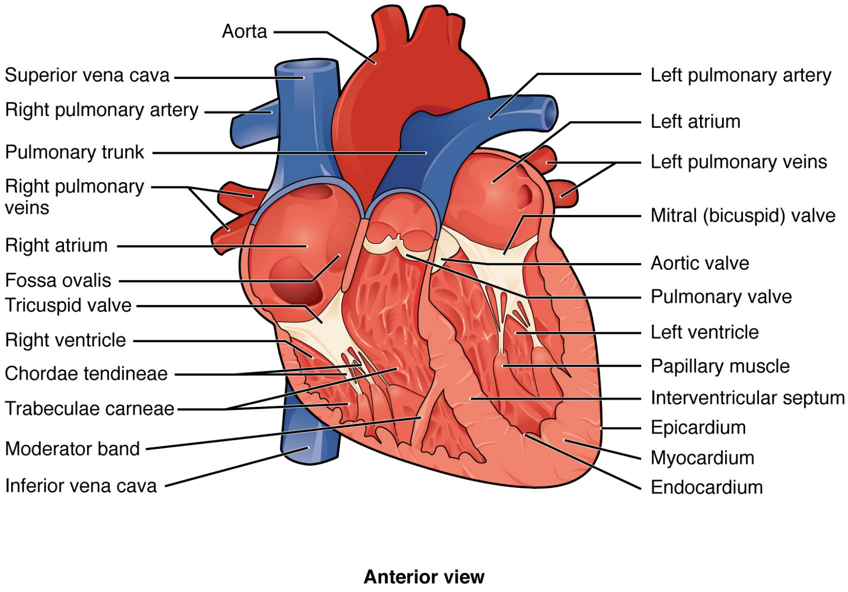

Figure 1.1: Human heart anatomy at anterior view [127]

excited potential difference can be traced by placing array of electrodes over specific regions of the body surface. The recorded diagram is called the electrocardiogram (ECG), which is an important clinical tool for diagnosing rhythm disorders, changes in electrical conduction, and myocardial ischemia and infarction. A typical cycle of the ECG is composed of several waves or peaks. The first wave called P wave represents the depolarization that spreads out from the SA node throughout the atria. The QRS complex following the P wave represents ventricular depolarization, and the R wave as the peak can be used as the indication of the ventricular contraction. Finally the T wave after the QRS complex represents ventricular repolarization.

The main functioning part of the human heart is the heart wall, which is composed of three layers [19]: the epicardium, the endocardium, and the myocardium. Among these three layers the myocardium in the middle is thickest and has the major function of contraction and relaxation. Through myocardial contracting the blood within ventricles can be pumped out. And the ventricles get filled up with the blood while the myocardium is under relaxation. Muscle fiber orientation of the myocardium is complex, as the muscle cells swirl and spiral around the chambers. There is a significant change of the fiber orientation from the ventricle base to apex, which results in a twisting contractile pattern of the myocardium. The epicardium is surrounded by coronary arteries and veins and the metabolism of the heart wall is achieved through the coronary circulation. When there is a blockage due to the coronary artery disease, ischemia of the myocardium will happen and a cardiac infarction will develop. Under this situation, the myocardium tissues become damaged and the myocardium with ischemia stops from functioning normally, followed by an impaired blood circulation.

1.1.2 Myocardial Motion

Cardiac diseases like myocardial ischemia will result in a function abnormality of the heart, which in turn can be identified and analyzed through different imaging techniques. Cardiac function is typically evaluated using two categories of indexes [124]: global and regional indexes. Global indexes include ejection fraction (EF), cavity volume, wall thickening, and myocardial mass [50]. These biomarkers are important indicators of cardiac diseases and can be evaluated using standard imaging techniques like ultrasound, CT and cine MRI. Once images are acquired using these techniques the myocardium contours can be drawn manually or automatically. The myocardium volume and ventricle volume are then estimated by using the segmentation results from all image planes. However, though global indexes can be used for identification and evaluation of some types of cardiac diseases, it lacks the ability of regional analysis. As a matter of fact, the quantitative analysis of the regional parameters like motion pattern and local strains may cast a light on the diagnosis of diseases and the evaluation of treatment effectiveness [135].

For myocardium with ischemia, the contractile function of the affected region is influenced, resulting in an abnormal motion of the heart wall during contraction [55]. The infarcted region can be so localized such that global biomarkers using traditional imaging technique are not adequate for a comprehensive analysis. For measurement of the myocardial motion in early times, very few methods exist except for the one that used implanted radiopaque markers and X-ray imaging to track these markers. However, this method was invasive and could not be conducted to human subjects. This problem continued until the advent of MR tagging technique [16, 136], which uses MR imaging and spatial tag modulation to place noninvasive markers to the soft tissue like myocardium. With the help of tagged MRI, deformation at the internal myocardium was observed and tracked for the first time. Following MR tagging, other noninvasive imaging techniques like DENSE [9], SENC [87], and zHARP [3] emerged, with the function of revealing regional properties of the heart wall.

1.1.3 Stress and Strain

Regional motion pattern of the myocardium is often represented by local stress and strain in a mechanical sense [13]. Stress is defined as the averaged force over area that neighboring particles exert on each other. Strain on the other hand is a differential deformation measurement relative to the reference position. Because the myocardial stress cannot be readily derived from the cardiac images, strain is more preferred as an index of the regional function of the myocardium, as it can be computed from the motion field of the heart wall and is closely related to the stress.

Computation of the myocardial strain is dependent on the coordinate system to be used. An orthogonal coordinate system like Cartesian coordinate system can be adopted. However strain tensors under Cartesian coordinate cannot be related to the regional geometry of the heart and therefore is not suitable for regional function analysis. A proper choice of the coordinate system should conform to the geometry or structure of the heart, such that the strain tensors have circumferential, longitudinal, and radial components. Another choice of the representation of the local strain tensor is to convert it to a fiber oriented coordinate, such that the three normal strain components are aligned along the radial, fiber and crossfiber directions (Figure 1.2 (a) [13]).

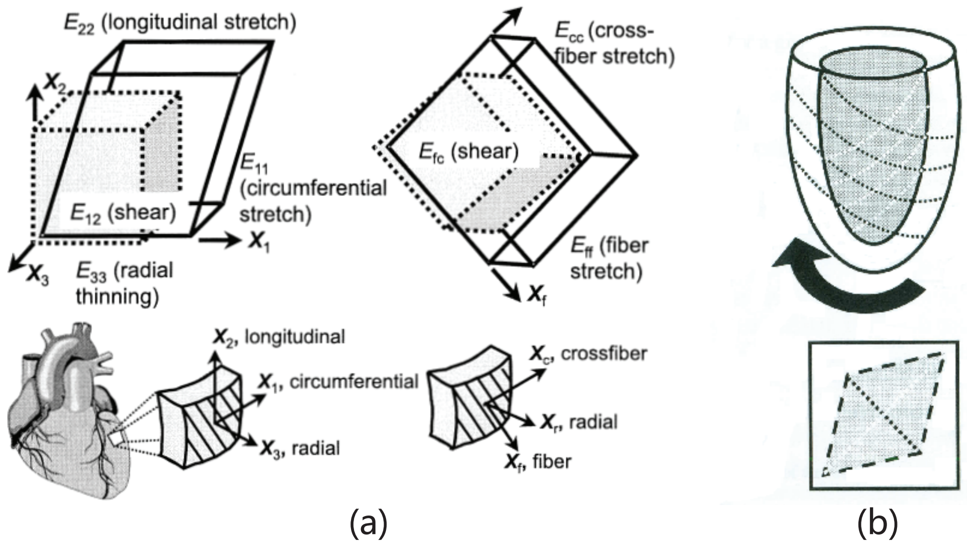

(a)

(b)

Figure 1.2: (a) Components of the strain tensor under different coordinate systems and (b) left-handed torsion during systole.

During the contraction of the ventricle, a positive radial strain E_{rr} occurs as a result of wall thickening, and the shortening along longitudinal and circumferential direction leads to negative longitudinal strain E_{ll} and circumferential strain E_{cc}. The principal axes of the strain do not usually coincide with the anatomical axes, and there is an angle between the maximal shortening principal axis and the circumferential direction [122]. The principal orientation is along the direction of subepicardial muscle fibers and is perpendicular to subendocardial fibers (Figure 1.2 (b)). This means that there are nonzero shear strain components. The conventional way of analyzing the principal strains from the strain tensor in anatomical coordinate is to use principal component analysis for a maximum principal strain $E_{\max}$ and minimum principal strain $E_{\min}$.

Another typical deformation related index besides strain is torsion, which is defined as the twisting of an object in response to a torque. Due to the whirling structure of the heart wall layers, the left ventricle undergoes a wringing motion while contraction, with an angle difference between rotations of the base and apex of the left ventricle. Unlike the myocardial strain, left ventricle torsion is a global index, measured as the rotation difference between apical slice and basal slice and devided by the distance between them. This measurement can be done using 2D images. However, because of the longitudinal shortening during contraction, structures within the same image plane do not come from the same material position, which is often the case for the basal part. Therefore, a torsion computed using a 3D deformation model may potentially reflects its true value.

Deformation analysis using strain and torsion as indexes are valuable for diagnosis, long-term disease development and remodeling identification, and evaluation of treatments. Altered mechanical properties are always related to the change of perfusion, structure, or metabolism. Many researches have been done to analyze the different deformation patterns in response to different pathologies, including acute ischemia and myocardial infarction [17, 83], hypertrophic [134] and dilated [133] cardiomyopathies, valvular disease [77], hypertension [44], and arrhythmias [78]. By using imaging technique like MR tagging, we have the ability to assessing the regional function of the heart in a quantitative way.

1.2 Dynamics of Ocular Tissues

1.2.1 Extraocular Muscle Motion

As tagged MRI and other techniques have been successfully applied to cardiac motion analysis, it is natural for one to think about their extension to other soft tissues. One of such extension is for the deformation measurement of the extraocular muscles of the eye. The movement of the eye is controlled by six extraocular muscles (EOMs), which are four rectus (medial, lateral, superior and inferior) and two oblique (superior and inferior) muscles, shown as Figure 1.3. The extraocular muscles cooperate in order to conduct the eye motion under a certain neural inputs and mechanical constraints. This coordination sometimes is impaired due to diseases or anomalies known as eye motion disorders. The most common disorder is strabismus, a condition in which a lack of binocular coordination between the extraocular muscles prevents the eyes from gazing at the same point. It is then evident that a comprehensive understanding of the extraocular muscle function can cast a light on a better treatment for strabismus and other eye motion disorders.

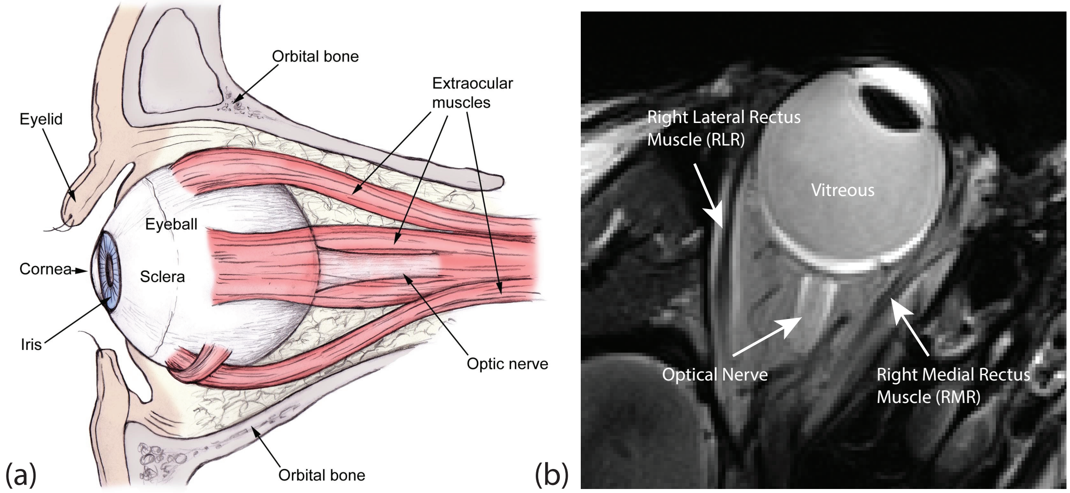

Figure 1.3: (a) Human eye anatomy showing extraocular muscles [128] and (b) T_2-weighted axial image of the right eye using MRI scanning.

There has been a prolonged debate about the mechanism of cooperative actions of the extraocular muscles in order to produce eye motion, and several models have been proposed for explanation [81]. Based on the observation of [82, 103], if the rectus extraocular muscles are constrained only at their ends, these muscles will sideslip widely about the globe, making eye rotation uncontrollable. This observation gave rise to a passive pulley model, as proposed in [80], that the muscle paths were directly stabilized by sheaths that functioned as pulleys elastically stabilized relative to the orbital wall. Later, another active pulley model was proposed in [35], within which the pulley was not assumed to passively support the muscle paths and to allow the muscles to slide freely through the pulley sleeves, but rather supposed to be connected to the orbital layer such that the pulley could move longitudinally.

Although the pulley model hypothesis has been supported by more and more reports from histological researches and developed imaging techniques, the exact mechanism of the model is not well understood. This inability results from the limitation of the traditional imaging methods, like CT and MRI, that the relative motion of the soft tissue pulleys with respect to the orbit, globe and extraocular muscles cannot be identified. However, a recent technique using tagged MR imaging was applied to eye imaging including the orbit, the extraocular muscles and other associated soft tissues [92, 93]. The acquired tagged MR images recorded the transmural deformation of the extraocular muscles. Based on this method, a tagged MRI scan using higher resolution may identify the relative motion of the orbital and global layers and may resolve the controversy about the pulley model.

1.2.2 Vitreous Humour Motion

Another soft tissue undergoes deformation during eye motion is the vitreous humour. The vitreous humour is a transparent gel-like liquid that fills in the vitreous cavity between the lens and the retina. The vitreous humour has certain refractional function that supports the vision of the human eye. On the other hand, the vitreous has a complex mechanical property that it supports the shape of the vitreous cavity, promotes the adherence between the retina and choroid, and acts as a barrier for transport of heat and molecules. The viscoelastic behavior of the vitreous humour is determined by the network of collagen fibrils and polyanionic hyaluronan [21]. When the eye moves smoothly or suddenly the vitreous humour deforms with a certain pattern. This rheological property of the vitreous humour is directly related to the regional viscoelastic properties.

Several studies (e.g. [112, 123]) have shown that the viscoelastic property changes along with the aging process. For elder people, the vitreous humour becomes less viscous or elastic compared to the young. Correspondingly, retinal detachment is more likely to happen to elder people. This observation can be explained by the assumption that the retina becomes more vulnerable when people age or that the tension exerted on the retina is the cause of the development of retinal detachment and this tension is higher when vitreous humour becomes less viscoelastic. Therefore, the relationship between the viscoelastic property and the stress of the vitreous humour on the periphery of the vitreous has been an important research area for better understanding the mechanism of the onset and development of retinal detachment.

Based on this assumption, many mathematical models have been proposed in order to investigate the deformation patterns of the vitreous humour with different viscoelastic properties and the shear stresses exerted on the retina (e.g. [24, 34]). However, these mathematical models all assume that the shape of the vitreous cavity to be spherical, and that the vitreous humour is homogeneous across the cavity. In fact, the vitreous humour is near spherical but has an indent near the lens. And the vitreous humour is inhomogeneous, with a higher viscoelasticity at posterior segment and lower viscoelasticity at the anterior segment as reported in [66]. Although the viscoelastic property of the vitreous humour has been studied *ex-vivo*, the values were subject to errors due to mass loss and microstructural changes after dissection [84, 117] and the mechanical property could not be conducted accurately. On the other hand, optical- [138] and ultrasound-based [123] methods did not count the inhomogeneity of the vitreous humour when investigating the deformation pattern under eye motion. As a consequence, an *in-vivo* deformation tracking method developed for the vitreous humour becomes critical and may reveal the vitreous motion pattern more accurately.

Chapter 2

Tagged MRI and Existing Methods for Motion Estimation

2.1 Tagged MR Imaging

Tagged MRI was first introduced in 1988 [136] and 1989 [16] with the application of myocardial motion analysis. Prospective ECG signal is used to predict the starting of the cardiac cycle and to trigger the tagging sequence. At the beginning of the pulse sequence a spatially modulated longitudinal magnetization is used to produce a dark strip pattern for one dimensional modulation or a grid pattern for two dimensional case. The dark strip or grid serves as a noninvasive marker and will follow the tissue during its motion. Figure 2.1 demonstrates the formation of the tag pattern using one dimensional tag modulation. We can see that tag lines are actually intersections of tag planes and the image plane. Due to T_1 relaxation of the magnetization, the tag profile will fade along with time. For cardiac analysis, most of the tag profiles persist until end-systole, and almost disappear at the end of the cardiac cycle. The most widely used tagged MRI is SPAtial Modulation of Magnetization (SPAMM) which produces a sinusoidal tag patterns. Figure 2.2 and Figure 2.3 are two examples of cardiac SPAMM images. The former shows images of long-axis view with four chambers of the heart present using line tags, and the latter shows images of short-axis view at mid-ventricle of the heart using grid tags. Notice that the tag line or grid follows along with the local material deformation and that tag fading becomes obvious after systole. Another MR tagging technique called complementary SPAMM (CSPAMM) was introduced [47], which utilized two SPAMM images that were out of phase by 180° and produced CSPAMM image by subtracting these two. By using CSPAMM the tag profile persists longer and untagged tissue gets suppressed.

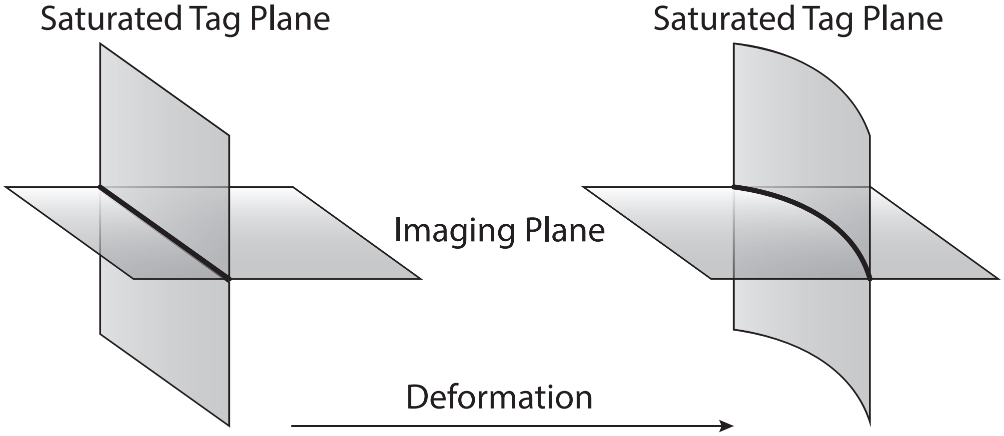

Figure 2.1: Demonstration of the tag line formation. Graph on left shows the tag line at its reference positions (undeformed) and the right one shows the deformed tag line.

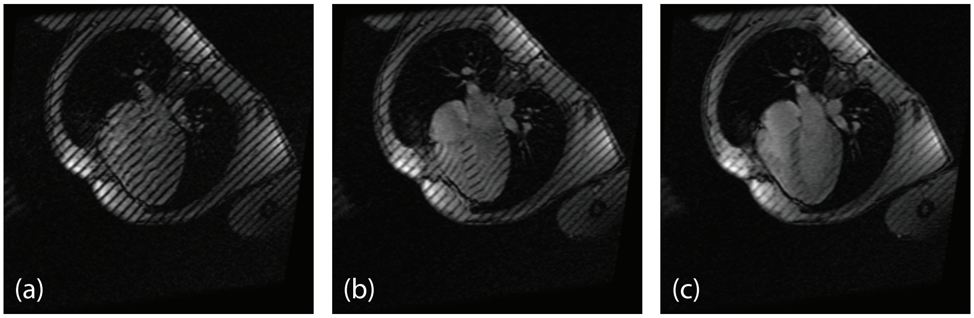

Figure 2.2: Cardiac SPAMM images of long-axis view with line tag pattern. Images were acquired at (a) 10, (b) 282, and (c) 646 ms, after the R wave triggering.

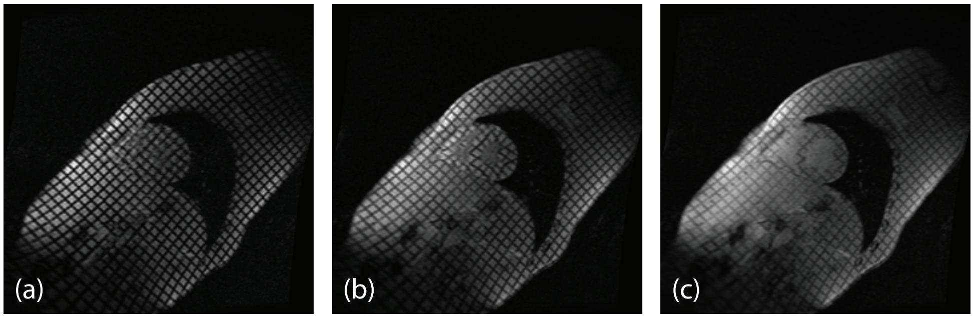

Figure 2.3: Cardiac SPAMM images of short-axis view with grid tag pattern. Images were acquired at (a) 0, (b) 270, and (c) 618 ms, after the R wave triggering.

Tagged MR images typically provide the 2D view of the tissue, like the myocardium. If a 3D visualization and deformation is needed then multiple views of 2D slices are required in order to reconstruct the 3D geometry and motion field. For cardiac imaging, a common approach is to acquire images from orthogonal planes (short-axis and long-axis). Parallel short-axis slices cover the ventricles from base to apex. The other set of slices are from a long-axis view, acquired either in parallel or radial configuration. For radial configuration the long-axis slices are usually separately by 30°. A typical pattern of tag modulation are coupled tag planes with orthogonal orientations (i.e. grid tags) that are perpendicular to the image plane for short-axis slices, and parallel tag planes for long-axis slices. Combining the short-axis slices and long-axis slices, a 3D geometry of the ventricles can be constructed. Also, the regional 3D deformation can be acquired from these three sets of tagging planes.

2.2 Segmentation

Segmentation is a prerequisite of motion estimation and analysis in most situations using tagged MRI. The segmentation step serves with two functions. First, by segmenting the region of interest (ROI) one can restrict the motion analysis within that region and exclude irrelevant parts out. In most cases, these irrelevant parts will contain noisy tag information or no information at all, imposing a serious problem to tag feature extraction and tracking. Second, for most of the model-based strain reconstruction methods, the segmentation result will be used for 3D model generation. With a 3D model, the coordinate of each tracked point can be transferred to a model-based coordinate system, which, among other things, allows strain tensors to be converted to an anatomically relevant coordinate system. Besides these two main functions, segmentation can be used by some algorithms to impose smoothness constraints using finite difference techniques.

Conventionally, the segmentation of myocardium or heart wall is achieved through delineating the endocardial and epicardial boundaries called the endo- and epi-contours. By using the segmented result from the contours, global cardiac function such as ejection fraction, wall thickening, and ventricle volume can be computed. Also these myocardium contours help with regulating the deformation pattern throughout the cardiac cycle. Because of the sharp contrast over the dark strips and grids, segmentation using tagged MR images is more difficult than using cine MR images, which mostly rely on the grayscale contrast over epicardial or endocardial boundaries. As a result, the automated segmentation algorithms are limited. Some of the methods automatically delineate endo- and epi-contours using the priori knowledge about the myocardium intensity, like in [39, 54]. However, the segmentation accuracy is subjected to the local grayscale information and therefore is prone to errors. Some other automated methods estimate the myocardium contours based on machine learning [97, 98], which requires a priori about the cardiac shape learned from the learning dataset. Aside from these automated segmentation methods, an alternative way is to manually draw contours for part of the image sequence, then register and propagate the contours for other time frames using automated algorithms [46]. This method assumes that the interframe deformation is small and the topology of the geometric structure is preserved throughout the cardiac cycle, which is often the case for cardiac imaging.

The semi-automated contour propagation method can potentially be applied to other tissues of interest, like skeletal muscles, tongue, and extraocular muscles of the eye. Due to the elastic nature of these tissues and the internal or external force exerted on them, there will be some deformation between images at adjacent time frames. However, the deformable model can still be applied because of the preserved topology.

2.3 Motion Estimation Methods using Tagged MRI

The motion estimation methods using MR tagging can be roughly classified into two groups [124]. The first group of methods are feature-based ones that utilize the deformed tagged features, like tag lines, tag line intersections (also called beads), and geometrically salient land markers. Some of the early works only track and visualize the tag features with no further processing. During the recent two decades deformable models or model-free methods are used to generate the dense motion field using interpolation of the measurements from the observed tag features, and then the strain was computed from the dense field. The second group of methods obtains a dense motion field or strain field without using the tracked tag features. This category includes the frequency-based method, optical flow methods, and registration methods. Along with these two main categories of methods, we listed in this dissertation a class of unwrapped phase-based methods, which utilize the phase information acquired from the frequency-based method and unwrap the phase map to eliminate the phase ambiguity. We will briefly introduce each of these methods in the following contents of this section. Because most of the motion estimation methods using tagged MRI were developed for myocardium function analysis, we will focus on their cardiac applications during this introduction. Despite the fact that some of these methods have the potential of extended applications to non-cardiac tissues, not all of them can be adopted without modification. Also the performance on other tissues with different motion patterns may differ among these methods.

2.3.1 Feature-Based Methods

Feature-based methods of motion estimation rely on the extracted and coordinated tag features, i.e., tag lines and tag intersections (beads). Due to the nature of tagged MRI, each tag line is the intersection of the corresponding tag plane and the image plane and the tag plane will move according to the underlying myocardial motion. Then, by investigating and tracking tag lines one can obtain the 1D displacement at each tag point along the normal direction of the undeformed tag plane. For tagged MR images with grid tags, since each tag intersection is the intersection of the two orthogonal tag planes and the image plane, the tracked tag intersections yield 2D displacements parallel to the image plane. In summary, the very first step of all feature-based methods is tag feature tracking.

Tag feature tracking is critical to the motion reconstruction as the accuracy of the tracked tag points (at tag lines or intersections) has direct influence on the reconstructed motion field. There have been multiple tag feature extraction and tracking algorithms. [54] preprocessed the tagged images using morphological filtering, then detected myocardial contours with the gradient information from the filtered result and tracked the tag lines by matching an intensity template of the tag profile to the data. Tag lines and intersections can also be tracked with active contours, or snakes [14]. The tag lines or intersections are initialized with B-splines or coupled B-splines at the undeformed positions. Then the B-snakes deform to the next time frame by attracting the snakes to the local intensity minimum and preserving the smoothness of the snakes at the same time. Tracking of the snakes can be embedded implicitly with a B-spline solid [31, 101]. With this method, each tag plane is modeled as an isoparametric plane defined from the B-spline solid. The external energy attracts the solid to align the isoparametric planes and the intensity valleys from the tagged images, and the internal energy penalizes the large bending and contraction or expansion of the solid. [39] used stochastic modeling of the tag profile to track tag lines. The probability that the candidate point belongs to a true tag line is evaluated with a likelihood function. Then the tag point candidates are optimized by minimizing a snake-like energy function which is defined as the sum of the negative likelihood function and the internal energy. Although the snakes algorithm is easy to implement, it is likely that the snakes be attracted to local minimum or other tag positions that are not part of the tracked tag lines. Therefore a manual intervention is highly recommended after the automated processing. This problem is partly caused by the noises present within the myocardium and the intensity ambiguity of different tag lines. To overcome this imperfection, [29] extracted the tag intersections using Gabor filter bank and tracked the intersection points from the current time frame to the next using a robust point matching algorithm (RPM). This method is more robust compared to the snake method as the tracking is accomplished by optimizing the transformation field that aligns the two intersection point sets.

One subset of these feature-based methods uses sparse tag features, which are intersections of the three orthogonal tag planes, to demonstrate and visualize the myocardium motion, as the tag line or the intersection point is a material feature and follows along with the tissue under deformation. However, the deformed tag line can only reveal its 1D displacement, which is the projection of its 3D displacement on the normal direction of the tag plane. Similarly, the 2D displacement from the tag intersection is the projection on the image plane. As a result, the three orthogonal tag planes have to be reconstructed before the intersection of each triplet of planes can be computed. In [59], a 3D deformation measurement method was proposed, which computed tag beads by reconstructing the tag plane using a thin-plate spline and determined the tag intersections from the reconstructed tag planes. Because an analytic solution for the intersection using thin-plate splines is intractable due to the complexity of the logarithm terms in the spline equations, the computation was done in an iterative way. Figure 2.4 shows the demonstration of tag plane intersections. A similar method was proposed with a higher computational efficiency [12]. Instead of representing the tag plane using thin-plate spline, the author utilized parameterized B-spline for interpolation. Compared to [59], this method uses fewer control points for tag plane fitting and therefore the intersection computation is much easier. 3D trajectories of tag features can also be computed without tag plane reconstruction. [109] used slice-following CSPAMM (SF-CSPAMM) technique to compensate for the through-plane motion. For in-plane motion the tag intersections were tracked using HARmonic Phase (HARP) from the tagged images, which we will talk about later.

The main disadvantage of these methods is that only sparse tag features can be obtained and the strain reconstruction based on the dense motion field becomes impossible. Although the observation of tag features can potentially improve using denser tag lines or grids, this will inevitably impose a challenge to the MR scanner as a higher magnetic gradient is required for magnetization modulation. Also, if the tag spacing is too small, tag lines can merge together when the myocardium contracts. Another limitation is that the tag plane reconstruction and computation of tag intersections are inefficient and time consuming.

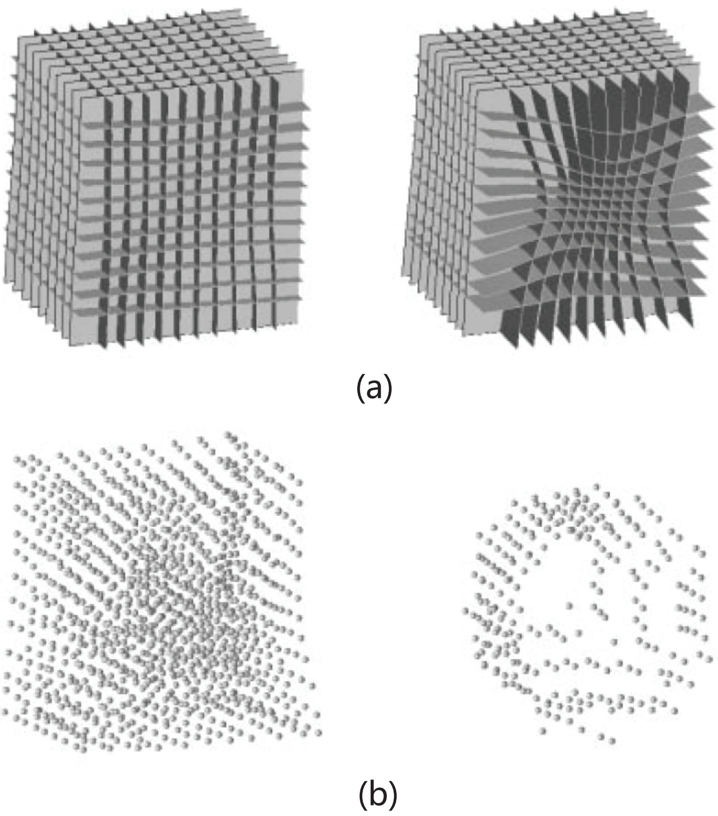

Figure 2.4: (a) Orthogonal tag planes with small deformation (left) and large deformation after myocardial contraction (right). (b) Tag plane intersections in the region of interest (left) and in the left ventricle (right) [59].

Instead of a sparse representation of the deformation field, a dense deformation field is preferred due to both the capability of quantitative assessment of regional function and the potential of intra-subject comparison and classification. In order to compute a dense deformation field, a parametric or nonparametric interpolation based on displacements observed at deformed tag points is required. For parametric interpolation, a deformable model is often used. For nonparametric interpolation, the deformable model is not required and therefore the assumption of geometry of the heart wall is not necessary [40].

The deformable model-based methods can be roughly classified into three broad categories, depending on the model used. The first class of methods use finite element model (FEM) to interpolate the motion field [56, 89, 131]. A typical FEM method consists several steps. First, the myocardium contours are partitioned and a geometric mesh based on the contour partitioning is generated. In this way, the myocardium is divided into multiple elements and the material property inside each element is controlled by element parameters (nodes) through the finite element shape functions. Then, the volumetric deformable model is deformed under the external force imposed by the distance between current parametric tag planes or tag lines to the observed ones of next time frame. [131] used the normal distance between model tag lines and image tag lines for external force computation. At the undeformed time, intersections of element subdivisions and tag planes are computed, which are material surfaces and will deform as the model parameters change (model tags). Then the model tag line as intersection of the model tag triangle and image plane can be coordinated with element parameters. In [56], instead of using model tag lines, model tag surfaces were used to register to the reconstructed tag surfaces after deformation. Along with the external energy term, there is an internal energy which is defined as the stiffness of the deformable model. By minimizing the total energy the volumetric deformable model is registered to the deformed position that the model tag lines or tag surfaces align to the observed tag lines or surfaces. Figure 2.5 shows the generated mesh for the deformable model and the model surfaces at the undeformed time frame.

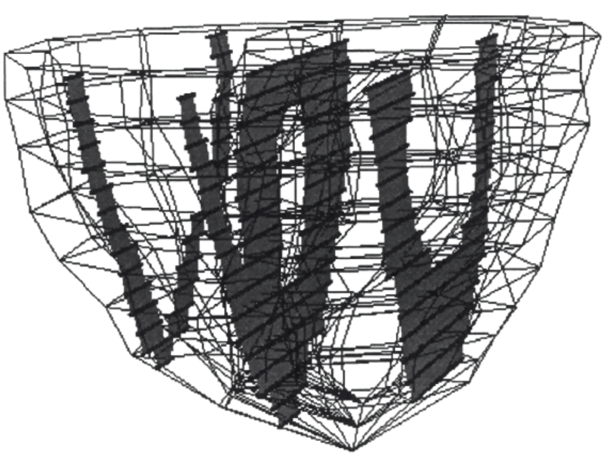

Figure 2.5: Biventricular mesh for the finite element model. Shaded surfaces are model surfaces at their undeformed positions. Material points are drawn in black. Each of the points is registered to the element in which it lies [56].

The second category of deformable model-based methods is spline-based methods. Among these methods the B-spline methods are the most popular ones [31, 58, 101]. A typical B-spline based interpolation method is using a B-solid, defined as a 3D tensor product B-spline, to represent the deformable heart. The coordinate of each material particle within the heart is controlled by the control points of the B-solid. The deformable B-solid is registered to the deformed position by applying an external force with implicit snakes that are determined within the solid and align them to the detected tag lines or intensity valleys. The internal energy is defined as a blend of first- and second-order derivatives of the B-solid, which is used to preserve smoothness and stiffness. Since the heart is modeled as a tensor product of B-splines, each material point at the undeformed time frame can be tracked to the deformed one and therefore the Lagrangian strain can be readily computed. Figure 2.6 is a demonstration of a 3D B-solid [101]. [119] improved the B-spline methods with 4D NonUniform Rational B-Spline (NURBS) as the deformable model. With this method, a control point set under polar coordinates (cylindrical or prolate spheroidal) is preferred over the one with Cartesian coordinates to represent the left ventricular myocardium. Parameterized models are built up for both the undeformed and deformed time frames separately.

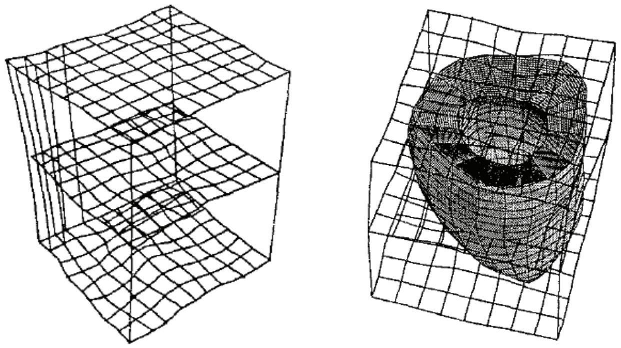

Figure 2.6: 3D B-solid after deformation (left) and heart volumetric model within the B-solid to represent myocardial surfaces [101].

The parameterized model at deformed time is then registered to the undeformed time using displacement information from tag planes, intersections of each triplet of tag planes, and intersections of contours and tag lines, resulting an Eulerian displacement field. Lagrangian fit can be acquired from densely sampling the Eulerian displacement field and performing a least square fit from the parameterized model at undeformed time to the deformed one. A 3D B-spline model based on cylindrical coordinate system was proposed in [36, 37], which was later improved with a prolate spheroidal B-spline model in [68], that shows to be more accurate in regard of the left ventricle geometry. Other spline-based deformable model can also be used for deformation interpolation and reconstruction, like thin-plate spline method proposed in [11], which used coupled B-snakes to track tag lines and used thin-plate spline to interpolate the motion field. Because of this, the reconstructed motion field and strain are limited to 2D.

Emerging in recent years, the third category uses a meshless deformable model to reconstruct the motion field [30, 125, 126]. The meshless deformable model (MDM) method reconstructs the dense motion field with the following steps [126]. First, tag intersections from the triplet of orthogonal tag planes are calculated to form the set of control points, and the myocardium contours are estimated using a machine learning-based segmentation method. Then a generic model of left ventricle built from MR images of healthy volunteers is used to deform and fit to the extracted contours. The global alignment is done with polar decomposition and the local refinement is done with Laplacian Surface Editing and Laplacian Surface Optimization. After the mesh is registered on the patient data, point cloud inside the left ventricle is sampled and forms the MDM. The model deforms with the external force provided by control points and fit them to the next time frame. Each point is not taken as a single particle but rather a part of the kernel that can interact with neighboring particles. The global deformation is optimized with the dynamics function and the local deformation is done by minimizing the local Laplacian coordinate, defined as the difference between the coordinate of the point and the average of its neighborhood, as we assume the neighborhood undergoes similar deformations. The deformation was computed iteratively until the control points match the target positions at the next time frame. Finally, the dense motion field and Lagrangian strain are reconstructed at each time frame.

Besides the deformable model-based motion reconstruction methods, there also exist interpolation methods that do not use any deformable model and therefore are not constrained by the geometry of heart. One of such alternatives was introduced as the discrete model-free method [40]. A set of 1D displacement from the extracted and tracked tag points are used to construct a linear system, where each displacement is the projection of the real 3D displacement vector along the tag plane normal, as shown in Figure 2.7. Since the linear system is under-determined with unknown 3D dense displacement vectors at the predefined grid positions, another spatial smoothness constraint needs to be incorporated into the linear system. By modeling the spatial variations of the dense displacement field and the tag detection errors as zero-mean random variables, the Fisher estimation framework can be adopted and solving the sparse linear system yields an estimation of the dense deformation field. Because the grid points at the deformed time frame do not correspond to regular material grid points at the reference time, the dense deformation field needs to be converted from spatial coordinate to the material coordinate using interpolation. The discrete model-free (DMF) method has the advantage that it does not assume the geometry of the target structure and therefore can be used with a variety of applications like motion reconstruction of the right

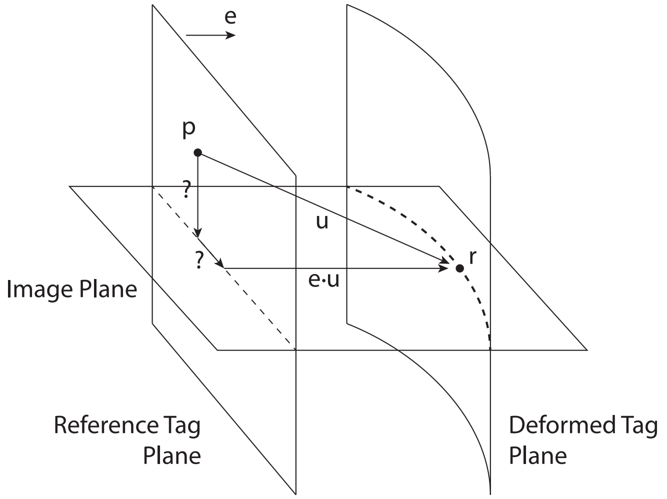

Figure 2.7: Displacement field measurement from planar tagged MR images. The material point p on the reference tag plane deforms to point r, which is on the intersection of image plane and the deformed tag plane. Only the projection of this displacement along the tag plane normal $e \cdot u$ is known [40].

ventricle, whose geometry is known to be complicated. The other advantage is that it has a relatively weak smoothness constraint, which makes it an ideal interpolation method for reconstruction of irregular deformation pattern. Also, the DMF method is more robust in the sense that it does not need to configure the control points as what are used with B-spline methods.

Another recent work without using a deformable model is the incompressible deformation estimation algorithm (IDEA) [75]. For this method, the normal displacement vector at each tracked material point is measured using the HARP tracking technique. Then IDEA applies a smoothing, divergence-free vector spline to interpolate velocity fields at intermediate discrete times such that the collection of velocity fields integrate over time to match the displacement components at the observed points. IDEA can give a dense 3D deformation field that matches the observation samples and conforms to the incompressibility property.

Despite the variety of feature-based methods with interpolation techniques, most of these methods require tag features be accurately detected and tracked, which is an error prone process. This is largely due to the periodic grayscale pattern of the tagged MR images, that makes the modeled tag lines or grids be trapped at unwanted positions. With the development of MR tagging, a small temporal resolution can be achieved for the image sequence. Therefore tag feature tacking for the left ventricle can be done with relative higher accuracy, by using a proper spatial-temporal smoothness constraint. However, when the potential deformation is large, like at the free wall of the right ventricle, the tag feature tracking method may have an error. One the other hand, the thin wall of the right ventricle and contrast over endocardium and epicardium will cause the tracking error, too. Therefore, within the context of the presence of a potential larger interframe deformation and heavier noise corruption, a non-tracking based motion estimation method may be preferred.

2.3.2 Frequency-Based Methods

Frequency-based methods are a large category that includes HARmonic Phase analysis (HARP), local Sine wave Modeling (SinMod), and Gabor filter banks. These methods deal with the motion tacking problem by looking at the frequency domain representation of the tagged MR images, as the tagged images can be treated as spatially AM-FM modulated signals. Among these techniques the most widely used is HARP [85, 86], mostly due to its fast and automatic nature. With this method, tagged images are first transformed to k-space using Fourier transform. Then the spectral peak is isolated using a bandpass filter. The harmonic phase is then retrieved by doing the inverse Fourier transform of the isolated spectrum and calculating angle information from the resulting complex image (Figure 2.8). The harmonic phase has the property that at each pixel the phase information is linearly related to the directional component of the material motion at that pixel, except that there exists a wrapping of the phase, restricting its value to be within $[-\pi, \pi)$. There are two techniques using harmonic phase, HARP tracking and HARP strain. HARP tracking is based on the fact that the phase information is a material property and will remain constant throughout the cardiac cycle for that material point. By tracking the phase information using harmonic phase images of two orthogonal orientations the 2D trajectory of each tracked point can be known. HARP strain, on the other hand, skips the deformation measurement and

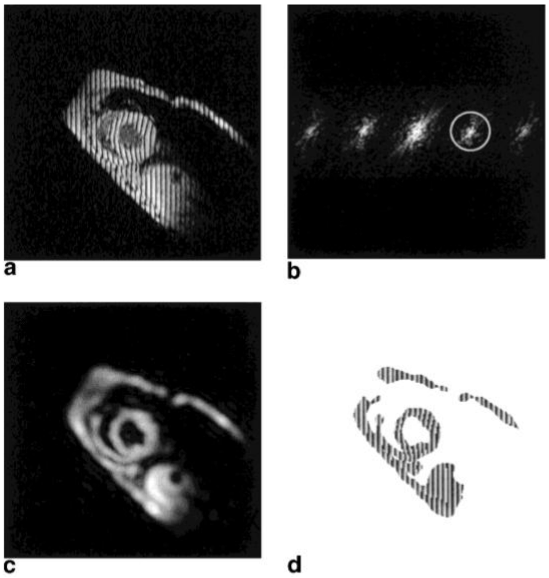

Figure 2.8: Demonstration of HARP. (a) SPAMM image with line tags. (b) Spectral peaks in k-space. (c) Magnitude of the complex image after invers Fourier transforming the isolated peak. (d) The harmonic phase image from the complex image [85].

computes the strain directly, by applying a modified gradient operator to the phase map. Though this method is fast and no tracking is required, the resulted strain is 2D and Eulerian.

Based on HARP technique, many other motion estimation and imaging methods were proposed. Since only the information near the spectral peak in k-space is needed, a fast-HARP pulse sequence [107] was developed, which only acquires a small region in k-space near the selected spectral peaks after tagging. By doing so, the image acquisition time can be reduced without influencing the ability of quantitative motion analysis. This method was later used by [2] with the application of real-time 2D cardiac strain. To overcome the disadvantage of HARP method that it can only deal with 2D in-plane motion, [88] used HARP images from both short-axis and long-axis tagged images and tracked the phase information for 3D motion reconstruction. [106] developed a true 3D tagging technique for 3D HARP analysis. However, the scan time is long and a sophisticated breath-holding technique is demanded. Other HARP-based imaging techniques try to decrease the imaging time, including the fast 3D-CSPAMM [105], zHARP [1], and HARP-SENC [108]. All these method can incorporate both in-plane and through-plane motion.

Local Sine wave Modeling (SinMod) [15] is another frequency-based method for analyzing the deformation field of tissue. Unlike HARP, which uses phase invariant condition to track the motion, SinMod uses both local spatial phase shift and local spatial frequency from the bandpass filtered images. By modeling the intensity at each point as a cosine wave front using the interframe displacement as the unknown variable, SinMod is able to compute the interframe displacement at each pixel, and is more accurate and robust against noise and artifacts than HARP. A comparison between SinMod and HARP was provided in [79]. [73] extended SinMod method by applying a robust and accurate center-frequency estimation algorithm to the original method. The center-frequency is computed by using mean-shift algorithm, which gives a rough estimation, and an original two-direction-combination strategy, which further enhances the accuracy.

While HARP method uses a bandpass filter with fixed window, Gabor filter can adjust its frequency related parameters according to the local image feature, and is therefore more appropriate for texture extraction. Actually, when there is a set of Gabor filters, or Gabor filter bank, the optimal filter for the regional feature can be selected based on the magnitude of response after convolving each Gabor filter to the image. The Gabor filter with highest magnitude of response tends to have parameters that best correspond to the local features. Based on this, [99] extended the 2D Gabor filter bank to 3D in order to extract and track deformed tag surfaces. [28] used a deformable model combining the phase information from Gabor filter bank, gradient information from original images, an intensity probabilistic model, and a spatio-temporal smoothness constraint to increase the accuracy of tag tracking. Another related paper [29] used the extracted tag intersection feature from Gabor filter bank and a robust point matching (RPM) algorithm to match the tag intersections between time frames. Then a meshless deformable model was used for dense motion estimation and strain reconstruction.

Frequency-based analysis has the advantage of less processing time and simpler mathematical model for implementation. Also, because the phase information is retrieved by bandpass filtering, it is more robust against noise compared to grayscale information in the feature space. However, due to the wrapping nature of the phase image, material point tracking based on phase invariant condition may not be accurate when a large interframe deformation is present. On the other hand, because of the tag fading the contrast-noise-ratio (CNR) decreases and the phase information is more likely to be corrupted by noise and artifacts. Combined with through-plane motion during heart contraction and relaxation the phase tracking method always leads to an exaggerated propagation error. To overcome this, further constraint and limitation need to be incorporated during the tracking process.

2.3.3 Optical Flow Methods

Optical flow method was first proposed in computer vision, which tries to track the motion of detected object from the time sequence. The basis of this method is the assumption that the intensity of the same material point will retain the same throughout time. Then the deformation components and spatial and temporal gradient of the local intensity can be incorporated into the same equation. The velocity field is solved based on the coupled partial differential equations (PDE). However, for tagged MR images the assumption of static intensity is violated because of tag fading. To compensate this, [94] introduced a term to account for the variable brightness of the stripes using the MR parameters T_1, T_2, and initial magnetization M_0. [45] used a Laplacian filter to compensate the intensity and contrast loss of the tag lines. In [129], a 3D optical flow method based on 3D tagged MRI was proposed.

Besides the original tagged MR images, phase images like HARP can also be used for optical flow computation [48]. [49] applied a multi-scale optical flow framework using HARP images, and reconstructed the zeroth- and first-order structure of the motion field. One of the advantages of using phase image like HARP instead of raw tagged image is that, the phase information from bandpass filtering is relatively robust against noise, and there is no need for intensity compensation.

One of the recent papers using optical flow is [25], which used a variational approach for optimizing the optical flow problem. For regularization, a total variation form of energy function was added with the purpose of denoising and discontinuity preserving. To improve the method, control points were automatically selected based on their phase stability. The enhanced variational method was shown to outperform the conventional variational method. And the result was shown to be more accurate than that from HARP. Another work presented recently is [8], which analyzed the tagged MR images using monogenic signal, the high dimensional extension of analytic signal. The monogenic signal incorporates both local frequency and local tag normal information, and is supposed to be changing smoothly across the space. In this method, the optical flow optimization was applied to the monogenic signal from the tagged MR images.

One problem of the optical flow method is that the accuracy of motion tracking relies on the smooth transition of the object between time frames. When there is large deformation or sharp transition between consecutive frames the optical flow can hardly track the motion correctly.

2.3.4 Non-rigid Registration Methods

The typical form of a set of tagged MR images is a sequence of tMRIs, composed of images from the beginning of the application of tag profiles to the end of cardiac cycle. Therefore the cardiac motion tracking can be treated as a 4D intramodality registration problem [76]. The image registration is to find the optimal transformation field that deforms the reference image to the target one. This can be done by maximizing the similarity term comparing the transformed reference image and the target image, along with a smoothness term incorporated within the transformation field. Based on the similarity metric used, the non-rigid registration methods can be classified in to two groups: one using intensity-based similarity measurement and the other one using entropy-based similarity measurement.

[65] used the intensity-based similarity criteria, which is measured as the squared difference between the target image and the warped reference image after registration. Combined with a regularization term the dissimilarity is minimized in regard of the deformation field. To improve the performance and speed of the algorithm, a multiresolution technique was used. The registration process was done for each pair of tagged images at adjacent time frames, and the deformation field from time to time could be computed accordingly. One of the disadvantages of this method is, because of the T_1 relaxation the intensity of tagged tissues is not constant throughout the time. Therefore the similarity measurement based on intensity can be problematic.

An alternative measurement is to use the entropy information. [104] registered the global deformation using affine transformation, then it used a free form deformation (FFD) based on B-spline to describe the local motion. Normalized mutual information (NMI) was used as the measurement of similarity. Registration was done by maximizing NMI as well as the smoothness of the transformation. In [27] this non-rigid registration method was applied for myocardial motion estimation, with a dual registration of both short-axis and long-axis images for 3D motion analysis. The local affine transformation was optimized by maximizing the NMI measurement. Then interframe deformation was added up for the final deformation field.

The advantage of non-rigid registration method is that it does not require the feature extraction step, and the registration process is fully automated. The disadvantage is that the registered result will sometimes be trapped at local minima due to either the intensity ambiguity or noises and artifacts. Since the registration result is not always accurate locally, a Bayesian estimation framework was introduced to improve the registered tag intersections [113]. By combining reversible jump Markov chain Monte Carlo (RJMCMC), the information about the heart dynamics, the imaging process, and tag appearance, this method was able to refine the detected tag features (tag intersections). The experimental result suggests an improved cardiac motion estimation.

2.3.5 Unwrapped Phase-Based Methods

As we discussed before in Section 2.3.2, for frequency-based methods like HARP, phase images instead of original tagged images are considered for the motion analysis. However, the phase information is wrapped, meaning that the true phase should be the wrapped phase plus an integer multiple of 2π. Phase unwrapping is to retrieve this true phase information by optimizing this integer, which we call *wrap count* in the rest contents of this dissertation. The phase unwrapping is an ill-posed reconstruction problem because the same wrapped phase value maps to an infinite set of unwrapped values. Consequently certain constraint or assumption has to be made in order for a successful unwrapping process. For a phase signal in the 1D case, a typical assumption is that the unwrapped phase is spatially or temporally smooth and discrete gradient is less than π. Starting from the seed point, the unwrapped phase at next temporal or spatial location is reconstructed by adding the modified gradient to the unwrapped phase of current point. The modified gradient is simply a wrapping of the original gradient that is restricted within the range $[-\pi, \pi)$. Though phase unwrapping is easy for 1D case with a simple assumption, the extension to 2D case can be problematic. This is caused by the fact that unwrapped phase at a non-seed point is dependent on the unwrapping path that we choose [53, 120]. If two unwrapping paths from the seed point to the target point encircle one or more discontinuity sources, then the final unwrapped values for target point will be different. The discontinuity source can be detected within a closed loop if the integration of the modified phase gradient along the loop is non-zero (Figure 2.9 [53]). This detection on 2D image can be specific if the loop consists 2×2 pixels, and the phase discontinuity is localized to the upper left pixel, also denoted as a *residue*. There are some ways to optimize the unwrapping process that yields an unique unwrapped result. One is to unwrap the phase image based on a quality map, which is computed from the gradient information of the image. After a pixel is unwrapped, one of its neighborhood having highest quality is then unwrapped. These steps guarantee that pixels with higher quality (or spatial smoothness) are unwrapped prior to those with lower quality. The other way is to use a

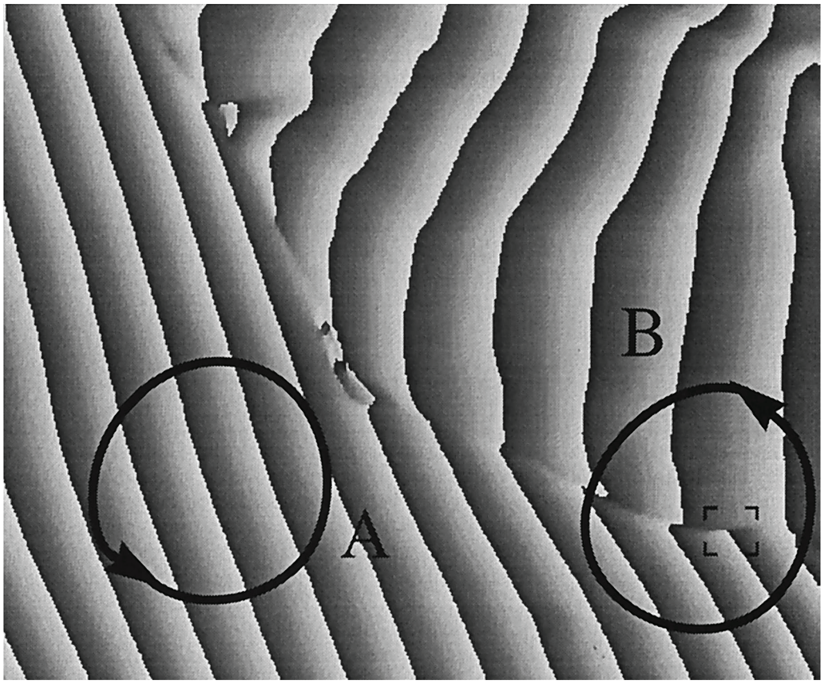

Figure 2.9: Phase map with discontinuity sources. Unwrapping along loop A yields zero, whereas loop B yields -2π, as loop B encloses a discontinuity source (in square) [53].

branch cut with two endings connecting to residues with different polarities. A positive residue is defined with an integration over the corresponding 2×2 pixel loop equals 2π and a negative one is defined with an integration of -2π. The branch cut cuts off certain regions along the line and therefore avoids any unwrapping path passing through it. These two methods can be combined for a better unwrapping result, as proposed in [120, 121].

Unwrapped HARP images share the same material properties with HARP images. In addition, due to the unwrapping nature, the phase value at each pixel becomes linearly related to its normal displacement from the undeformed position. Therefore, the 1D displacement value is readily available once the phase is correctly unwrapped. By using the unwrapped phase directly, there is no need for the phase tracking as used in HARP technique. In this way, the problem of error propagation can be avoided. [120] proposed an unwrapping method using manually placed branch cuts and quality-guided phase unwrapping and applied it to the left ventricular motion reconstruction and strain computation. The dense samples of 1D displacement at pixels within the image plane was retrieved from

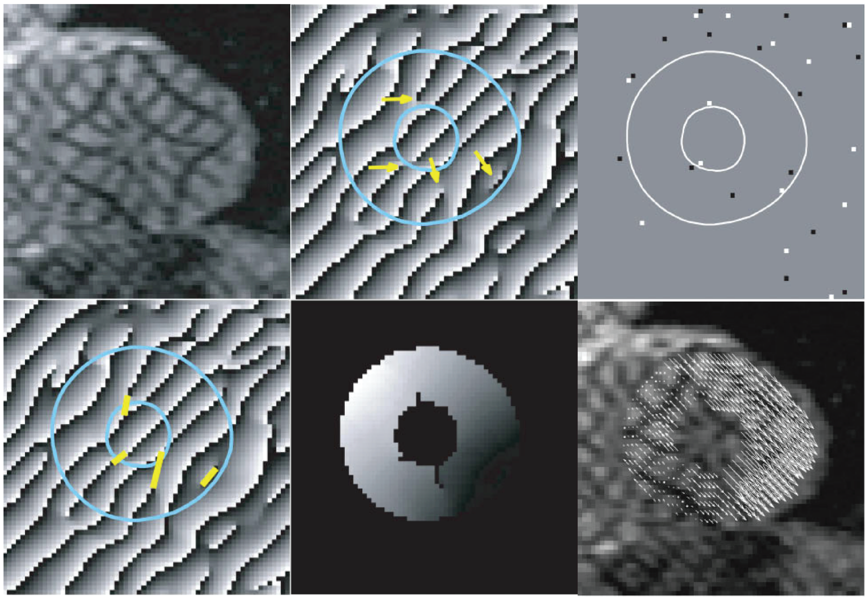

Figure 2.10: The procedure of phase unwrapping from a tagged MR image. Top left: raw tagged MR image of short-axis view. Top middle: corresponding HARP image with tag orientation of 45° as well as myocardial contours of left ventricle. Phase discontinuities (residues) are denoted with yellow arrows. Top right: positive (white) and negative (black) residues. Bottom left: branch cuts connecting positive and negative residues or residues and contours are shown in yellow. Only residues within the myocardium are resolved. Bottom middle: unwrapped phase with quality-guided phase unwrapping. Bottom right: computed 1D displacement along 45° orientation overlaid on the raw image.

the unwrapped phase and a prolate spheroidal B-spline model was used for 3D interpolation. A graphic user interface (GUI) was designed for users to place branch cuts interactively. Figure 2.10 shows the procedure of phase unwrapping for an image with short-axis view. This method combines the advantages from frequency-based and feature-based methods: a dense field with material properties and is robustness against noise, as well as the capability of 3D motion reconstruction. This unwrapping-based motion reconstruction method was further extended to biventricular strain analysis in [121], which used the discrete model-free (DMF) method for 3D motion and strain reconstruction, due to its versatile capability of strain reconstruction for irregular structures.

Although this motion reconstruction based on unwrapped phase information has many advantages over the traditional ones, the unwrapping process itself is prone to error. This is because a single difference of the selected unwrapping path may potentially influence a large region within the ROI and result in a great difference of the unwrapped values. Therefore the branch cuts need to be carefully placed in order to give out an accurate unwrapped phase map. [120, 121] used manually placed branch cuts that requires certain level of proficiency of the operator. In [10], an automated method based on temporal smoothness assumption was proposed for unwrapping left ventricle region of the HARP images from short-axis slices. The energy function defined as the sum of squared differences of the unwrapped values between consecutive timeframes were minimized by optimizing over the branch cut configuration using simulated annealing. Though short-axis images can be unwrapped automatically, the performance of this annealing-based method is inferior for long-axis images, due to a relatively larger amount of residues present in the myocardium and a larger interframe deformation that somehow violates the temporal smoothness assumption. Because of this, the authors set up the branch cuts automatically for short-axis images and placed the branch cuts manually for long-axis images.

Another unwrapped phase-based motion reconstruction method was proposed in [32]. In this paper, the unwrapped phase map was modeled with a B-spline surface, and was optimized by minimizing the sum of differences between the spatial gradients of absolute and wrapped phases, and the difference between the rewrapped and wrapped phases. Anchor points with known phase values were selected based on their spatial stability, and were introduced in the energy function to regulate the unwrapping. The authors also proposed a hybrid phase unwrapping technique that could select either B-spline based phase unwrapping method or HARP technique for the motion estimation. However, this B-spline approach for phase unwrapping has a problem that the rewrapped phase value is different from the wrapped phase due to the smoothing nature of splines. On the other hand, similar to the branch cut method, this phase unwrapping technique is still time inefficient, restricting its clinical applications.

2.3.6 Conclusion

All the motion reconstruction methods mentioned above have their own advantages and shortcomings. The feature-based methods first extract and track the tag features, which serve as sampled observations of the deformation field. Then a dense 2D or 3D motion field is reconstructed using interpolation techniques. Despite the capability of a dense motion field reconstruction on a higher dimensional space, which benefits the researcher with localization and diagnostic purposes, accuracy of the reconstructed motion field is highly dependent on the feature tracking result. Because of the grayscale ambiguity from the periodic nature of tagged images, the contrast over myocardial boundaries, and heavier noises over time, tag feature extraction and tracking can be challenging. On the other hand, most of the feature-based methods reconstruct the motion field with predefined deformable models that assume geometry of the left ventricle. This limits the capability of motion reconstruction for other tissues that have irregular shapes and geometries, like the right ventricle. Therefore, the nonparametric motion reconstruction method without a deformable model can be more versatile and suitable for researches involving tissues other than the left ventricle.

The frequency-based methods are good for their time efficiency and simple implementation. The Eulerian motion or strain from the frequency-based method is dense in the 2D space, while the Lagrangian motion or strain is limited to a coarser resolution. One the other hand, the capability of the reconstruction of a dense motion field in the 3D space is relatively limited with the frequency-based method. HARP tracking is a tracking-based method that seeks around the neighborhood for similar phase value from the current time frame to the next. This phase tracking is prone to error when large interframe deformation is present, like the time point between end-diastole (ED) and end-systole (ES) at which the myocardium contraction rate is the highest. This error happens because the true point in the next time frame is actually further from the current location and another point with the same phase value is mistakenly selected, due to a phase ambiguity.

Optical flow and non-rigid registration methods are automated in their nature. However, certain strong assumption about the motion field has to be made. The assumption of optical flow method is that the interframe deformation is small and the same material point preserves its intensity throughout the cardiac cycle, which is clearly not true. Although certain techniques like HARP may compensate for the intensity variation due to tag fading, exaggerated noise and tag-boundary interference can affect the accuracy of optical flow computation. A similar intensity assumption is made for non-rigid registration. The registration method relies on the comparison of intensities or entropies from target image and transformed image. With a periodic variation of the tag profile, the accuracy of registration is not always ideal. Also, registration-based method has a problem of over-smoothing, which further jeopardises the estimation accuracy.

Unwrapped phase-based method is a promising motion estimation technique in the sense that it can give out a dense displacement sampling rate, and that it does not impose a limitation about the interframe displacement, as opposed to other frequency-based methods and some of the tag feature tracking methods. On the other hand, because the unwrapped phase encodes the material displacement, it can be applied to the framework of feature-based method for dense 3D motion field estimation. However, certain problems of unwrapped phase-based methods need to be overcome in order to make them suitable for clinical purpose. One such problem is the time consumption. In [120, 121] the HARP was unwrapped with manually placed branch cuts, which requires intensive user intervention and proficiency. In [10] and [32], though the HARP images were unwrapped automatically, the time expended was not significantly reduced. The other problem is the accuracy of phase unwrapping. With the manual branch cut method, the branch cuts have to be placed carefully such that the resulted unwrapped phase is spatially smooth and conforms to the temporal consistency and the judgment of experienced researchers. For automated phase unwrapping methods, [10] used simulated annealing to minimize the phase difference between consecutive time frames. However, for HARP image with large amount of residues, the branch cut configuration may not be the global optima and therefore the unwrapped phase may be imperfect. In [32] the unwrapped phase was modeled as a B-spline surface, which suffers from the smoothing nature of splines and cannot perfectly fit to the true unwrapped phase.

In conclusion, despite the variety of existing motion estimation methods for tagged MR images, there are still many aspects need to be improved for a better performance and potential clinical application, i.e., higher time efficiency, higher accuracy, and less user intervention, etc. Before we go on with the exploration for better motion estimation approaches, we first introduce the objectives of this dissertation, which are stated in the following chapter.

Chapter 3

OBJECTIVES

The objectives of this research are to develop one or more motion estimation methods using tagged MR images that meet each of the following criteria:

1. Time efficient, so as to be applicable for clinical purposes;
2. Accurate and not over-smoothing the true motion field;
3. Highly automated and involves little user intervention;
4. Applicable to various kinds of tag data, including data with line tags and grid tags;
5. Capable of providing dense motion field and Lagrangian strain in 3D and 2D;
6. Requires little or no priori information about the geometries or dynamics of the investigated tissue.

Due to the popularity of frequency-based methods, like HARP and Gabor filter banks, and the capability of dense motion reconstruction with feature-based methods, it will be beneficial to combine these two techniques. With the frequency-based method, the displacement field is obtained at a higher sampling rate with a lower noise level. And with the feature-based method, a dense motion field can be reconstructed with or without a predefined model. In this research, we follow this intuition about the combination of frequency-based and feature-based methods, but we are more interested in developing new techniques for feature extraction and tracking. This is because, to a large extent, the accuracy of feature extraction and tracking determines the final accuracy level of the estimated motion field, hence the strain map. By developing a feature tracking method which is robust against both noise and local optima, we can expect the estimated motion field to be as accurate as possible.

The detailed objectives are as follows

1. Based on HARP technique, the unwrapped phase-based method is promising in that it is robust against large deformation and it can be used with other feature-based methods for dense motion and strain reconstruction. However, the phase unwrapping process with existing techniques is either time consuming or prone to unwrapping errors. We would like to introduce an improved phase unwrapping method which serves as an alternative to the existing ones and is both accurate and fast;

2. Due to the fixed window of bandpass filter, HARP cannot accurately track large deformation, like contraction, expansion, and rotation. In this regard, we would like to propose a feature tracking method and correspondingly a motion estimation method that is robust against large deformation and can be potentially applied to non-myocardial tissues;

3. We would like to extend the developed methods for ocular tissue analysis: extraocular muscle and vitreous humour deformation evaluation, specifically.

These objectives will be addressed in following chapters. In Chapter 4, we extended method in [10] to the biventricular case, with a modification to the energy function. This work was published as an abstract in ISMRM 2013 [72]. In Chapter 5, we proposed an automated phase unwrapping method using integer optimization with graph cuts and a cardiac dynamic model with Kalman filtering, and applied this method to biventricular strain reconstruction. Portions of this algorithm were published as a full paper in MICCAI 2014 [70] and as an abstract in ISMRM 2015 [71]. In Chapter 6, we proposed a motion estimation method which used Gabor filter bank for tag point extraction and a tag point classification algorithm to compute tag point correspondence. In Chapter 7, we applied the motion and strain computation method (DMF) [40] to tagged MR studies of the extraocular muscle to evaluate its deformation. This was published as an abstract in ISMRM 2014 [41]. In Chapter 8, we used the method in Chapter 6 and the DMF method to evaluate the motion pattern of the vitreous humour. This work was published as an abstract in ISMRM 2015 [69].

Chapter 4

BIVENTRICULAR CARDIAC STRAIN FROM UNWRAPPED HARMONIC PHASE: A COMPUTER-ASSISTED BRANCH CUT PLACEMENT METHOD

4.1 Introduction

As described in Chapter 2, several techniques have been developed to measure myocardium deformation and strain from the deformed tag pattern. These techniques include feature-based methods [39, 42, 54, 100], optical flow [38], non-rigid registration-based [27, 65] methods, and HARmonic Phase (HARP)-based methods [60, 74, 85, 86].

Among these methods the most popular one is HARP, which is fast and highly automated. In HARP analysis, the tag pattern deformation is measured by the local change in phase of the tag pattern. The HARP phase at a point in the image is a material property of the underlying tissue and can be tracked through the image sequence [85] or used to compute 2D strain [86]. The HARP phase, however, is wrapped because it can only be measured modulo 2π. This wrapping can cause tracking problems if a region of the tissue deforms more than one-half tag spacing, i.e., a phase shift of more than π between timeframes, which is more likely to happen during the right ventricle (RV) wall motion. Deformations of this magnitude are possible in both healthy and diseased hearts.

In [120], an unwrapped harmonic phase technique has been developed and was later on extended to biventricular strain estimation [121]. We refer to this method as manual Strain from Unwrapped Phase (mSUP). Compared to feature-base methods, displacement measurements from mSUP are denser than those obtained from tracking tag lines or tag grid intersections, and are not overly spatially smoothed like the result from non-rigid registration-based methods. Furthermore, due to its unwrapping nature it does not assume small motion as the HARP technique does. In [121], a discrete model-free (DMF) method [40] was later used to compute strain from the displacement measurements. DMF does not assume cardiac geometry and thus can accurately reconstruct LV and RV strain at the same time.

Phase unwrapping algorithm may have phase inconsistencies and fail at residues. A residue is defined as a pixel when integration of modified phase gradients around a 2 by 2 neighborhood of that pixel is non-zero. The modified phase gradient is the gradient wrapped to the range of $[-\pi, \pi)$. mSUP resolves these phase inconsistencies by using branch cuts [51] connecting from one residue to another with opposite polarity or from one residue to the border. Branch cut removes certain pixels on the phase image and guides the path of the unwrapping algorithm. mSUP uses manually specified branch cuts with a graphical user interface (GUI), which requires constant user interaction and is time consuming. Depending on the proficiency of operator and quality of tMRI images, the time required to analyze a biventricular study composed of $280 \sim 360$ tagged images would be from 1 to 2 hours.

In this chapter, a computer-assisted branch cut placement method is presented to compute 3D biventricular strain throughout the cardiac cycle using short-axis and long-axis HARP images. We refer to the proposed method as computer-assisted Strain from Unwrapped Phase (caSUP). This method is based on branch cut placement using simulated annealing, which was proposed for general-purpose phase unwrapping [53]. In [53], the author minimized the averaged branch cut length, which is a reasonable criterion in single-image unwrapping where phase inconsistencies are mostly caused by noise. In cardiac imaging, the shortest branch cuts might not be the best solution. So in this chapter, we use the property of temporal consistency of unwrapped phase for the energy function construction.

We used either exhaustive search or simulated annealing to automatically place branch cuts over HARP images, depending on the number of residues present. A quality-guided phase unwrapping was applied after branch cut placement. These two steps are fully unsupervised. After the automated phase unwrapping finishes, a test algorithm is used to detect any phase inconsistencies present on each phase image and manually placed branch cuts need to be applied to fix these inconsistencies. We used the DMF method to reconstruct 3D+time biventricular strain at each imaged timeframe of the cardiac cycle. Strain results were presented in normal volunteers, patients with LV resistant systemic hypertension (HTN), patients with pulmonary arterial hypertension (PAH), and diabetic patients with myocardial infarction (DMI). These results were also compared to strains from mSUP method and feature-based method [39, 40] to validate the performance of caSUP.

This chapter is organized as follows. The materials and methods are presented in Section 4.2. Experimental validation results on human studies and discussion/conclusion are presented in Sections 4.3 and 4.4.

4.2 Materials and Methods

4.2.1 Human Subjects and Data Acquisition

A cohort of 30 studies consisting of 10 normal volunteers (NL), 7 patients with pulmonary arterial hypertension (PAH), 8 patients with resistant systemic hypertension (HTN), and 5 diabetic patients with myocardial infarction (DMI) was used to validate the caSUP method. All human studies were approved by the Institutional Review Boards of both institutions and informed consent was obtained from each participant. Note that these pathologies were chosen to generate a diverse range of strains for validation purposes and not to compare strains between groups from a clinical perspective.

All participants underwent MRI on a 1.5 Tesla MRI scanner (GE, Milwaukee, WI) optimized for cardiac application. tMRI composed of 8-12 slices of a short-axis view and 6 slices of 360°radial long-axis view were acquired with a prospectively ECG gated fast gradient-echo cine sequence with grid tags spaced 7mm apart. Scanning parameters were: FOV=40x40cm, scan matrix=256×128, 8mm slice thickness, flip angle=10°, TE=4.2ms, TR=8.0ms, 20 frames per cardiac cycle, typical temporal resolution is 50ms.

4.2.2 Computer-Assisted Strain from Unwrapped Phase

Before phase unwrapping and cardiac motion estimation, the myocardial contours need to be delineated. We drew endo- and epi-contours at the end-diastolic and end-systolic time frames for each slice of images. Then the contours were propagated to other time frames using a dual-contour propagation method based on non-rigid registration [46]. The segmentation result defines the region of interest (ROI) of the myocardium, as well as provides regions for unwrapping, displacement measurement, and motion/strain reconstruction.

In the unwrapped phase (mSUP) method described previously in [120] and [121], branch cuts were specified by the user with a graphical user interface (GUI). In this research we propose a computer-assisted branch cut placement method which finds the optimal branch cut configuration that minimizes a certain energy function. In [53], the author used an energy function that minimized the averaged branch cut length. This is a valid way to unwrap images with discontinuity sources mostly caused by noise. However, in cardiac applications, the noisy region can be easily removed by applying myocardium contours. On the other hand, the length-minimized branch cut configuration does not take the priori knowledge that an unwrapped phase of myocardium should be spatially and temporally smooth.

In an early work [10], an automated branch cut placing method using simulated annealing was used for unwrapping HARP images. The energy function of the branch cut configuration was defined as the sum of squared difference between current unwrapped phase and the one at previous time. The optimal branch cut configuration was found by minimizing the energy function over candidate configurations using simulated annealing technique. Though this method works for left ventricle studies, it cannot be directly extended to biventricular case, and HARP images from long-axis view still need manually placed branch cuts for unwrapping due to a larger interframe deformation. To improve this, we define a new energy function that is robust against larger myocardial deformation. We start the design of the energy function by assuming the myocardium is incompressible during its deformation. Since the tag plane follows the heart tissue the myocardium volume between two neighboring tag planes will be constant. If we further assume that there is no or very small through-plane motion between two consecutive time frames –meaning that there is little tissue motion perpendicular to the image plane –the area of the myocardial region between two neighboring tag lines will stay the same from time frame to time frame. Although this is a relatively strong assumption, it is valid as long as the through-plane motion is gradual and the time gap between two frames is small.

There is another aspect of unwrapping with branch cuts that needs to be considered. When we apply myocardium contours, which masks out the non-cardiac tissue outside the epi-contour and the blood inside the endo-contour, there will be "holes" left, i.e., the LV and RV blood pools. Even though all the residues are resolved over the myocardium mask, phase unwrapping may still be path-dependent, and phase inconsistencies occur. Figure 4.1 shows how this situation happens. (a) and (b) show two branch cut configurations for the same HARP image. Note that branch cut in the bottom is the only difference between these two configurations. Though all residues are resolved by applying branch cuts, branch cut configuration in (a) gives out a successful unwrapped phase in (c), whereas configuration in (b) gives an unsuccessful one in (d). The artifact of unwrapping due to phase inconsistency is denoted in (d).

Let us define the wrapping function as

$$\mathcal{W}(\phi) = \mathrm{mod}(\phi + \pi,\ 2\pi) - \pi. \tag{4.1}$$

The gradient of true unwrapped phase ϕ could be represented as a modified gradient of wrapped phase ψ as long as we assume the discrete gradient of the true unwrapped phase in no larger than π

$$\nabla\phi = \nabla^{*}\psi = \begin{cases} \nabla\psi & \|\nabla\psi\| \leq \|\nabla\mathcal{W}(\psi+\pi)\| \\ \nabla\mathcal{W}(\psi+\pi) & \text{otherwise} \end{cases}. \tag{4.2}$$

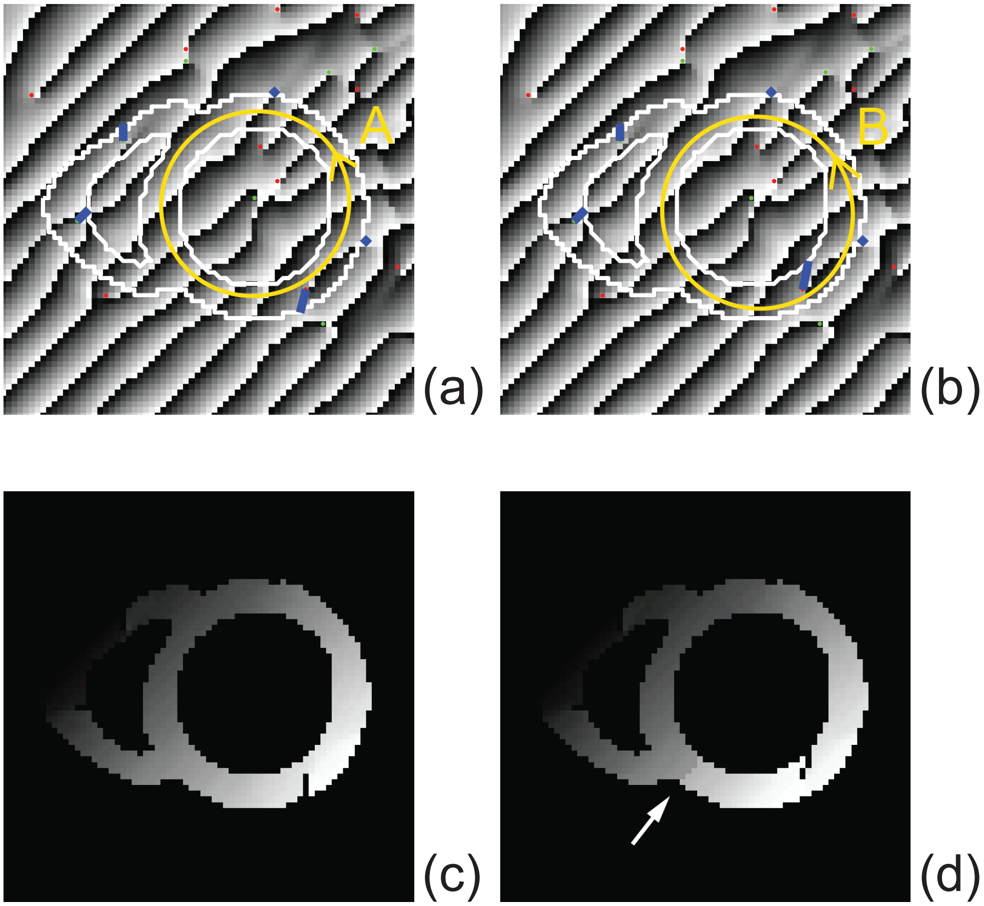

Figure 4.1: Different branch cut configurations ((a) and (b)) result in different unwrapped phase maps ((c) and (d)). White borders in (a) and (b) are myocardium contours. Residues are denoted in red (positive) or green (negative). Blue line segments are branch cuts connecting either positive and negative residues or residues and contours. Unwrapping artifact due to phase inconsistency is indicated with white arrow in (d). Notice the difference between the integrations of modified phase gradient along loop A and B.

Integration of the modified gradient of wrapped phase along a closed loop on the phase image should be zero if there are no phase inconsistencies. The gradient integration along loop A in Figure 4.1 (a) is zero while the integration along loop B in Figure 4.1 (b) is -2π. We can simplify this test by restricting the loop to be connected pixels of the endo-contour. Note that this situation can also happen to RV because RV blood pools in short-axis are also closed. We prevent this phase inconsistencies from happening by incorporating the gradient integration into the energy function with a high weighting factor.

The proposed energy function is then

$$E_t = \sum_{i=1}^{N_{\text{loop}}} \left| \int_{\boldsymbol{C_i}} \nabla^* \psi \right| + \lambda_1 \sum_j (n_{t,j} - n_{t-1,j})^2 + \lambda_2 \frac{1}{N_{bc}} \|R\boldsymbol{a_k}\|^2. \tag{4.3}$$

E_t is the energy at time frame t with current branch cut configuration. The first term is the sum of all integrations of modified gradient along closed loops as we have discussed previously. N_{loop} is the total number of loops which need to be tested, i.e., loops around LV and RV blood pools. $\nabla^* \psi$ is the modified gradient and $\boldsymbol{C_i}$ is the ith closed loop.

$n_{t,j}$ is the number of pixels inside the myocardium with the same *wrap count* value j at time t, where *wrap count* j is an integer defined by the relationship: $\phi = \psi + 2\pi j$. The second term minimizes the change of area between two neighboring phase discontinuity lines from time $t-1$ to t. Since phase discontinuity lines coincide with tag lines, this term essentially penalizes the change of area between neighboring tag lines as we assume this area staying the same as discussed above.

We introduced a third term, which is a modification of the widely used branch cut length energy. N_{bc} is the total number of branch cuts and $\boldsymbol{a_k}$ is the kth branch cut. R is a 2D transformation matrix:

$$R = \begin{bmatrix} \omega_1 \cos\theta & -\omega_1 \sin\theta \\ \omega_2 \sin\theta & \omega_2 \cos\theta \end{bmatrix},$$

where θ is the orientation of tag line defined from the protocol. If scaling factors ω_1 and ω_2 are the same, the matrix R is simply a rotational matrix that transforms the branch cut from Cartesian coordinate to the rotated coordinate, in which the x axis aligns to the tag line direction. Or we can set ω_1 and ω_2 to be different to scale certain axis in an elliptical sense. We set ω_1 to be less than ω_2 to encourage branch cuts be placed parallel to the tag line. This setting conforms to the observation that a good branch cut does not deviate from the tag line orientation by too much. We here choose $\omega_1 = 0.25$ and $\omega_2 = 1$ empirically.

The contribution of each term to the overall energy is controlled by two weighting factors λ_1 and λ_2. We will give a parameter sensitivity test later in Section 4.3 to decide their values.

After the application of branch cut configuration, the unwrapped phase ϕ is obtained by unwrapping the HARP phase (wrapped) using flood-fill quality-guided phase unwrapping [51, 120, 121]. We can use the exhaustive search method to explore all possible branch cut configurations to find the optimal solution that gives the minimal energy. However, as the number of residues increases, the number of possible configurations becomes prohibitively large ($N_{bc}!$ configurations). To overcome this problem we introduced a simulated annealing-based branch cut (SABC) placement method.

The simulated annealing-based branch cutting has been proposed for general-purpose phase unwrapping [53]. The method in [53], however, minimizes the branch cut length, while we minimize energy defined in Equation 4.3. A similar SABC method has been proposed in the early work [10].

The simulated annealing-based branch cutting [53] consists of

- An initial random configuration of branch cuts. In this research, the initial branch-cut configuration is chosen using nearest neighbor criteria, but any automatic algorithm can be used.
- An energy function E that describes the quality of a proposed solution. Energy function in Equation 4.3 is used.

- A generation mechanism that applies small changes to produce a new branch cut configuration. For each iteration k, a small change to the branch-cut configuration is applied based on mechanism in [10, 53]. The candidate configuration is chosen randomly. The energy E_t^{k+1} of the new configuration is then calculated, and the energy difference is

$$\Delta E_t = E_t^{k+1} - E_t^k.$$

- An acceptance criterion to decide whether the new configuration is accepted. The new configuration is always accepted if $\Delta E < 0$. Accepting a new configuration only if $\Delta E < 0$, though, means that the algorithm may be trapped to local minima. Therefore, increasing values of E are also accepted with a Boltzmann probability. The acceptance probability p, therefore is

$$p = \begin{cases} 1 & \text{if} \Delta E \leq 0 \\ e^{-\Delta E/T} & \text{if} \Delta E > 0 \end{cases}.$$

- The Boltzmann probability is controlled by the temperature T. The SABC algorithm consists of several Markov chains that start at high values of T (10000 in our research to allow a global minimum). Reducing the temperature T slowly reduces the internal energy of the system until it reaches a minimum, which is the solution to our optimization problem. The values of T are determined by a cooling schedule

$$T^{k+1} = \frac{T^k}{1 + \left[T^k \ln(1+\delta)/(3\sigma^k)\right]}.$$

In the above equation T depends on δ and σ. δ controls the cooling speed and is set to 0.25 according to the guidelines in [53]. The cooling speeds are kept low to allow the algorithm to reach the global minimum. σ is the standard deviation of the energy during the final Markov chain.

- A stopping criterion to decide whether the algorithm has found a final solution. The algorithm terminates when there is no change in the accepted energy for a number of consecutive configuration changes.

In order to use either the SABC method or exhaustive search method to place branch cuts, every HARP image of the first frame of each slice needs to be unwrapped with manually placed branch cuts. This was accomplished by using a graphic user interface (GUI) in [120]. After the first frame of image was unwrapped, the following phase images were unwrapped with branch cut configurations minimizing the energy function discussed above. Figure 4.2 shows the time taken using the exhaustive search and simulated annealing methods to find a suitable solution for a given number of residues in the image. For each point on the horizontal axis, five images were identified with the corresponding number of residues. Each image was unwrapped using the SABC and exhaustive search methods. The average time taken was computed over three trials for each image and each method. The average of the time taken over the five images was then plotted as shown in Figure 4.2.

In this research, we utilized the fact that the exhaustive search is faster than the SABC when the number of residues is small but the SABC method is faster for greater number of residues. We found that the SABC method tended to be faster when the number of residues was larger than 5. Therefore a threshold of 5 was the computational optimized criteria to decide which method to be used. However, because the exhaustive search method always gives a global solution, we changed the threshold to 6 in our experiment to make the result more accurate, at the cost of a longer computation time. Figure 4.3 shows the distributions of number of residues in long-axis images and short-axis images. On average there were 3.8 residues presented in long-axis images and 2.9 residues in short-axis images. The proportions of images with more than 6 residues were relatively small (16% for long-axis images and 8% for short-axis images). Despite these facts, the SABC method is still necessary because if only the exhaustive search is applied the processing time will be prohibitively long.

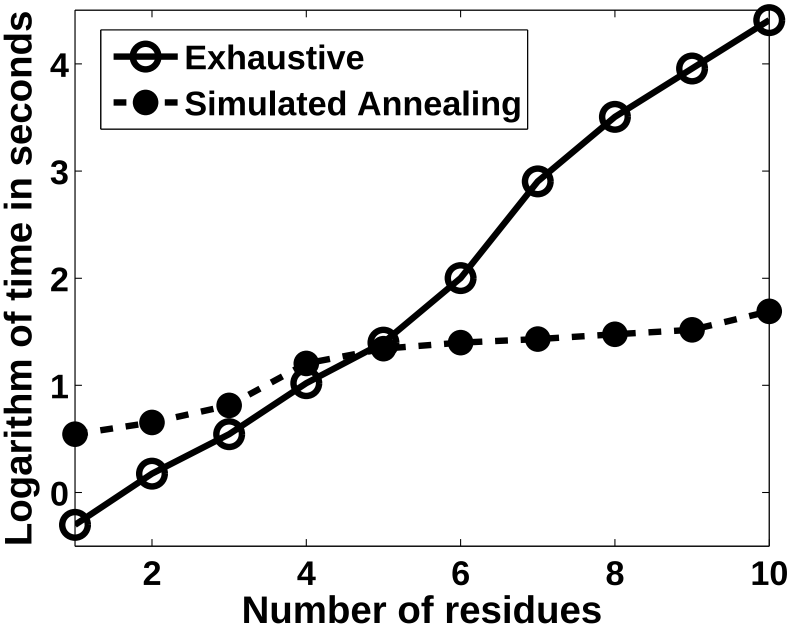

Figure 4.2: The logarithm (log_{10}) of the time taken in seconds using the exhaustive search and simulated annealing methods to find a suitable solution as functions of the number of residues.

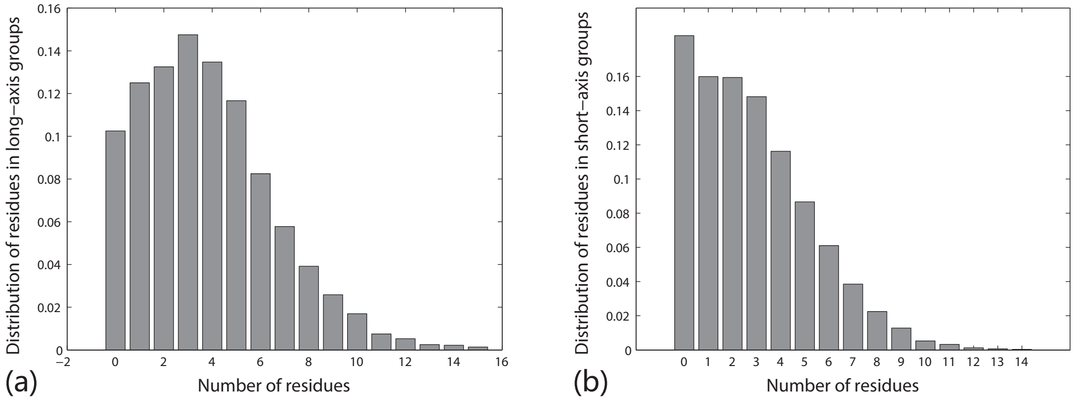

Figure 4.3: Distributions of residue number in each HARP image from long-axis (a) and short-axis (b) slices derived from histograms.

After the application of SABC or branch cutting using exhaustive search, some unwrapped phase images may still contain errors and therefore need to be fixed by introducing manual branch cutting. A discontinuity map, similar to that used in [114], was used to detect images with incorrect unwrapping. A discontinuity map measures the gradient of the unwrapped phase. If the unwrapping is correct, the spatial gradient magnitude of the unwrapped phase does not exceed π. When discontinuity was detected after unwrapping, user-interaction (as in [120]) was required to manually place branch cuts for that HARP image.

4.2.3 Motion and Strain Estimation

Since each HARP image is unwrapped independently, and the seed point for unwrapping varies from time to time, the unwrapped phases in two adjacent timeframes may differ by a multiple of 2π. As described in [120], this difference can be compensated by adding a multiple of 2π to the current unwrapped phase image. The multiple is chosen to minimize the L_1 norm of all differences between current and previous phase images. Note that this alignment assumes that the L_1 norm of the unwrapped phase difference between consecutive time frames is less than π, which corresponds to one-half of the tag spacing. Also, interframe deformation of more than one-half tag spacing in a localized region or regions will not affect the alignment as long as the average deformation is small.

Once HARP images in short-axis group and long-axis group were unwrapped, 1D displacement was measured at each pixel in the segmented myocardium using the technique described in [120]. 1D displacement measurements and a material-point mesh automatically constructed from the end-diastolic (ED) contours were used to compute 3D biventricular deformation and strain in each time frame throughout the cardiac cycle. The deformation and strain were reconstructed using a discrete model-free method as described in [40]. The entire procedure involved is called computer-assisted Strain from Unwrapped Phase (caSUP).

4.3 Experiments

4.3.1 Computation Time

All studies were processed using the caSUP technique described above, which was implemented in MATLAB (The Mathworks Inc, Natick, MA). Unwrapping all images in a study took less than a minute on a 2.6GHz Core2 Duo processor with 4 GB of memory. The average time required for fully-automated branch cut placement and phase unwrapping of both short and long-axis images was 7 seconds per HARP image or 60 minutes for a typical 320 image study. Compared to manually placed branch cut method (mSUP) [121], which is $1 \sim 2$ hours depending on user's proficiency, this is not a great improvement. However, we need to notice that this process is automatically done without supervision, and one can run several studies simultaneously. This is a great advantage over the previous method [121]. Another 5 minutes per study were required to manually correct branch cuts that caused 4% of images to have unwrapping inconsistencies. These images were automatically detected after automated branch cut placement and phase unwrapping as discussed in Section 4.2.2. The DMF strain reconstruction took about 30 minutes per study. The total time (not including the myocardial segmentation) required to analyze 20 time frames of a typical biventricular study with short and long-axis images was 90 minutes.

4.3.2 Parameter Sensitivity

As discussed in section 4.2, weighting factors λ_1 and λ_2 in the energy function (Equation 4.3) need to be decided. We conducted a parameter sensitivity test involving a test group of another 10 studies (4 normal volunteers, 3 hypertensive patients, and 3 patients with isolated mitral regurgitation) to optimize these two parameters. λ_1 and λ_2 were first empirically chosen as $\lambda_1 = 10^{-5}$ and $\lambda_2 = 10^{-3}$. Parameter combinations were acquired by changing either one of the two parameters logarithmically (with the scale of 1/10 and 10) while keeping the other parameter fixed. caSUP algorithm without branch cut corrections were

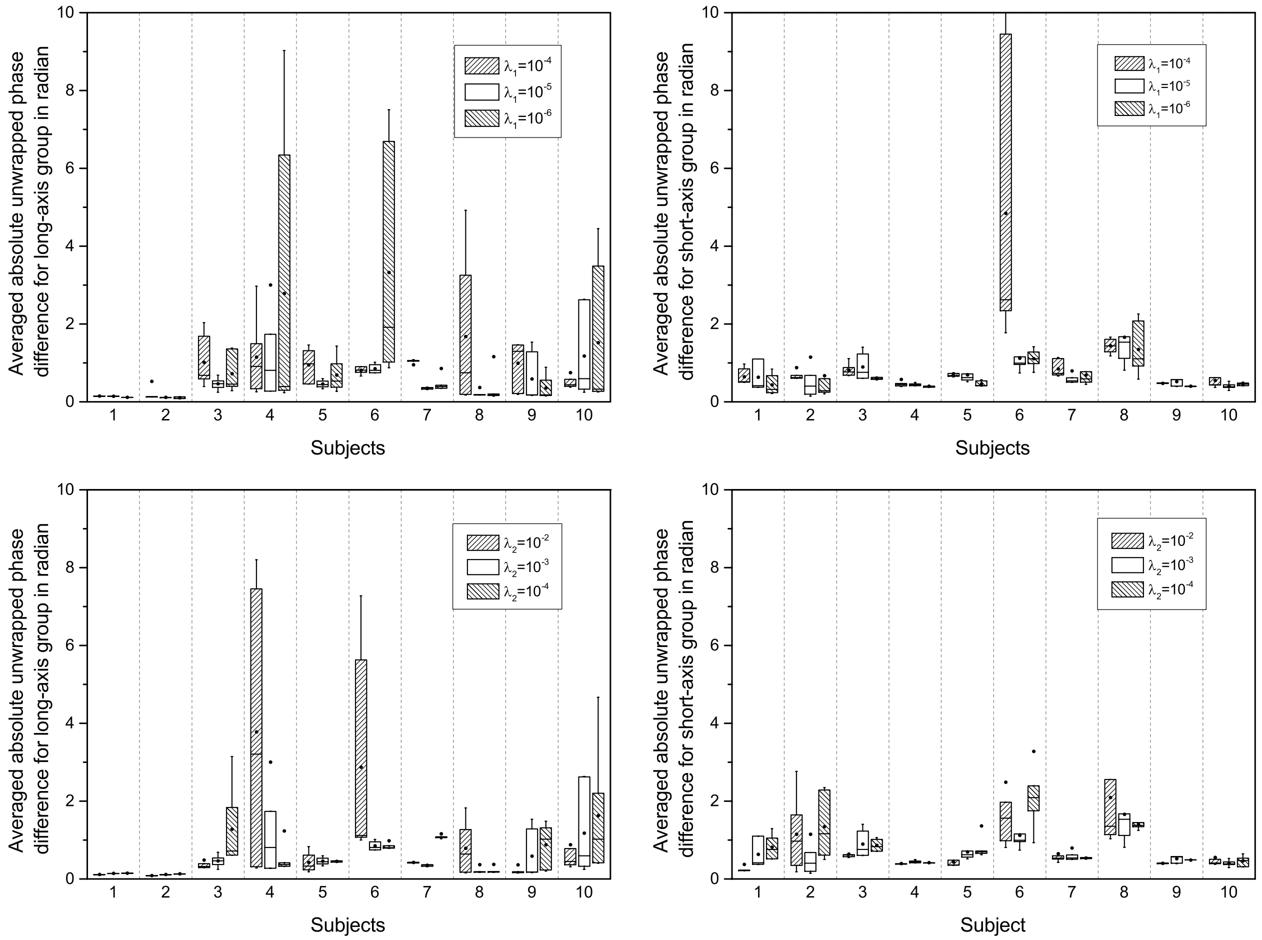

Figure 4.4: Parameter sensitivity test for λ_1 and λ_2 on a set of 10 human subjects. Six trials of averaged absolute unwrapped phase differences were computed by comparing to phase images with manually placed branch cuts. Plots on the left show the difference for long-axis groups and plots on the right show the difference for short-axis groups. λ_1 varies ($\lambda_1 \in \{10^{-4}, 10^{-5}, 10^{-6}\}$) while λ_2 is fixed to 10^{-3}, and λ_2 varies ($\lambda_2 \in \{10^{-2}, 10^{-3}, 10^{-4}\}$) while λ_1 is fixed to 10^{-5}.

then applied to five slices (two long-axis slices and three short-axis slices of basal, apical and mid-ventricle range) from each of the 10 subjects with six trials. Averaged absolute difference between the unwrapped phase and the unwrapping result with manually placed branch cuts was computed at each trial for each group (long and short). The parameter sensitivity test results are shown as Figure 4.4, which shows that a combination of default values of λ_1 and λ_2 ($\lambda_1 = 10^{-5}$ and $\lambda_2 = 10^{-3}$) gives an overall best result with least phase difference.

4.3.3 Validation

The caSUP method was validated on the cohort of 30 human subjects. In each subject, 3D biventricular strains in all timeframes were obtained with caSUP and mSUP methods. Both of these two methods utilize unwrapped phase images for displacement measurements and the discrete model-free method (DMF) in [40] to reconstruct the dense motion field. Strain from the feature-based method in [40] was also computed at time frames of end-diastole and end-systole. This feature-based method used user specified tag points for the displacement measurement, and the DMF method for 3D deformation interpolation. The accuracy of 3D strains with caSUP was assessed by comparing caSUP strains to mSUP strains and strains from feature-based (FB) method at end-systole (ES) with paired t-tests. In all statistical comparisons, a P-value of 0.05 or less was considered statistically significant. We also compared the 3D strains to 2D HARP strains qualitatively to validate its accuracy at different time frames along the cardiac cycle.

Tabel 4.1 shows statistics of the difference in averaged mid-ventricular strains and global twist (defined as rotation difference between base and apex) between caSUP and mSUP methods at ES. Correlations between strains and twists from caSUP and mSUP methods are high. Coefficients of variance (CV) for LV strain differences are lower than 3%. But CV for twist and RV strain differences are higher. All the strain parameters with caSUP method are statistically indifferent from those with mSUP method. Table 4.2 shows the comparison of end-systolic caSUP strains and twist with those from the FB method. LV strains and twists are highly correlated while RV strain correlations are lower. CV are lower than 3% in LV strains, lower than 5% in twist and lower than 6% in RV strains. LV strains, twist, and RV minimum principal strain with caSUP are not statistically different from those with FB method.

Table 4.3 shows comparison of peak strains (twists) and strain rates (twist rates) between the caSUP and mSUP methods. Peak $E_{\mathrm{tt}}RV$ early-diastolic rates, peak $E_{\min}RV$s, and peak $twist$ early diastolic rates are significantly different between these two methods. Correlations

Table 4.1: Comparison of end-systolic strains (unitless) and twist (degree) with caSUP and mSUP methods. Differences are caSUP-mSUP. Differences = Mean ± Standard Error. ρ= Correlation coefficient. For all correlation coefficients, $p < 0.001$. CV = coefficient of variation. E_{rr} = LV radial strain. E_{cc} = LV circumferential strain. E_{ll} = LV longitudinal strain. $E_{\min}$ = LV minimum principal strain. $E_{\mathrm{rr}}RV$ = RV radial strain. $E_{\mathrm{tt}}RV$ = RV tangential strain. $E_{\mathrm{ll}}RV$ = RV longitudinal strain. $E_{\min}RV$ = RV minimum principal strain.

Strain	Differences			p	ρ	CV
E_{rr}	0.0048	±	0.0018	0.51	0.94	2.14%
E_{cc}	0.0049	±	0.0020	0.52	0.94	2.17%
E_{ll}	0.0094	±	0.0024	0.31	0.94	2.32%
$E_{\min}$	0.0067	±	0.0023	0.43	0.93	1.67%
$Twist$	-0.3218	±	0.1797	0.61	0.92	3.79%
$E_{\mathrm{rr}}RV$	0.0113	±	0.0030	0.21	0.89	3.84%
$E_{\mathrm{tt}}RV$	0.0034	±	0.0044	0.73	0.80	5.77%
$E_{\mathrm{ll}}RV$	0.0145	±	0.0040	0.14	0.83	4.21%
$E_{\min}RV$	0.0065	±	0.0037	0.51	0.87	2.69%

Table 4.2: Comparison of end-systolic strains (unitless) and twist (degree) with caSUP and FB methods. Differences are caSUP-FB. Differences = Mean ± Standard Error. ρ= Correlation coefficient. For all correlation coefficients, $p < 0.001$. CV = coefficient of variation. E_{rr} = LV radial strain. E_{cc} = LV circumferential strain. E_{ll} = LV longitudinal strain. $E_{\min}$ = LV minimum principal strain. $E_{\mathrm{rr}}RV$ = RV radial strain. $E_{\mathrm{tt}}RV$ = RV tangential strain. $E_{\mathrm{ll}}RV$ = RV longitudinal strain. $E_{\min}RV$ = RV minimum principal strain.

Strain	Differences			p	ρ	CV
E_{rr}	0.0110	±	0.0022	0.14	0.91	2.48%
E_{cc}	0.0137	±	0.0019	0.07	0.94	2.03%
E_{ll}	0.0147	±	0.0030	0.11	0.90	2.81%
$E_{\min}$	0.0095	±	0.0025	0.25	0.91	1.81%
$Twist$	-1.3172	±	0.2077	0.06	0.93	4.07%
$E_{\mathrm{rr}}RV$	0.0201	±	0.0037	0.03	0.83	4.58%
$E_{\mathrm{tt}}RV$	0.0211	±	0.0044	0.03	0.79	5.30%
$E_{\mathrm{ll}}RV$	0.0290	±	0.0050	0.01	0.76	4.96%
$E_{\min}RV$	0.0183	±	0.0035	0.07	0.88	2.48%

of peak $E_{\mathrm{tt}}RV$ systolic rate and peak $twist$ are not significant. CV are higher for RV strains and twist.

Table 4.3: Comparison of peak strains (unitless), peak strain rates (1/sec), peak twists (degrees), and peak twist rates (degrees/sec) computed using the caSUP and mSUP methods. Difference = Mean pm Standard Error. ρ = Correlation Coefficient. CV = Coefficient of Variance. E_{cc} = LV Circumferential Strain. E_{min} = LV Minimum Principal Strain. $E_{\mathrm{tt}}RV$ = RV Tangential Strain. $E_{\mathrm{min}}RV$ = RV Minimum Principal Strain. Peak = Peak (maximum/minimum) strain/twist during the cardiac cycle. Sys Rate = Peak systolic strain/twist rate. E Dia Rate = Peak early diastolic strain/twist rate.

	Strain	caSUP - mSUP	p	ρ	p	CV
E_{cc}	Peak Strain	0.0043 ± 0.0003	0.57	0.95	< 0.001	1.92%
	Sys Rate	0.0138 ± 0.0022	0.73	0.91	< 0.001	2.34%
	E Dia Rate	0.0921 ± 0.0089	0.21	0.61	< 0.001	8.87%
E_{min}	Peak Strain	0.0035 ± 0.0004	0.68	0.94	< 0.001	1.42%
	Sys Rate	0.0019 ± 0.0025	0.97	0.94	< 0.001	2.22%
	E Dia Rate	-0.0258 ± 0.0060	0.64	0.64	< 0.001	7.07%
$Twist$	Peak Strain	1.5658 ± 0.0593	0.10	0.88	< 0.001	3.65%
	Sys Rate	8.0144 ± 0.3197	0.11	0.91	< 0.001	4.13%
	E Dia Rate	-21.8176 ± 1.1832	0.00	0.06	0.739	14.19%
$E_{\mathrm{tt}}RV$	Peak Strain	0.0074 ± 0.0005	0.38	0.87	< 0.001	3.42%
	Sys Rate	-0.0033 ± 0.0093	0.95	0.19	0.312	9.69%
	E Dia Rate	0.2039 ± 0.0102	0.01	0.50	0.005	8.65%
$E_{\mathrm{min}}RV$	Peak Strain	0.0016 ± 0.0005	0.86	0.90	< 0.001	2.11%
	Sys Rate	0.0239 ± 0.0102	0.74	0.39	0.035	8.92%
	E Dia Rate	-0.0489 ± 0.0075	0.44	0.56	0.001	8.53%

Figure 4.5 shows maps of 3D LV circumferential strain (E_{cc}) and RV tangential strain ($E_{\mathrm{tt}}RV$) computed from the caSUP and the mSUP methods for a representative from each subject group. Note that the same motion estimation and strain reconstruction method was used (DMF). The strain maps are mostly similar. Differences, if any, are noted at basal right ventricular free wall where the increased through-plane motion violated the assumption in section 4.2 that area between two neighboring tag lines stays the same from one cardiac frame to the next.

Figure 4.6 is the plot of averaged mid-ventricular strains (unitless) and twists (degree) from caSUP and HARP methods for different pathologies throughout the cardiac cycle. caSUP strains and twist show agreement with the 2D HARP strains and twist except for

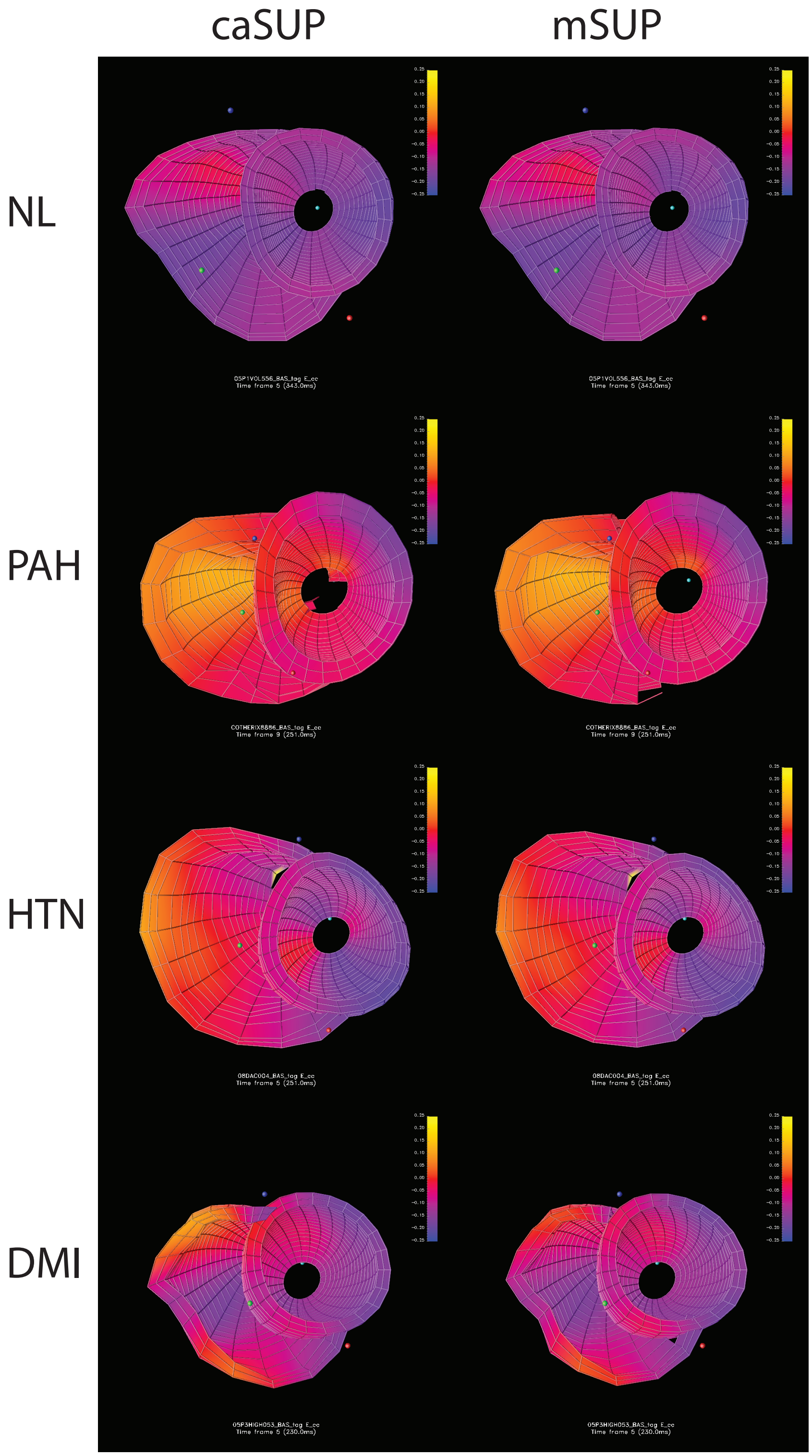

Figure 4.5: Maps of LV circumferential (E_{cc}) strain and RV tangential ($E_{\text{tt}}RV$) strain using caSUP (left column) and mSUP (right column) methods for a representative from each of the four subject groups: NL, PAH, HTN, and DMI at end-systole (ES). Strains are mapped from blue = -25% to yellow = 25%.

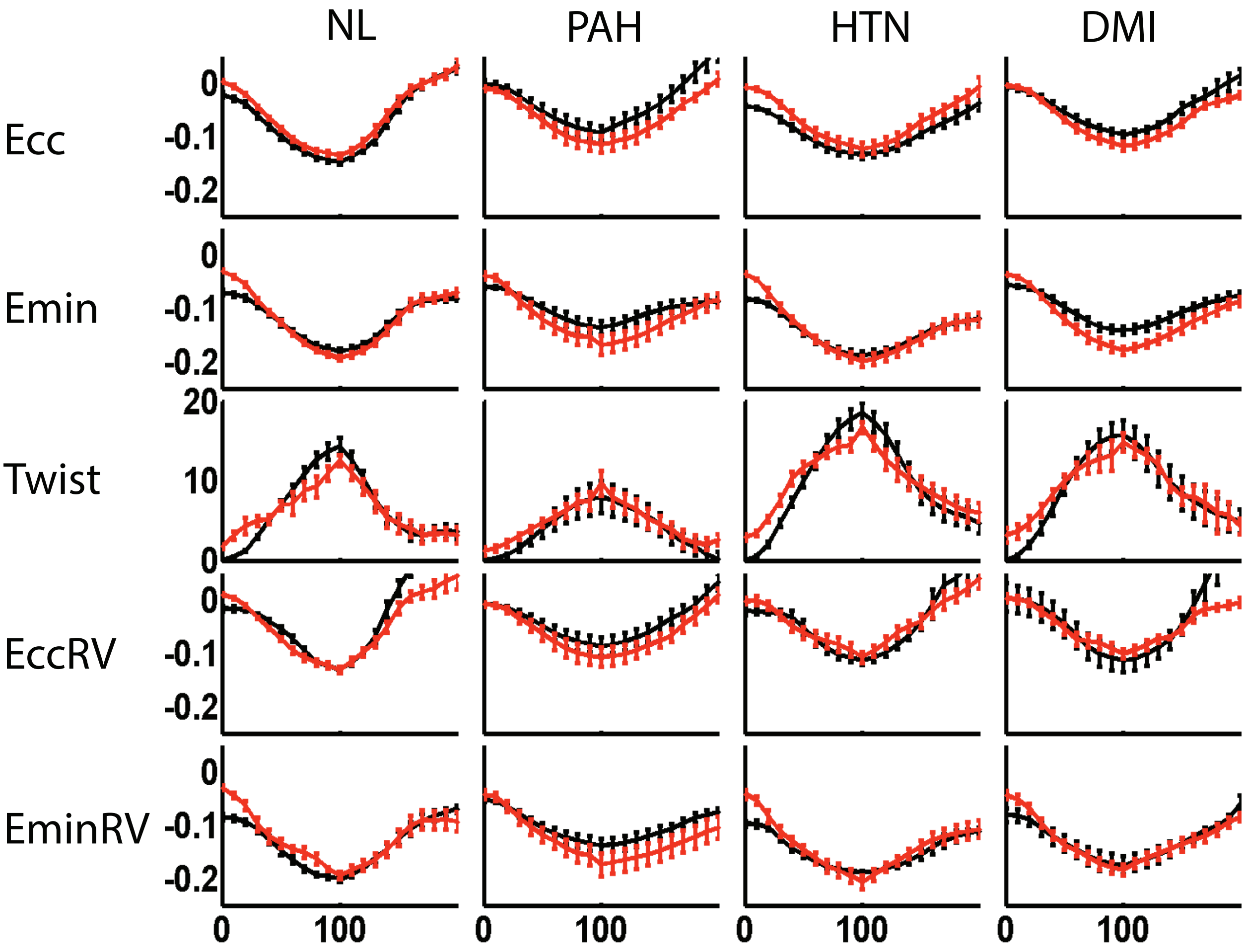

Figure 4.6: Averaged mid-ventricular strains (unitless) and twists (degree) for NL, PAH, HTN, and DMI hearts using caSUP (red) and HARP (black) methods. Error bars represent standard errors.

some differences around end-systole, which is not surprising because HAPR method provides 2D Eulerian strains while caSUP is a 3D Lagrangian strain reconstruction method.

4.4 Discussion and Conclusion

A computer-assisted strain from unwrapped phase (caSUP) procedure was presented for estimating 3D dense motion field and strain from tagged MRI. This method used automated branch cut placement to resolve residues presented on HARP images, followed by phase unwrapping of these HARP images. Manual intervention, with a small chance, was necessary to modify the branch cut configuration when unwrapping errors were discovered. Displacement and 3D biventricular strain then can be calculated from the unwrapped phase images. 30 clinical studies from normal volunteers and patients with three different pathologies were used to validate the algorithm. caSUP strains demonstrated excellent agreement with the previously presented manual strain from unwrapped phase (mSUP).

The time required for the caSUP to unwrap all HARP images including both LV and RV over 20 time frames is approximately 60 minutes per study or 7 seconds per HARP image without user supervision. Another 5 minutes of user interaction is required to correct any erroneous unwrapped phase. The same analysis would take around $1 \sim 2$ hours with intensive user interaction using the mSUP method. The feature-based method [39, 40] would require about 3 hours of user interaction. Most of the user interaction is involved later in the cycle (mid to late diastole) when tag lines fade and the CNR reduces significantly. Advanced tagged imaging techniques such as CSPAMM, can yield a higher tag CNR throughout the cardiac cycle. Images with higher CNR will have fewer phase inconsistencies, and therefore, automated branch cut placement is faster and more accurate and less user interaction will be required to correct them. Consequently, if strains are to be computed only through systole or till early diastole as is so often the case, time consumption and user interaction can drastically reduce.

Unlike HARP tracking [85], which requires small deformation between consecutive timeframes, the caSUP method only assumes averaged deformation of tissue between timeframes to be less than half tag spacing. This advantage makes the caSUP method be applicable to larger deformed tissues like right ventricle free wall where traditional methods would fail. One the other hand, the displacement measurements acquired from unwrapped phase with computer-assisted branch cuts could be applied to either model-based strain reconstruction or non-model-based strain reconstruction. Therefore this technique can potentially be applicable to non-myocardial tissues because it does not have to assume a regular shape as HARP does.

The caSUP technique reconstructs a 3D+time biventricular strain maps from tagged MR images, and takes into account the through-plane motion of the heart. Slice following DENSE [115], zHARP [3] and HARP-SENC [108] can count in the through-plane motion, but these techniques require two breath-holds per slice. In contrast, tagged images can be acquired with multiple slices per breath hold which allows the entire biventricle to be imaged in significantly less time.

In conclusion, the computer-assisted strain from unwrapped phase (caSUP) method can compute parameters such as 3D strains and strain rates in both LV and RV and twist in the LV through the cardiac cycle with a reasonable amount of computation time and minimal user interaction compared to other manual 3D analysis methods.

Chapter 5

HARMONIC PHASE UNWRAPPING USING INTEGER OPTIMIZATION AND DYNAMIC MODEL FOR BIVENTRICULAR CARDIAC STRAIN ANALYSIS

5.1 Introduction

As described in Chapter 2, displacement measurements from tagged MRI can be acquired by either detecting and tracking feature points, such as tag line points and tag intersections, or converting the original image to a phase image, computed from the inverse Fourier transform of the isolated spectrum peak in k-space of the original tagged image.

For the second method, the resulted phase map is called HARmonic Phase (HARP) image, and was used for cardiac strain computation in the HARP-based methods including HARP strain [86] and HARP tracking [85]. HARP is robust against noise, due to its bandpass filtering nature. Another advantage of HARP method is that the processing is fully automated, except for the myocardium segmentation and landmarks placement. These benefits enabled HARP to be one of the most popular cardiac strain evaluation techniques [113]. However, there are still some limitations of the HARP methods. For HARP strain method, the computed result is 2D Eulerian strain, instead of Lagrangian strain. For HARP tracking, although the resulted strain is Lagrangian, tracking errors may happen near the boundaries of the myocardium, i.e., epicardium and endocardium, due to the disappearing and reappearing of the myocardium signal caused by through-plane motion [118]. On the other hand, tracking errors will accumulate and propagate along with the time, making the tracking accuracy less and less accurate for later time frames.

To compensate for these shortcomings, a harmonic phase unwrapping method was developed in [120, 121]. This method unwrap HARP images using quality-guided phase unwrapping. The resulted unwrapped phase is linearly related to the 1D displacement along the tag modulation orientation at each pixel location. Therefore, by unwrapping the HARP image, the 1D displacement measurements can be readily available. A primary challenge of the quality-guided phase unwrapping is the number of phase inconsistencies present on the phase map. Because the quality-guided phase unwrapping is path dependent and sensitive to these inconsistencies (also called residues), certain regions need to be cut off to guide the phase unwrapping process. This was done by cutting off pixels long manually placed branch cuts that connect between residues with different polarities or from residue to the myocardium boundary. One significant result of this treatment is the prolonged processing time. Depending on the proficiency of the operator, the branch cut placement for a typical cardiac study composed of 320 tagged images will take $1 \sim 2$ hours.

An alternative to the quality-guided phase unwrapping is to treat the unwrapping problem as an integer optimization one. Since at each pixel the difference between the unwrapped phase and wrapped phase is an integer multiple of 2π, we can optimize the integer field such that the unwrapped phase map is optimal in the sense of spatial smoothness [20, 130]. Notice that because HARP image is biased with a linear phase determined from the tag modulation, we need to first remove this offset and the result is the demodulated HARP image. By treating the unwrapped phase at each pixel as a random variable, we show that the optimization problem can be framed using a Markov random field and unwrapped phase difference between neighboring pixels defines the energy function. To further improve the algorithm, we process the phase images sequentially such that the unwrapped phase map at previous time can provide prior information for the unwrapping at current time frame. A temporal smoothness term, which penalizes the unwrapped phase difference between neighboring time frames at the same pixel, is then incorporated into the energy function as unary terms. The energy function is a mixture of pairwise terms and unary terms, which can be minimized over the integer field globally using a max-flow/min-cut algorithm [64]. This technique has been applied to left ventricular (LV) strain analysis in our previous research work [70].

However, this unwrapping technique does not take in the dynamics the myocardium. As we observe the cardiac motion, the myocardium contraction and dilation is periodic and can roughly be considered oscillatory. This provides us the intuition that we can use a dynamic model [95, 96] to estimate and predict the unwrapped phase at each time frame, thus enabling a more accurate unwrapping process. In this research, we model the unwrapped demodulated HARP of the myocardium using B-spline surface with grid control points. Mean locations, current locations, and velocities of all control points define the state variables. Kalman filtering with an oscillatory dynamic model is used to estimate the state at current time and to predict the state and observations at the next [18]. The predicted observations, including predicted unwrapped phase values, will be used for providing credentials for unwrapping the new demodulated HARP image. This modification using dynamic model is useful especially for unwrapping right ventricle (RV) region, which is known to have a larger interframe deformation.

The rest contents are organized as follows: Section 5.2 introduces the proposed method including phase unwrapping and strain reconstruction. Section 5.3 introduces the experiments and shows the results. Section 5.4 is the discussion and conclusion.

5.2 Methods

5.2.1 Demodulated HARP

HARmonic Phase (HARP) image [85, 86] is computed from tagged MRI with the following procedure. First, tagged image is converted to k-space using Fourier transform. Then a bandpass filter determined by tag modulation frequency and angle is used to isolate the corresponding spectrum peak. By applying the inverse Fourier transform the isolated peak yields a complex image. The resulting angle map is called harmonic phase image. The phase value at each pixel is linearly related to 1D displacement component projected along the modulation orientation, except that it is wrapped within $[-\pi, \pi)$. Relationships between HARP ψ (wrapped) and the absolute phase ϕ (unwrapped), and the absolute phase ϕ and

1D displacement d are: $\psi = W(\phi) = \text{mod}(\phi + \pi, 2\pi) - \pi$, $\phi = w(x - d) = u - xd$, where $W(\cdot)$ denotes the wrapping function in [85, 86], $\text{mod}(\cdot)$ denotes the modulo, w is the tag modulation frequency and x is the spatial coordinate of the pixel.

We can see that absolute phase map is biased with a linear phase determined by the tag modulation frequency and orientation. Because of this bias, the unwrapped HARP image is intrinsically nonsmooth in the first-order sense. To eliminate this bias effect, as we show later that spatial smoothness is a criterion for unwrapping process, we compute demodulated HARP images from original HARP images by $\mathbf{\Psi}_{\text{demod}} = W(\mathbf{\Psi}_{\text{HARP}} - U)$, where $\mathbf{\Psi}_{\text{demod}}$ is the demodulated HARP image, $\mathbf{\Psi}_{\text{HARP}}$ is the HARP image, and U is the linear phase map. Once we unwrap $\mathbf{\Psi}_{\text{demod}}$ to get the unwrapped demodulated HARP image $\mathbf{\Phi}_{\text{demod}}$, 1D displacement measurement at each pixel can be computed. For the rest contents, unless otherwise noted, we denote $\mathbf{\Psi}_{\text{demod}}$ by $\mathbf{\Psi}$ and $\mathbf{\Phi}_{\text{demod}}$ by $\mathbf{\Phi}$.

5.2.2 Phase Modeling and Phase Unwrapping

We observe the relationship between the unwrapped phase (absolute phase) ϕ and the wrapped phase (principal phase) ψ at each pixel: $\phi = \psi + 2k$. k is an integer called *wrap count*. In other words, the phase unwrapping is to reconstruct the wrap count map from the wrapped phase image. We model the unwrapped phase image by treating the unwrapped phase values as random variables, similar to the one introduced in [130]. We then derive an energy function as a mixture of pairwise and unary terms from this phase modeling.

Let us define the absolute phase image as $\mathbf{\Phi} = \{\phi_m, m \in \mathcal{S}\}$ and the wrapped phase image as $\mathbf{\Psi} = \{\psi_m, m \in \mathcal{S}\}$, where m is the index of pixel and $\mathcal{S}$ is the index set of all pixels. According to [130], the ill-posed problem can be solved by using maximum *a posteriori* (MAP) estimator as follows

$$\hat{\mathbf{\Phi}} = \underset{\mathbf{\Phi}}{\text{argmax}}\, p(\mathbf{\Phi}|\mathbf{\Psi}) = \underset{\mathbf{\Phi}}{\text{argmax}}\, p(\mathbf{\Psi}|\mathbf{\Phi})p(\mathbf{\Phi}). \tag{5.1}$$

$p(\mathbf{\Phi}|\mathbf{\Psi})$ and $p(\mathbf{\Phi})$ are posterior and prior distributions and $p(\mathbf{\Psi}|\mathbf{\Phi})$ is the likelihood function. According to the relationship between absolute phase and wrapped phase, the likelihood function has the following form

$$p(\mathbf{\Psi}|\mathbf{\Phi}) = \prod_m \delta\big((\psi_m - \mathcal{W}(\phi_m)\big), \tag{5.2}$$

where $\delta(\cdot)$ is the Dirac delta function. However, using this likelihood function alone cannot determine the absolute phase as there are infinite optimal solutions. We then introduce a Markov random field (MRF) framework to regulate the estimation problem. Based on the assumption of the MRF, each random variable communicates with a restricted set of other random variables, that forms the neighborhood of this variable. In [130], the neighborhood system was set to be 4-connected system on the pixel grids, meaning that the neighborhood for a pixel not located on the border are four pixels that are directly connected to it, i.e., up, down, left, and right pixels. A pair of this pixel and one of its neighborhood forms a clique, denoted as c, and the set of all cliques is $\mathcal{C}$. We then assume the prior distribution $p(\mathbf{\Phi})$ of this first-order MRF to be Gibbsian, which is like

$$p(\mathbf{\Phi}) = Z(\beta)^{-1}\mathrm{exp}\big(-\beta \textstyle\sum_{c\in\mathcal{C}} V_c(\phi_c)\big), \tag{5.3}$$

where $Z(\beta)$ is the partition function that normalizes the distribution and will not influence the shape of the distribution. β is the inverse temperature. $V_c(\cdot)$ is the clique potential function and ϕ_c denotes a vector composed of the phase values within the clique c. The form of the prior distribution is like

$$p(\mathbf{\Phi}) \propto \exp\big(-\beta \sum_{m\sim n} V(\phi_m - \phi_n)\big), \tag{5.4}$$

where $m \sim n$ means that the pair of pixels m and n forms a clique in the 4-connected system, and $V(\cdot) = (\cdot)^2$ is the clique potential function that gives a Gauss-Markov prior. Using this prior distribution, the MAP estimation problem is then equivalent to minimizing the following energy function over the wrap count map $\mathbf{k} = \{k_m, m \in \mathcal{S}\}$ given the wrapped phase image $\mathbf{\Psi}$

$$\hat{\mathbf{k}} = \underset{\mathbf{k}}{\operatorname{argmin}}\, E(\mathbf{k}|\mathbf{\Psi}) = \underset{\mathbf{k}}{\operatorname{argmin}} \sum_{m \sim n} \big[\psi_m - \psi_n + 2\pi(k_m - k_n)\big]^2. \tag{5.5}$$

However, by minimizing this energy function, the unwrapped demodulated HARP image may not be accurate even though a first-order spatial smoothness is maximized. This is because we are dealing with phase images contaminated mostly by artifacts, which are difficult to model. An improvement to this unwrapping method for the implementation to a sequence of demodulated HARP images is to take the advantage of the previously unwrapped images within the sequence, as we assume this information will provide some information for the unwrapping of the current time frame. Following this, we have a modified MAP estimation of the unwrapped phase

$$\begin{aligned}
\hat{\mathbf{\Phi}} &= \underset{\mathbf{\Phi}}{\operatorname{argmax}}\, p(\mathbf{\Phi}|\mathbf{\Psi}, \tilde{\mathbf{\Phi}}) \\
&= \underset{\mathbf{\Phi}}{\operatorname{argmax}}\, p(\mathbf{\Psi}|\mathbf{\Phi}, \tilde{\mathbf{\Phi}}) p(\tilde{\mathbf{\Phi}}|\mathbf{\Phi}) p(\mathbf{\Phi}) \\
&= \underset{\mathbf{\Phi}}{\operatorname{argmax}}\, p(\mathbf{\Psi}|\mathbf{\Phi}) p(\tilde{\mathbf{\Phi}}|\mathbf{\Phi}) p(\mathbf{\Phi}).
\end{aligned} \tag{5.6}$$

In the above equation, $\tilde{\mathbf{\Phi}}$ is a rough estimation of the absolute phase map. $p(\mathbf{\Psi}|\mathbf{\Phi}, \tilde{\mathbf{\Phi}}) = p(\mathbf{\Psi}|\mathbf{\Phi})$ because the wrapped phase $\mathbf{\Psi}$ is only determined by $\mathbf{\Phi}$. The change of this equation compared to Equation 5.1 is the term $p(\tilde{\mathbf{\Phi}}|\mathbf{\Phi})$, which is the conditional probability of the estimation $\tilde{\mathbf{\Phi}}$ on $\mathbf{\Phi}$. Let us assume the estimation error to be white Gaussian, with mean ϕ_m and standard deviation σ_m at each pixel m, then we have

$$p(\tilde{\mathbf{\Phi}}|\mathbf{\Phi}) \propto \exp\big(-\sum_m \frac{1}{2\sigma_m^2}(\tilde{\phi}_m - \phi_m)^2\big). \tag{5.7}$$

Equation 5.5 after modification becomes

$$\begin{aligned}\hat{\mathbf{k}} &= \operatorname*{argmin}_{\mathbf{k}} E(\mathbf{k}|\boldsymbol{\Psi}, \tilde{\boldsymbol{\Phi}}) \\ &= \operatorname*{argmin}_{\mathbf{k}} \sum_{m\sim n} \big[\psi_m - \psi_n + 2\pi(k_m - k_n)\big]^2 + \sum_m \lambda_m \big[\psi_m + 2\pi k_m - \tilde{\phi}_m\big]^2, \qquad (5.8)\end{aligned}$$

where $\lambda = (2\beta\sigma_m^2)^{-1}$ is the weighting factor that balances the unary term at each pixel m. In previous research [70], we processed the demodulated HARP images sequentially and let $\tilde{\boldsymbol{\Phi}}_t = \boldsymbol{\Phi}_{t-1}$, where t is the current time frame and $\boldsymbol{\Phi}_{t-1}$ is the computed unwrapped image at previous time. This selection took the advantage of temporal smoothness of the absolute demodulated HARP images as we assumed that the interframe deformation was small and the unwrapped phase at previous time could provide some information to the unwrapping at current time. However, this is a strong assumption and will impose a problem especially for the unwrapping at right ventricle (RV), where a larger interframe deformation is expected during the systolic phase. In this research, we improve the estimation of the absolute demodulated HARP image by using a dynamic model as well as Kalman filtering, which update state variables and predict absolute phase values at next time frame.

5.2.3 Dynamic Model and Kalman Filtering

The basic idea to use dynamic model for assisting unwrapping process is that the cardiac motion is periodic. By describing the unwrapped demodulated phase values parametrically, we can define state variables with these parameters and update and predict the state at the upcoming time frame. The predicted observations serve as the estimated unwrapped map $\tilde{\boldsymbol{\Phi}}$. Also we can acquire an estimation of σ_m at each pixel location. This treatment instead of using unwrapped phase image directly from previous time and a constant standard deviation like in [70] can incorporate the cardiac dynamics and will potentially improve prediction when a larger interframe deformation is expected, like in RV region.

We can parameterize an unwrapped phase map using a B-spline surface of degree l

$$C(x,y) = \sum_{i=1}^{p+1}\sum_{j=1}^{q+1} B_{i,j}N_{i,l}(x)M_{j,l}(y). \tag{5.9}$$

$C(x,y)$ is the value of the surface at coordinate (x,y), B is the mesh of $(p+1)\times(q+1)$ control points, N and M are piecewise polynomial functions along x and y directions, respectively. At each pixel location (x,y) we can rewrite the above equation with matrix multiplication as $c = \boldsymbol{e}'\boldsymbol{b}$, where $\boldsymbol{e}$ is vectorized outer product of N and M, $\boldsymbol{b}$ is vectorized control point mesh B, and prime notation denotes transpose. For the B-spline fitting problem, we try to solve $\boldsymbol{b}$ by minimizing sum of squares of the following error

$$\boldsymbol{z} - E_{\text{full}}\boldsymbol{b}, \qquad E_{\text{full}} = \begin{bmatrix} E \\ \sqrt{\lambda}D \end{bmatrix}. \tag{5.10}$$

$\boldsymbol{z}$ is the vector of observed values (unwrapped phase values) with zeros appended, E is the matrix of stacked $\boldsymbol{e}$ at all observed pixel locations, D is the matrix of second-order derivative operator, and λ is a parameter to control smoothness of the fitting surface. We need to make the fitted B-spline surface spatially smooth such that the control point values near the myocardium boundary will be stable.

We consider each control point undergoes oscillatory motion with a constant angular velocity ω. Then for each control point b, we have its value (or location) at arbitrary time t equals to $b(t) = \bar{b}(1 - \cos(\omega t)$, where $\bar{b}$ is the mean location throughout the cycle. Notice that the mean location $\bar{b}$ is necessary to describe the cyclic dynamics. The continuous-time state-space model [96] for state variable $\xi(t) = [\bar{b} \quad b \quad \dot{b}]'$ will be

$$\dot{\xi}(t) = \begin{bmatrix} 0 & 0 & 0 \\ 0 & 0 & 1 \\ \omega^2 & \omega^2 & 0 \end{bmatrix} \xi(t) + \begin{bmatrix} 1 & 0 \\ 0 & 0 \\ 0 & 1 \end{bmatrix} v(t), \tag{5.11}$$

where $v(t)$ is the continuous-time white noise that accounts for the uncertainty of the estimation of control point mean location and velocity. Covariance of this white noise is

$$\Gamma(t) = \mathbb{E}[v(t)v(t)'] = \begin{bmatrix} q_1^2 & 0 \\ 0 & q_2^2 \end{bmatrix}. \tag{5.12}$$

The discrete-time state-space model [96] for the single state variable is

$$\xi(k+1) = \begin{bmatrix} 1 & 0 & 0 \\ 1-\cos(\omega T) & \cos(\omega T) & \frac{1}{\omega}\sin(\omega T) \\ \omega\sin(\omega T) & -\omega\sin(\omega T) & \cos(\omega T) \end{bmatrix} \xi(k) + v(k) = F_{cy}\xi(k) + v(k). \tag{5.13}$$

Covariance of the discrete-time noise process is $Q_{cy} = [q_{i,j}]_{3\times3}$, with each element $q_{i,j}$ computed from $\Gamma(t)$ [96].

Now consider a state variable for all control points $\boldsymbol{s} = [\xi_1' \quad \xi_2' \quad \xi_3' ...]'$ where ξ_i represents the single state variable for ith control point. The state covariance matrix is P. The discrete-time state-space model for $\boldsymbol{s}$ is provided as

$$\boldsymbol{s}(k+1) = F\boldsymbol{s}(k) + \boldsymbol{v}(k), \tag{5.14}$$

where $F = I_{(p+1)\times(q+1)} \otimes F_{cy}$, $I_{(p+1)\times(q+1)}$ is the identity matrix with rank $(p+1)\times(q+1)$ and operator $\otimes$ denotes Kronecker product. $\boldsymbol{v}$ is the discrete-time white noise vector for state variable with covariance $Q(k) = \text{cov}(\boldsymbol{v}(k)) = I_{(p+1)\times(q+1)} \otimes Q_{cy}$.

The discrete-time measurement equation is

$$\begin{aligned} \boldsymbol{z}(k) &= H(k)\boldsymbol{s}(k) + \boldsymbol{w}(k) \\ H(k) &= E_{\text{full}} \otimes \begin{bmatrix} 0 & 1 & 0 \end{bmatrix}, \end{aligned} \tag{5.15}$$

where $\boldsymbol{w}$ is the measurement noise having zero mean and covariance matrix $R = diag(r^2)$. $diag(\cdot)$ denotes diagonal matrix.

Kalman filter update [18] for the state estimation and measurement prediction is

$$\begin{aligned} \boldsymbol{s}(k+1|k) &= F\boldsymbol{s}(k|k) \\ \hat{\boldsymbol{z}}(k+1|k) &= H(k+1)\boldsymbol{s}(k+1|k). \end{aligned} \tag{5.16}$$

State covariance prediction and update are

$$\begin{aligned} P(k+1|k) &= FP(k|k)F' + Q(k) \\ S(k+1) &= H(k+1)P(k+1|k)H(k+1)' + R(k+1) \\ W(k+1) &= P(k+1|k)H(k+1)'S(k+1)^{-1} \\ P(k+1|k+1) &= P(k+1|k) - W(k+1)S(k+1)W(k+1)^{-1}, \end{aligned} \tag{5.17}$$

where S is covariance matrix of the measurement prediction error, also called the innovation covariance matrix. W is the filter gain matrix. Due to the large size of matrix S, we need to avoid computing its inverse in order to improve efficiency. This is done by using equivalent forms of the last two equations

$$\begin{aligned} P(k+1|k+1)^{-1} &= P(k+1|k)^{-1} + H(k+1)'R(k+1)^{-1}H(k+1) \\ W(k+1) &= P(k+1|k+1)H(k+1)'R(k+1)^{-1}. \end{aligned} \tag{5.18}$$

Measurement residual and state update are

$$\begin{aligned} \boldsymbol{\nu}(k+1) &= \boldsymbol{z}(k+1) - \hat{\boldsymbol{z}}(k+1|k) \\ \boldsymbol{s}(k+1|k+1) &= \boldsymbol{s}(k+1|k) + W(k+1)\boldsymbol{\nu}(k+1). \end{aligned} \tag{5.19}$$

To start the state estimation and measurement prediction for the unwrapped demodulated HARP sequence, we need to initialize the Kalman filter with initial state variable $\boldsymbol{s}(1|1)$ and covariance matrix $P(1|1)$. We used a two-point differencing method [18, 96] to obtain an estimation of the control point locations and velocities and corresponding covariance matrix. We first fit a B-spline surface to the unwrapped phase and acquire control point locations $\boldsymbol{b}(1)$ at $t = 1$.

$$\dot{\boldsymbol{b}} = \frac{\boldsymbol{b}(1) - \boldsymbol{b}(0)}{T} = \boldsymbol{b}(1)/T$$
$$P(1|1) = I_{(p+1)\times(q+1)} \otimes \begin{bmatrix} \bar{R} & 0 & 0 \\ 0 & R & R/T \\ 0 & R/T & R/T^2 \end{bmatrix}. \tag{5.20}$$

$\boldsymbol{b}(0) = \mathbf{0}$ because displacement is zero all over the myocardium at the beginning of the image sequence when tag profile has just been applied. $\bar{R}$ and R are the variances of mean position and position of each control point at initialization. For above set up, we determined initial values for control point locations and velocities. However, mean positions for these control points over cardiac cycle need to be determined too. To do so, we use a graphic user interface and manually placed branch cuts [120] to unwrap demodulated HARP images for all slices at time frame closest to end-systole (ES) when control points reach their peak locations. Then we fit a B-spline surface to each unwrapped image to yield a set of control point values. Half of these values serve as a guess of the initial values for the mean control point locations.

We unwrap the demodulated HARP image at the first time frame $t = 1$ to acquire $\boldsymbol{z}(1)$. A constant standard deviation σ_m and zero map $\tilde{\boldsymbol{\Phi}}_1 = \boldsymbol{\Phi}_0 = \mathbf{0}$ are used to unwrap. For later time $t > 1$, we acquire a prediction of unwrapped phase values $\hat{\boldsymbol{z}}$ within myocardium using above Kalman filtering technique. This prediction fills up the myocardium region of $\tilde{\boldsymbol{\Phi}}_t$ with prior n values (n is the number of pixels within myocardium region) and rest values will be discarded.

In order to unwrap the demodulated HARP image using discussed method in Section 5.2.2, we also need to estimate the standard deviation σ_m at each pixel location within the myocardium. This is done by extracting diagonal elements in the innovation covariance matrix S. We let σ_m^2 be equal to values of these elements at specific locations. This is because S estimate the measurement prediction error, which is the difference between predicted unwrapped phase values and computed unwrapped phase values.

Starting from the second time frame, we fill up $\boldsymbol{z}$ by using the computed unwrapped phase image and update the state variable to provide prediction at next time. The phase unwrapping is done sequentially till the very last time frame.

5.2.4 Integer Optimization for Unwrapping

The minimization of Equation 5.8 can be accomplished using several integer optimization methods. In [130] a dynamic programming algorithm was used. In [20] a graph cuts method was used. The integer optimization was broken into several iterations and a binary map was optimized at each iteration by applying a max-flow/min-cut algorithm to the corresponding graph. The wrap count map was updated with this binary map at each iteration. This method has the advantage of lower computational complexity, as long as the clique potential function is convex and a submodularity condition is met (which we will discuss later in this section). In this research, we adopt this graph cuts-based optimization method with some modifications. First, in [20], the clique potential function is nonconvex in order to preserve the phase discontinuity. However, this imposed nonsubmodular terms to the integer optimization, which is typically an NP-hard problem and cannot be solved using standard graph cuts algorithms. [20] avoided this situation by truncating nonsubmodular terms, resulting in an estimated solution to the optimization problem. In our research, because the myocardial displacement field and the unwrapped demodulated HARP image are continuous and smooth, we restricted the phase unwrapping to be within the segmented myocardium. This restriction allows us to use a quadratic clique potential function as there are no discontinuities to be preserved. Second, as we have discussed previously, a unary term was added to the energy function to evaluate the difference between the candidate unwrapped phase and estimated phase image. Because of this addition, a modified version of the iteration scheme in [20] is also proposed.

Let $\mathbf{k}_t^0 = \mathbf{0}$ be initialized wrap count map for the demodulated HARP image at time t with iteration step 0, and the wrap count map at each step $i+1$ is updated by $\mathbf{k}_{\text{myo},t}^{i+1} = \mathbf{k}_{\text{myo},t}^{i} + \alpha\boldsymbol{\Delta}_t^{i+1}$. $\alpha \in \{1, -1\}$ is a sign indicator and $\boldsymbol{\Delta}_t^{i+1} = \{\delta_{m,t}^{i+1}, m \in \mathcal{S}_{\text{myo},t}\}$ is the binary map with each pixel taking a binary value $\delta_{m,t}^{i+1} \in \{0, 1\}$. Subscript "myo" in $\mathbf{k}'^{i+1}_{\text{myo},t}$ and $\mathcal{S}_{\text{myo},t}$ denotes myocardium region for the wrap count image and the index set. Note that we only update the wrap count at pixels within the myocardium at time t, and the wrap count value for pixels outside remains to be 0. Then the energy function at each iteration step $i+1$ is minimized to optimize the corresponding binary map

$$\begin{aligned}
\hat{E}(\boldsymbol{\Delta}_t^{i+1}) =& E(\mathbf{k}_{\text{myo},t}^{i} + \alpha\boldsymbol{\Delta}_t^{i+1} | \boldsymbol{\Psi}_t, \tilde{\boldsymbol{\Phi}}_t) \\
=& \sum_{m\sim n} \left[2\pi\alpha(\delta_{m,t}^{i+1} - \delta_{n,t}^{i+1}) + a_{m,n,t}^{i}\right]^2 + \sum_{m} \lambda_m \left[2\pi\alpha\delta_{m,t}^{i+1} + b_{m,t}^{i}\right]^2 \\
=& \sum_{m\sim n} E_1^{mn}(\delta_m^{i+1}, \delta_n^{i+1}) + \sum_{m} E_0^{m}(\delta_m^{i+1}). \\
a_{m,n,t}^{i} =& 2\pi(k_{m,t}^{i} - k_{n,t}^{i}) + \psi_{m,t} - \psi_{n,t} \\
b_{m,t}^{i} =& 2\pi k_{m,t}^{i} + \psi_{m,t} - \tilde{\phi}_{m,t}
\end{aligned} \tag{5.21}$$

We let E_1^{mn} and E_0^{m} denote the pairwise term and unary term in the energy function for simplicity. The iteration scheme is to update the wrap count map with a pair of operations: *up* and *down* operations. $\alpha = 1$ for *up* operation and $\alpha = -1$ for *down* operation. After each operation the wrap count at each pixel within the myocardium is updated with either a $\{0,1\}$ or a $\{0,-1\}$ binary value. From the research of [64], if a submodularity condition is met for all pairwise terms, then at each iteration $i+1$ the binary map $\mathbf{\Delta}_t^{i+1}$ can be optimized globally with a max-flow/min-cut algorithm, and the global optima of the wrap count image $\mathbf{k}_t$ can be reached after at most $2K$ iterations, where K is the maximum range of the wrap count. The pairwise term is submodular if and only if

$$E_1^{mn}(0,0) + E_1^{mn}(1,1) \leq E_1^{mn}(0,1) + E_1^{mn}(1,0). \tag{5.22}$$

Due to convexity of the quadratic term, we have the following inequality for any iteration step i and time t

$$\begin{aligned} E_1^{mn}(0,0) + E_1^{mn}(1,1) &= 2(a_{m,n,t}^{i})^2 \\ &\leq (a_{m,n,t}^{t} + 2\pi)^2 + (a_{m,n,t}^{t} - 2\pi)^2 = E_1^{mn}(0,1) + E_1^{mn}(1,0). \end{aligned}$$

Therefore, this submodularity condition holds for all pairwise terms. Because of this, the binary energy function in Equation 5.21 is *graph representable* [63] and the following graph can be constructed: let $\mathcal{G} = (\mathcal{V}, \mathcal{E})$ be a directed graph with $\mathcal{V} = \{v_1, ..., v_N, s, t\}$, where $N = |\mathcal{S}_{\mathrm{myo},t}|$ is the number of pixels within the segmented myocardium, $v_1, ..., v_N$ represent the binary variables $\mathbf{\Delta}_t^{i+1}$ and s (source) and t (sink) are terminals. Each s/t cut corresponds to a configuration of the variables $\delta_1, ..., \delta_N$ (here we omit the iteration $i+1$ and time t for simplicity) such that $\delta_m = 0$ when $v_m \in S$ and $\delta_m = 1$ when $v_m \in T$, where S and T are sets of vertices including source s and sink t, respectively. By properly constructing the graph, the total cost of the graph cut is equal to the value of the binary energy function, except for a constant offset. Therefore, the binary energy minimization is transferred to computing of the minimum s/t cut on graph $\mathcal{G}$. This minimum cut computation can be accomplished efficiently using the max-flow/min-cut algorithm [20, 63].

The graph construction consists of two steps [63]. First, an elementary graph is constructed for each energy term, either unary or pairwise. Then all the elementary graphs are merged to give the final graph $\mathcal{G}$. The procedure is illustrated in Figure 5.1. Figure 5.2 shows an example of the elementary graphs, where $E_0^m(1) \geq E_0^m(0)$, $E_1^{mn}(1,0) \geq E_1^{mn}(0,0)$, and $E_1^{mn}(1,0) > E_1^{mn}(1,1)$, as well as the final graph $\mathcal{G}$.

After the binary map $\mathbf{\Delta}_t^{i+1}$ is optimized by minimizing the binary energy function using max-flow/min-cut algorithm, the wrap count image is updated with $\mathbf{k}_{\text{myo},t}^{i+1} = \mathbf{k}_{\text{myo},t}^{i} + \alpha\mathbf{\Delta}_t^{i+1}$, where α alters between 1 and -1 for *up* and *down* operations. This updating process will repeat until the pair of *up* and *down* operations cannot further decrease the energy in Equation 5.8. The summary of the algorithm is listed in Algorithm 1.

Algorithm 1 Phase unwrapping with integer optimization

```
Input: Wrapped phase $\mathbf{\Psi}_t$; unwrapped phase from previous time $\mathbf{\Phi}_{t-1}$; index set $\mathcal{S}_{\text{myo},t}$; and
    clique set $\mathcal{C}$.
Output: Optimal wrap count image $\mathbf{k}_t$ and unwrapped phase $\mathbf{\Phi}_t = \mathbf{\Psi}_t + 2\pi\mathbf{k}_t$.
initial $\mathbf{k}_t = \mathbf{0}$, possible improvement = true.
while possible improvement do
    for $\alpha \in \{1, -1\}$ do
        Compute energy for each clique or pixel within $\mathcal{S}_{\text{myo},t}$.
        Construct graph $\mathcal{G} = (\mathcal{V}, \mathcal{E})$.
        Compute $s/t$ cut based on $\mathcal{G}$ and get $\mathbf{\Delta}_t$.
        $\mathbf{k}_{\text{myo},t} = \mathbf{k}_{\text{myo},t} + \alpha\mathbf{\Delta}_t$
    end for
    if $E(\mathbf{k}_t|\mathbf{\Psi}_t, \mathbf{\Phi}_{t-1})$ decreases then
        possible improvement = false.
    end if
end while
```

5.2.5 Segmentation and Strain Reconstruction

Segmentation is an important preprocessing step before phase unwrapping and following dense motion estimation and strain reconstruction. We adopt the same segmentation method that has been used in Chapter 4, which uses manually delineated myocardium contours for time frames near end-diastole (ED) and end-systole (ES) and propagates contours to all other frames with non-rigid registration [46, 137].

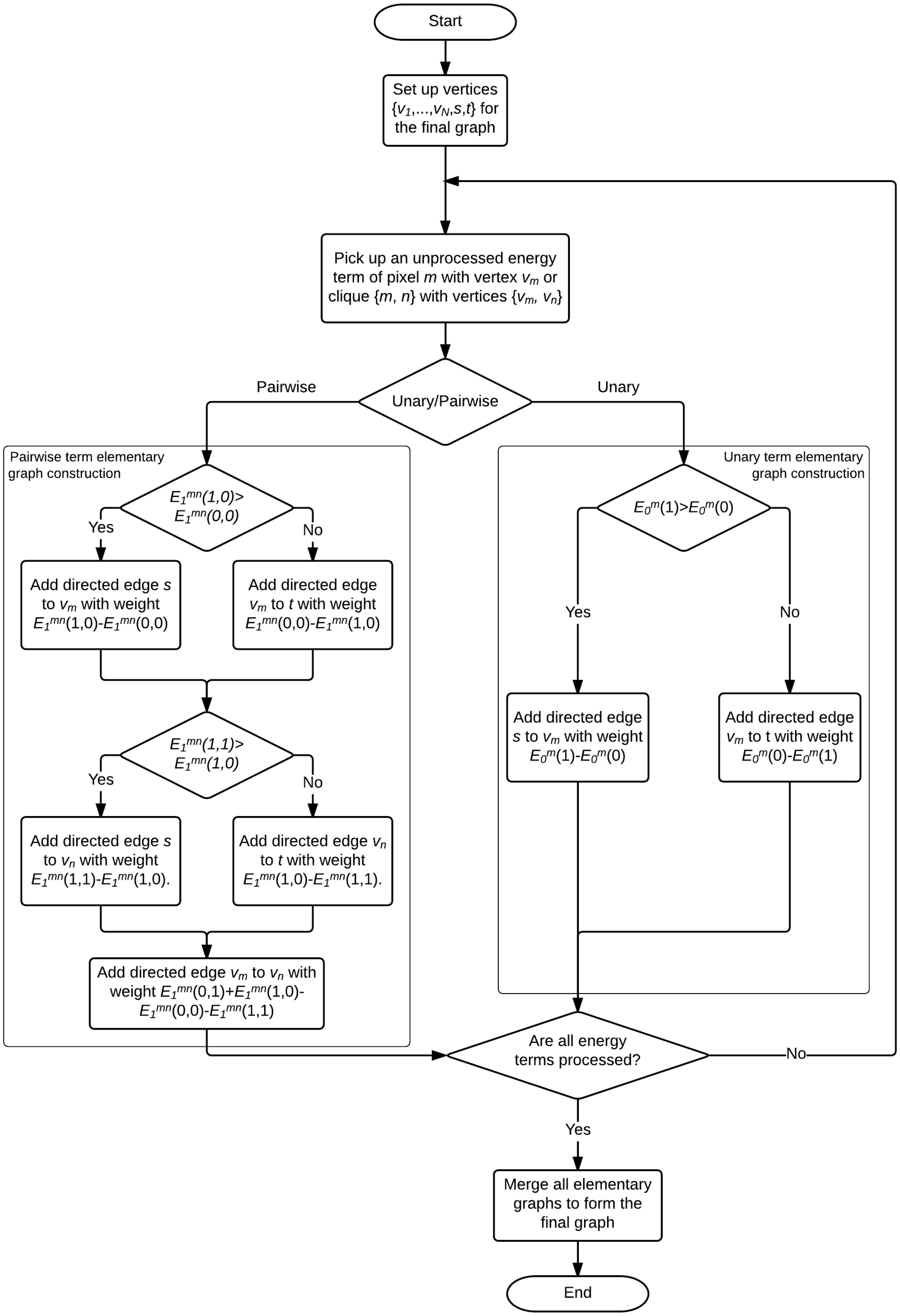

Figure 5.1: Flow chart of graph construction for first-order energy minimization.

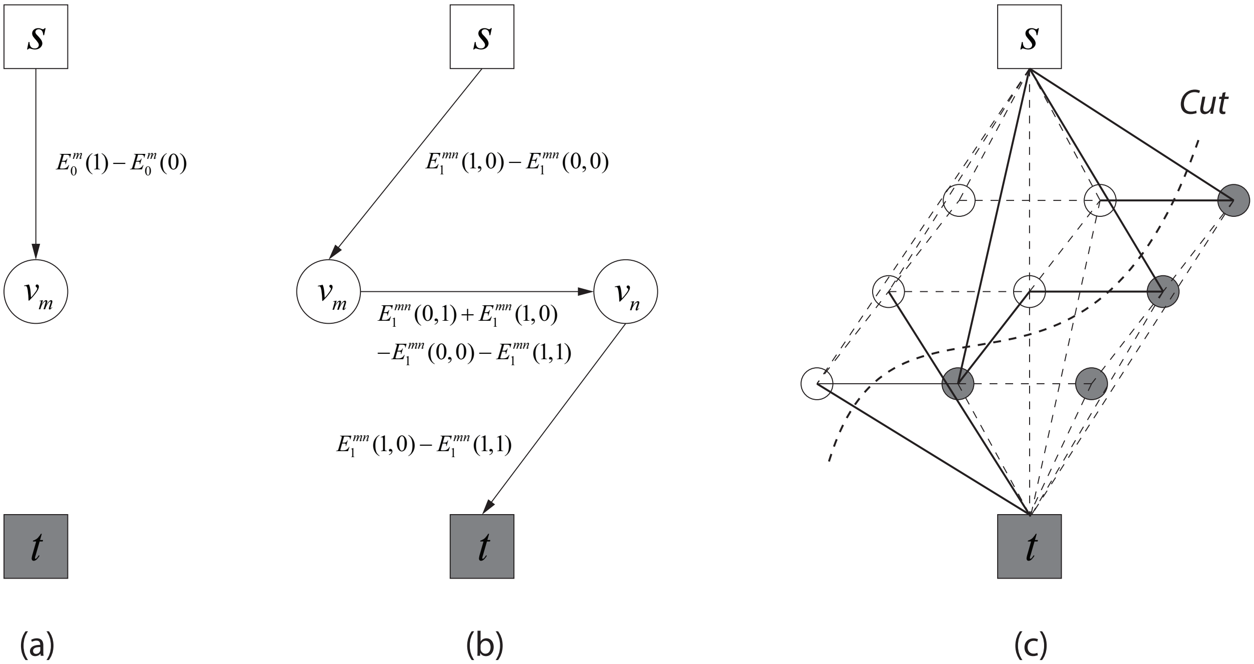

Figure 5.2: Illustration of elementary graphs and the final graph. s and t are terminal source and sink, respectively. v_m and v_n are two interactive vertices that corresponds to the two binary variables δ_m and δ_n. (a) is the elementary graph of an unary term, with $E_0^m(1) \geq E_0^m(0)$. (b) is the elementary graph of a pairwise term, with $E_1^{mn}(1,0) \geq E_1^{mn}(0,0)$, and $E_1^{mn}(1,0) > E_1^{mn}(1,1)$. (c) is the final graph after merging all elementary graphs. The cut divides vertices into two sets S and T, corresponding to the configuration of the variables $\mathbf{\Delta}$. Edges with weights counted in the cost of cut are shown with solid lines.

After automated phase unwrapping finishes, some unwrapped images may need manual corrections. We detect images with unwrapping errors by checking the difference between predicted unwrapped phase values and computed unwrapped values. If the ratio of pixels with a difference exceeding 2 (rad) is larger than ϵ, then we label this image as the one with unwrapping error, and we correct it by re-unwrapping with manually placed branch cuts under a graphic interface [120]. The threshold ϵ is set to be 0.2 for short-axis slices and 0.3 for long-axis slices. The threshold for long-axis slices is larger because typically the interframe deformation is larger at long-axis view and the real deformation can be more different from the assumed dynamic model.

After the process of myocardium segmentation and phase unwrapping for all demodulated HARP images at a certain time frame, 1D displacements at pixels within the myocardium can be computed for both short-axis and long-axis slices. Then these incomplete deformation measurements are used to interpolate a 3D dense deformation field and hence, the 3D strain map. In this research, we use a discrete model-free (DMF) method [40] for biventricular dense deformation field computation. The DMF method does not assume the geometry of the heart and therefore can be applied to both left and right ventricles. 3D Lagrangian strain maps are also computed from the dense deformation fields. We refer to this strain reconstruction method as Strain from Unwrapped Phase with Integer Optimization (SUPIO).

5.3 Experiments and Results

5.3.1 Materials

In this section we validate the proposed SUPIO method by testing on an *in-vivo* dataset of images acquired from 40 human subjects, including healthy volunteers (NL), patients with diabetes and myocardial infarction (DMI), resistant hypertension (HTN), and pulmonary hypertension (PAH). 10 out of 40 studies (4 NL, 3 DMI, and 3 HTN) are used for optimization parameter β. The rest 30 studies (10 NL, 5 DMI, 8 HTN, and 7 PAH) are used to validate the proposed SUPIO method by comparing resulted strains to other two manual methods.

All participants underwent the MRI scan on a 1.5 Tesla machine (GE Healthcare, Milwaukee, WI) optimized for cardiac application. 8 to 12 short-axis slices and 6 radially-prescribed long-axis slices were imaged with a fast gradient-echo cine sequence using the following parameters: field of view = 40×40 cm, scan matrix = 256×128, flip angle = 10°, repetition/echo time = 8.0/4.2 ms, views per segment = $8 \sim 10$, 20 time frames per cardiac cycle with a typical temporal resolution of 50 ms, slice thickness = 8 mm. Grid spatial modulation of magnetization (SPAMM) was applied to short-axis slices, while line tags were applied to long-axis slices. All tag lines were separated with a tag spacing of 7 pixels. The validation dataset with 30 human studies covered a wide diversity of human hearts including both geometries and motion patterns, and was also used in [121] to test the manually unwrapped phase-based method.

5.3.2 Parameter Selection

Parameters of Kalman filter were determined empirically using the 10 optimization dataset described before. Parameters of B-spline fitting are set to be $l = 3$, $p = q = 6$, and $\lambda = 1$. Parameters of Kalman filter are $T = 0.05$, $q_1^2 = 1, q_2^2 = 10$, $\bar{R} = 0.01$, $R = 1$, and $r^2 = 1$. $\bar{R}$ is set to be small because we used manually unwrapped phase to determine the mean locations of control points, and we want to retain these values without too much change throughout the cardiac cycle by using a smaller gain from the input residuals. Variation of the control point locations is set to be larger such that new observed values have a higher contribution to update current state variable values (locations and velocities).

For determination of the dynamic model frequency ω, we first observe a typical cardiac cycle and find that the systolic phase is shorter than the diastolic phase. If we treat the whole cardiac cycle as two joining half cycles, with different oscillating frequencies, the two frequencies can be approximated as $\omega_1 = \pi(N_{\text{frames}} - 1)/(I_{\text{ES}} - 1)$ and $\omega_2 = \pi(N_{\text{frames}} -$

$1)/(N_{\text{frames}} - I_{\text{ES}})$, where N_{frames} and I_{ES} are number of time frames in one slice (20 for the dataset in this research) and time index closest to ES. This modification will result in two versions of matrices F and Q, one for the systolic phase and the other for the diastolic phase.

The inverse temperature β which controls the balance between pairwise and unary terms is determined experimentally in this research. With a larger value of β we put more weight to spatial smoothness property of the true unwrapped phase image, and with a smaller value we put more weight to the predicted unwrap phase values, which are results from the Kalman filter. To optimize β, we tested a range of values ($\beta \in \{1, 5, 25, 125\}$) on the 10 human studies mentioned in Section 5.3.1, and compared unwrapping results at time frame closest to ES to the manually unwrapped results [121]. The test results are shown in Table 5.1. We set $\beta = 25$ which gives an overall best unwrapping result.

Table 5.1: RMSE of unwrapping differences (rad) at ES for different slice groups with different values of β compared to manual results. Base = Basal short-axis slices, Mid = Mid ventricular short-axis slices, Apex = Apical short-axis slices, Long = Long-axis slices.

	LV				RV			
β	Base	Mid	Apex	Long	Base	Mid	Apex	Long
1	0.2653	0.2554	0.3503	1.5620	0.9524	1.2687	0.2165	2.9441
5	0.2686	0.2593	0.5104	1.3808	0.9752	1.2118	0.2165	2.9623
25	0.2686	0.2574	0.6561	1.2332	0.9852	0.9099	0.2165	1.5475
125	0.2686	0.2574	1.1570	1.2988	1.2784	0.7472	0.2165	1.5475

5.3.3 Effect of Kalman Filter Prediction

In order to test the effectiveness of the addition of the Kalman filter prediction step, we unwrap the phase images from all 30 human studies, using the proposed SUPIO method (with Kalman filtering) as well as the one without Kalman filtering (as used in [70]). For the later method, computed unwrapped phase from previous time frame is used as the estimation of the current unwrapped phase image. The constant standard deviation is set as $\sigma_m = 1$, which approximately equals the average standard deviation using the proposed method when innovation covariance matrix S does not change much after a couple of Kalman filter updates. We select three time frames closest to 50%, 100%, and 150% of the systolic interval. Accuracies of the unwrapped phase images at these time locations are evaluated by comparing to unwrapped images with manually placed branch cuts [121]. Root mean square errors (RMSE) are computed for different axis views (short-axis and long-axis) and ventricles (LV and RV) for each single study. Notice that the unwrapped phase images are results of the automated processing [1] and no corrections are applied. Boxplots of the RMSEs are shown in Figure 5.3.

From the figure we can see the addition of Kalman filtering can improve the unwrapping accuracy, especially for time frames near end-systole (ES) and during the systolic phase. RV groups have higher improvement compared to LV groups. This is because RV region undergoes a larger interframe deformation typically, and the application of Kalman filtering can better predict the motion by assuming a periodic deformation pattern of the myocardium.

5.3.4 3D Biventricular Strain Validation

We validated the proposed SUPIO method for the 30 human studies. All studies were processed with procedures including myocardium contour segmentation, manual phase unwrapping at ES time frames (to provide information of control point mean locations), automated phase unwrapping, unwrapping correction, and 3D deformation field and strain reconstruction. The resulted strain parameters were compared to those obtained using other two manual methods. The first method used manually identified tag points for displacement measurements [40], referred as the feature-based method (FB). The second method used manually placed branch cuts to unwrap HARP images [121], referred as the manual strain from unwrapped phase method (mSUP). Paired t-test was used to compare resulted strains with different methods. A P-value greater than or equal to 0.05 was considered to be significant. Notice that all these three methods used DMF strain reconstruction. The only difference is the displacement measurement procedure.

---

[1] other than contouring and manual unwrapping at ES time frame (with Kalman filtering)

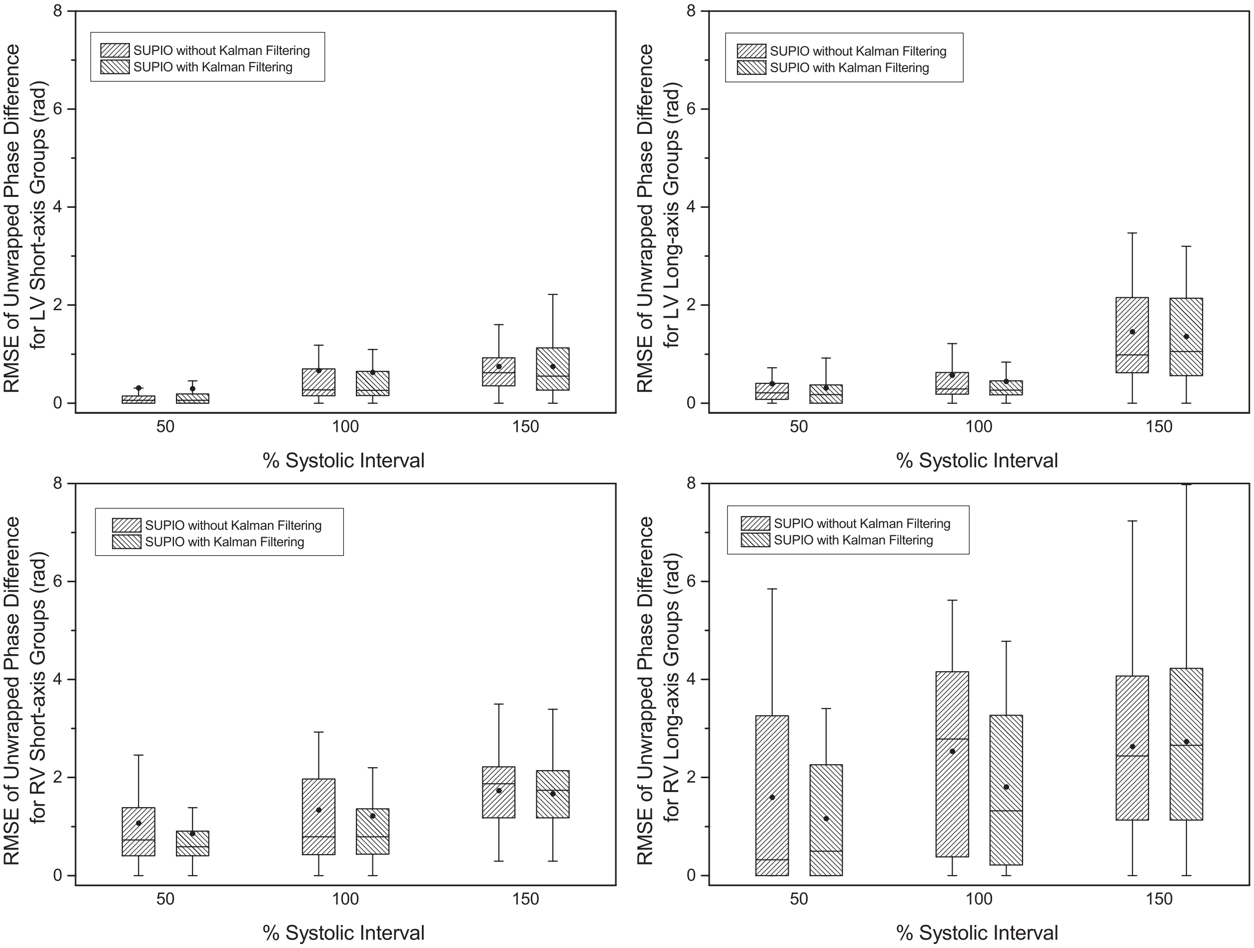

Figure 5.3: RMSE of the unwrapping differences at three different time locations (50%, 100%, and 150% of the systolic interval) using the proposed method (SUPIO with Kalman filtering) and the one without Kalman filtering for all 30 studies. Differences are grouped into four categories (LV short-axis, LV long-axis, RV short-axis, and RV long-axis).

All programs were implemented with MATLAB (The Mathworks Inc, Natick, MA) on a PC with Intel dual-core processer. For max-flow/min-cut computation we used a Quadratic Pseudo-Boolean Optimization (QPBO) algorithm [22, 23, 57, 62], the code of which was publically available. For a typical cardiac study, the processing time for manual contour delineation and propagation was 30 min. The time for manually unwrapping at ES time frames for Kalman filter start up (described in Section 5.2.3) was 5 min. The time for automated phase unwrapping was 5 min. The unwrapped phase correction step took 10 min, with a correction rate of 4% for all unwrapped images. The strain reconstruction using DMF method took 30 min. The overall processing time (excluding segmentation step) for a typical biventricular study with 8-12 short-axis slices and 6 long axis slices and 20 time frames is 50 min.

Table 5.2 shows the statistics of the difference in averaged mid-ventricular strains (unitless) and twist (degrees) at end-systole (ES) over the 30 studies between SUPIO and mSUP, SUPIO and FB methods. For comparison between SUPIO and FB methods, strains and twists except for RV tangential strains and RV longitudinal strains were not significantly different. Correlations between strains and twists using these two methods were quite high. Coefficients of variance (CV) were less than or equal to 2.10% for LV strains, 3.38% for twist, and less than or equal to 3.90% for RV strains. For comparison between SUPIO and mSUP methods, strains and twists were not significantly different. Correlations were higher than those between SUPIO and FB methods. CV were less than or equal to 1.49% for LV strains, 2.04% for twists, and less than or equal to 4.14% for RV strains. The differences between strains and twists from SUPIO and mSUP were smaller because both of these two methods use unwrapped phase images for displacement measurements.

Table 5.3 shows a comparison of peak strains (twists) and strain rates (twist rates) over the 30 studies between SUPIO and mSUP methods. All strains (twists) and strain rates (twist rates) were not significantly different. Peak strains (twists) show higher correlation

Table 5.2: Statistics of differences between strains (unitless) and twists (degrees) from SUPIO and FB, or SUPIO and mSUP methods for 30 validation studies at ES. Differences = Mean ± Standard Error. ρ = Correlation Coefficient. For all correlation coefficients, $p < 0.001$. CV = Coefficient of Variance. E_{cc} = LV circumferential strain. E_{ll} = LV longitudinal strain. E_{min} = LV minimum principal strain. $E_{\mathrm{tt}}RV$ = RV tangential strain. $E_{\mathrm{ll}}RV$ = RV longitudinal strain. $E_{\mathrm{min}}RV$ = RV minimum principal strain.

	SUPIO - FB				SUPIO - mSUP			
Strain	Differences	p	ρ	CV	Differences	p	ρ	CV
E_{cc}	0.0120 ± 0.0017	0.12	0.95	1.78%	0.0028 ± 0.0014	0.71	0.97	1.49%
E_{ll}	0.0083 ± 0.0023	0.39	0.94	2.10%	0.0030 ± 0.0014	0.76	0.98	1.29%
E_{min}	0.0065 ± 0.0020	0.44	0.94	1.48%	0.0026 ± 0.0010	0.76	0.99	0.73%
$Twist$	-0.9076 ± 0.1557	0.14	0.95	3.38%	-0.0149 ± 0.0873	0.98	0.97	2.04%
$E_{\mathrm{tt}}RV$	0.0223 ± 0.0035	0.01	0.84	3.90%	0.0052 ± 0.0035	0.56	0.85	4.14%
$E_{\mathrm{ll}}RV$	0.0211 ± 0.0031	0.03	0.90	2.97%	0.0071 ± 0.0022	0.46	0.95	2.27%
$E_{\mathrm{min}}RV$	0.0162 ± 0.0026	0.09	0.93	1.84%	0.0037 ± 0.0016	0.68	0.97	1.19%

than strain rates (twist rates). Correlations were lower for RV strain rates. CV were higher for RV strain rates.

Figure 5.4 shows mid-ventricular strains and twists averaged over four subject groups, i.e., normal volunteers (NL), diabetic patients with myocardial infarction (DMI), resistant hypertensive patients (HTN), and pulmonary hypertensive patients (PAH). Strain curves from the proposed SUPIO method are shown in blue. Curves from the mSUP and HARP strain method are shown in red and black, respectively. We can see that the two phase unwrapping-based methods provided similar results, whereas HARP strains showed slightly different values compared to the other two. This was because HARP strain technique computes 2D Eulerian strain, while the other two methods result in 3D Lagrangian strains. From these plots, lower strain and twist magnitudes for DMI and PAH groups compared to the other two groups are evident.

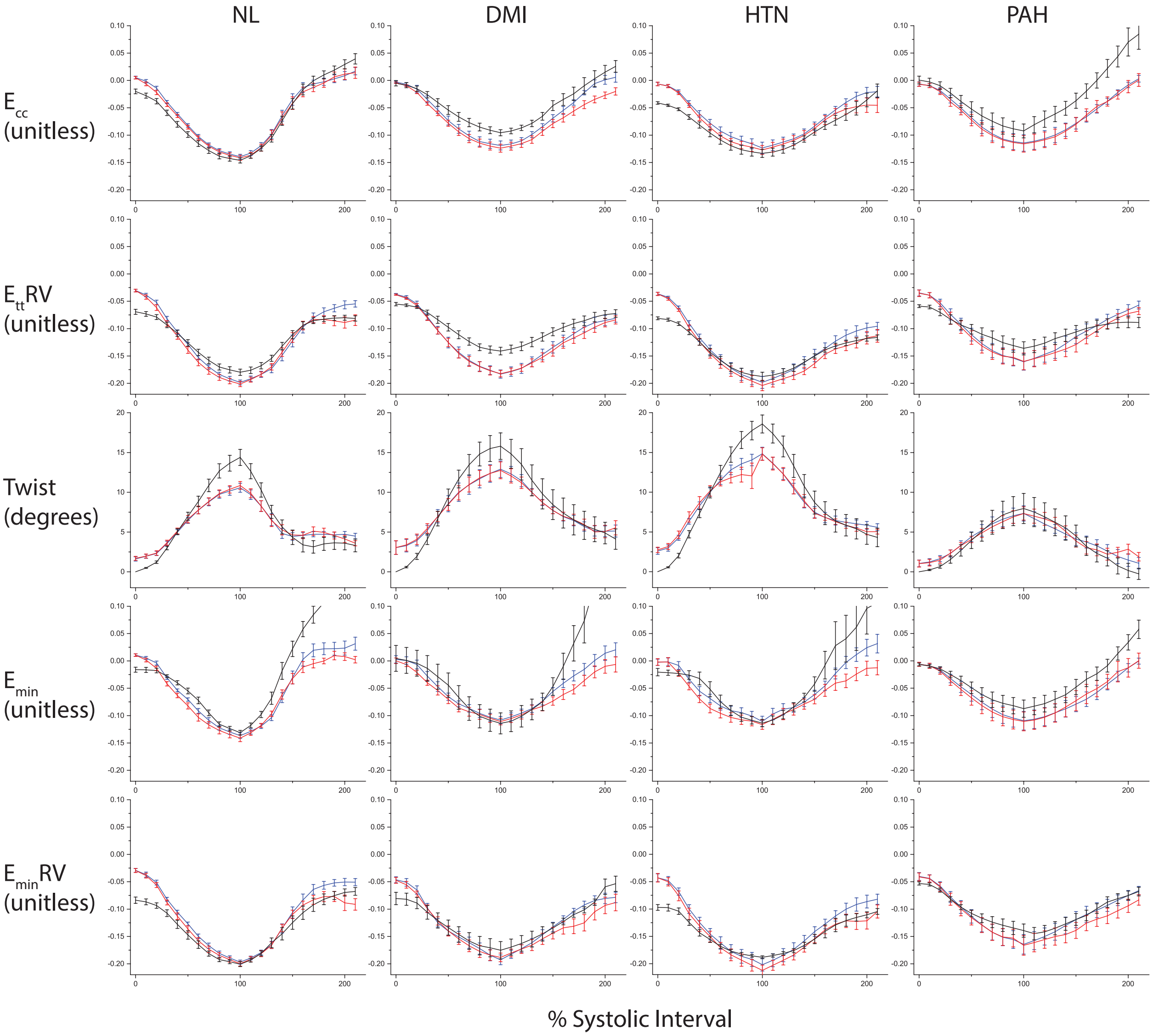

Figure 5.4: Plots of averaged mid-ventricular strains and twists obtained with the proposed SUPIO method (blue), the mSUP method (red), and HARP strain method (black), for normal volunteers (NL) and patients with diabetes and myocardial infarction (DMI), resistant hypertension (HTN), and pulmonary hypertension (PAH). Error bars represent ± one standard error.

Table 5.3: Comparison of peak strains (unitless), peak strain rates (1/sec), peak twists (degrees), and peak twist rates (degrees/sec) computed using the proposed SUPIO method and the mSUP method for 30 validation studies. Difference = Mean *pm* Standard Error. ρ = Correlation Coefficient. CV = Coefficient of Variance. E_{cc} = LV Circumferential Strain. $E_{\min}$ = LV Minimum Principal Strain. $E_{\mathrm{tt}}RV$ = RV Tangential Strain. $E_{\min}RV$ = RV Minimum Principal Strain. Peak = Peak (maximum/minimum) strain/twist during the cardiac cycle. Sys Rate = Peak systolic strain/twist rate. E Dia Rate = Peak early diastolic strain/twist rate.

	Strain	SUPIO - mSUP	p	ρ	p	CV
E_{cc}	Peak Strain	0.0029 ± 0.0003	0.69	0.97	< 0.001	1.50%
	Sys Rate	-0.0073 ± 0.0029	0.87	0.87	< 0.001	3.05%
	E Dia Rate	0.0355 ± 0.0044	0.55	0.83	< 0.001	4.60%
$E_{\min}$	Peak Strain	0.0022 ± 0.0002	0.80	0.98	< 0.001	0.89%
	Sys Rate	-0.0083 ± 0.0030	0.88	0.92	< 0.001	2.59%
	E Dia Rate	0.0363 ± 0.0051	0.50	0.74	< 0.001	5.67%
$Twist$	Peak Strain	-0.0625 ± 0.0250	0.95	0.98	< 0.001	1.65%
	Sys Rate	-0.6065 ± 0.1631	0.89	0.96	< 0.001	2.28%
	E Dia Rate	-0.6497 ± 0.4536	0.91	0.80	< 0.001	6.55%
$E_{\mathrm{tt}}RV$	Peak Strain	0.0038 ± 0.0005	0.64	0.89	< 0.001	3.13%
	Sys Rate	-0.0313 ± 0.0054	0.56	0.70	< 0.001	5.58%
	E Dia Rate	0.0657 ± 0.0068	0.38	0.76	< 0.001	6.23%
$E_{\min}RV$	Peak Strain	0.0034 ± 0.0004	0.70	0.95	< 0.001	1.41%
	Sys Rate	0.0033 ± 0.0081	0.96	0.56	0.001	7.04%
	E Dia Rate	0.0350 ± 0.0073	0.56	0.57	0.001	7.77%

5.4 Discussion and Conclusion

We improved the phase unwrapping process by incorporating a dynamic model and Kalman filtering process. Most of the Kalman filter parameters were determined empirically. Some of them have more influence on the filter performance and therefore should be determined with care, including B-spline parameters and variances $\bar{R}$, R and r^2.

We used manually unwrapped phase at end-systole time frame to initialize mean locations of B-spline control points. The expense is an extra 5 min of manual intervention per study. However, if we use an inferior estimation the Kalman filter predicting will become less accurate. One potential research topic is to find a better automated method for establishing initial state variables.

In this chapter we proposed a phase unwrapping technique based on integer optimization with graph cuts, as well as a dynamic model with Kalman filter. This phase unwrapping method was applied to unwrap demodulated HARP images computed from the tagged MR data. The displacement measurements were acquired from the unwrapped phase images and were further used to reconstruct the dense motion field and strain map. Compared to the quality-guided phase unwrapping method, which has been widely used in the general phase unwrapping problems, the proposed method is path-independent and is insensitive to the phase inconsistencies (residues) and can provide unwrapped phase images that are both spatially and temporally smooth. All these advantages make the proposed method ideal for unwrapping series of demodulated HARP images. Besides this, the proposed unwrapping method is computational efficient. The total operation time (excluding segmentation process) is 50 min for a typical cardiac study with 8-12 short-axis slices and 6 radial long-axis slices and 20 time frames. The phase unwrapping procedure takes 20 min, with 5 min automated processing and 15 min of manual intervention and corrections. We have greatly reduced the manual intervention rate compared to previous manual methods. We also validated the reconstructed strain parameters by comparing to other two manual methods using *in-vivo* data. The results show that the proposed SUPIO method can accurately reconstruct cardiac strains with significantly less time and user interaction.

Chapter 6

CARDIAC STRAIN ANALYSIS USING GABOR FILTER BANK AND POINT CLASSIFICATION WITH GRAPH CUTS

6.1 Introduction

As described in Chapter 2, several techniques have been developed to either manually or automatically measure myocardium deformation from the deformed tag pattern, including feature-based methods [31, 39, 40, 54], optical-flow methods [45, 94, 129], non-rigid registration-based methods [27, 65], and frequency-based methods like HARmonic Phase (HARP) [85, 86] and local sine wave modeling (SinMod) [15, 73].

HARmonic Phase (HARP) is a widely used technique. Since tagged images can be treated as AM-FM modulated 2D signals, local myocardial motion is encoded in the regional phase information. HARP computes this phase information from a complex image, which is produced by inverse Fourier transforming an isolated peak of the tagged MR image in the spatial frequency domain. The phase information is a material property and the same material point will retain the same phase value throughout the cardiac cycle, enabling tracking of the myocardium motion by tracking its phase value.

HARP is robust against noise, but, due to the bandpass filtering process, it constrains local variations in tag spacing and orientation because the location and shape of the bandpass filter are fixed. These constraints can cause artifacts such as branching and merging of the phase discontinuity when two tag lines get too close to each other in the original tag image, or breaking of the discontinuity when a large regional rotation is present. To address this issue, adaptive filtering methods such as Gabor filter banks [29, 100] have been developed. A Gabor filter is a complex-valued filter that is convolved with the original image enabling local periodic strip features to be extracted from the complex response. A large magnitude response suggests a higher match between the filter parameters and the local tag spacing and orientation. Therefore, by convolving the original image with a bank of Gabor filters with different combinations of parameters, one can estimate local features from the parameters of the filters that have the largest magnitude responses, and obtain a phase image from the optimal local complex responses.

Myocardial deformation can be estimated by unwrapping the phase image or using the wrapped phase information directly. The phase unwrapping process reconstructs the absolute phase by adding multiples of 2π to each pixel. The algorithm in [120, 121] requires manual intervention to correct the unwrapping process in regions where the wrapped phase is inconsistent. Tracking methods like HARP tracking [85] avoid the unwrapping process and estimates the motion field by tracking the local phase information. However, tracking errors may happen when the material point is tracked to an inconsistent position from the present time frame to the next, due to the presence of phase artifacts, through-plane motion, or large interframe deformation. In addition, when through-plane motion occurs, the radial positions of the tracked points tend to drift either to the epicardium or the endocardium, which can cause strain estimation errors [118].

An alternative to these phase-based methods is to extract tag lines or tag line intersections first, by detecting edges in the phase image. Gabor filter bank methods are sometimes used over HARP as the feature detection method because parameters of the Gabor filter are adjustable such that the local variation of tag spacing and orientation can be captured. Then the deformation field is estimated either by calculating the correspondence between detected tag lines and undeformed tag lines, or by tracking tag line intersection features between consecutive time frames as in [29], where a robust point matching algorithm (RPM) was used to match and track two intersection point sets in two consecutive time frames and an implicit deformable model was used to reconstruct a dense left ventricular deformation field. However, the RPM-based method in [29] ignores information about the underlying deformation that is contained in tag line points not on tag intersections. While loss of this information may not be an issue in the relatively thick-walled left ventricle, where there are many tag intersections, it can cause problems in the right ventricular wall, where tag intersections are sparse or non-existent.

In this research, we develop a deformation estimation method which uses Gabor filter banks to extract all tag line points in both the left and right ventricular walls and uses integer optimization to classify each point to a tag line. A deformation model is then fit to the tag points in each time frame of an image sequence and used to reconstruct dense motion field and strain in both the left and right ventricular walls. The classification algorithm assigns an integer tag line index to each tag point. It can be shown [42] that assigning a point to a particular tag line corresponds to a one-dimensional (1D) displacement of that point back to the undeformed tag line. The classification algorithm assigns indices to tag points so as to minimize the spatial variation in these 1D displacements between neighboring points. This smoothness constraint is formulated with a Markov Random Field (MRF), and the classification is performed iteratively with several binary optimization processes, which either change the index by 1 or keep it the same in each iteration. Binary optimization in each iteration is performed using a graph cuts method (max-flow/min-cut) [20, 64]. We refer to this proposed algorithm as the Point Classification with Graph Cuts (PCGC).

PCGC works best when the deformation field between a given time frame and the undeformed time frame is relatively small, which is not the case in many tagged cardiac imaging protocols, particularly near end-systole. To address this issue, we displace the extracted tag points in a given time frame by the inverse of the deformation field computed from the previous time frame. If the interframe motion is small, and the deformation field of the previous time is accurate, the tag points at a given time frame after compensation will be close to the undeformed tag line positions and can be accurately classified by the PCGC. After tag points from all tag groups (short-axis and long-axis view) are classified and the 1D displacements are computed, a 3D dense motion field and strains are reconstructed for both ventricles with the discrete model-free method [40].

This chapter is organized as follows: the Gabor filter bank tag identification method, the PCGC method along with the motion compensation, and the strain reconstruction are described in Section 6.2. Section 6.3 shows experimental results for *in-vivo* studies. Discussion and conclusion are presented in Section 6.4.

6.2 Methods

6.2.1 Gabor Filter Bank

To identify tag points in an image, we use Gabor filter banks similar to the ones used by [29]. A Gabor filter is a linear filter composed of a Gaussian kernel modulated by a sinusoidal plane wave

$$\begin{aligned} h(x,y) &= g(x',y') \cdot \exp(2\pi j \omega x') \\ &= A \cdot \exp(-\pi(a^2 x'^2 + b^2 y'^2)) \cdot \exp(2\pi j \omega x'), \end{aligned} \tag{6.1}$$

where $(x', y') = (x\cos\theta + y\sin\theta, -x\sin\theta + y\cos\theta)$ are the coordinates (x, y) rotated by the tag line angle θ, ω is the spatial frequency of the sinusoidal carrier, A is the magnitude of the Gaussian envelope, and a and b control the shape of the envelope.

After 2D Fourier transform, the Gabor filter in frequency domain has a simpler form

$$\hat{h}(u,v) = \frac{A}{ab}\exp\left(-\pi\left(\frac{(u-u_0)^2}{a^2} + \frac{(v-v_0)^2}{b^2}\right)\right), \tag{6.2}$$

where $(u_0, v_0) = (\omega\cos\theta, \omega\sin\theta)$ are frequency components of the carrier in the spatial domain. In this research, we chose $a = b = \sqrt{A} = \omega/\sqrt{2\pi}$.

The 5×3 array of Gabor filters shown in Figure 6.1 defines a bank [29], where the frequency varies from $0.5\omega_0$ to $2\omega_0$ with an increment of $\sqrt{2}$ in scale and the orientation varies from $\theta_0 - \pi/8$ to $\theta_0 + \pi/8$ with an increment of $\pi/8$. Parameters of the filter in the center of the bank, (ω_0, θ_0), are determined by tag line modulation frequency and orientation from the image acquisition protocol. In this example, where tag modulation is 45 degree

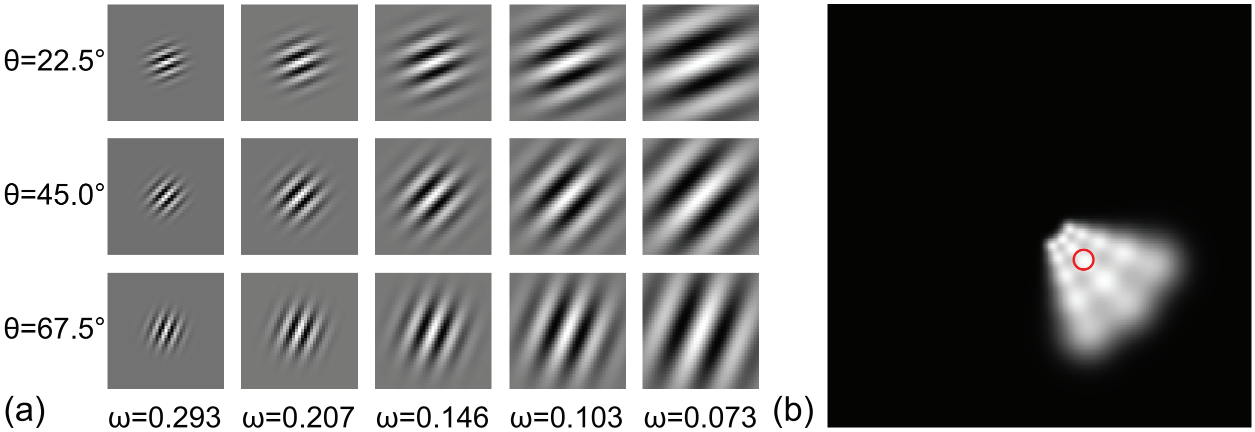

Figure 6.1: Gabor filter bank in (a) spatial domain (showing only the real part) and (b) frequency domain. Gabor filter in center of (a) and denoted with red circle in (b) has parameters of $\omega = 0.1467, \theta = \pi/4$.

and tag spacing (T) is 6.8 pixels, the Gabor filter bank is designed with ($\omega_0 = 1/T = 0.1467, \theta_0 = \pi/4$). For image with -45° modulation and the same tag spacing, the Gabor filter bank applied is rotated by 90° with ($\omega_0 = 0.1467, \theta_0 = -\pi/4$).

For grid-tagged images, Gabor filters could be applied directly to the image, but this sometimes results in the detection of spurious tag points near borders of the myocardium and near intersections. In this reseach, we use strip filters of width $1/T$ to isolate tag lines in each orientation as shown in Figure 6.2 and apply a Gabor filter bank to each resulting line-tagged image.

Since the filters in the bank are relatively coarsely sampled in frequency and orientation, the optimal frequency and orientation for a particular pixel must be interpolated from the parameters of the filters with the highest magnitude responses. In [29], the optimal parameters were computed using a weighted average of the the parameters of the K highest magnitude response filters, where the weight for the kth filter at pixel i was defined as $w_{i,k} = m_{i,k}/\sum_{\kappa=1}^{K} m_{i,\kappa}$ and $m_{i,k}$ is the magnitude response of the kth filter at pixel i. Similarly, the magnitude and phase response at each pixel was computed from a weighted

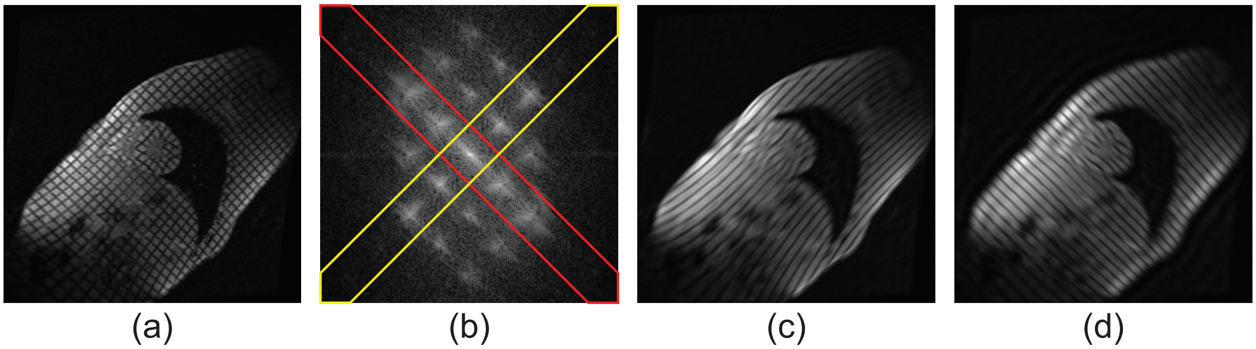

Figure 6.2: Illustration of pre-filtering process for grid tagged images. (a) Short-axis cardiac tagged image near mid-ventricle and end-systole. (b) Fourier transform magnitude of the image in (a). The strip filter enclosed with red lines preserves tag line with 45° orientation and removes tag lines of $-45°$ as shown in (c). The filter enclosed by yellow lines does the opposite as shown in (d).

average of the filter bank real and imaginary responses [29]. [29] used $K = 3$. In this research, we computed a weighted average over all filters ($K = 15$), which was a bit faster computationally since it was not necessary to sort the magnitude responses at each pixel.

Tag line points were identified inside the myocardium by detecting the locations where the phase response wrapped from $-\pi$ to π. The myocardium in both ventricles was segmented using endocardial and epicardial contours constructed with a dual-contour propagation technique developed by our group [46, 137] and used in several clinical studies [5, 6, 7, 43, 52, 90, 110, 111]. This technique uses manually-drawn contours in time frames near end-diastole (ED) and end-systole (ES) to automatically propagate contours to all remaining time frames using non-rigid registration. ED and ES contours are typically drawn during clinical analysis of cardiac MRI data to compute functional parameters. A typical tag line point identification result near end-systole is shown in Figure 6.3.

6.2.2 Point Classification with Graph Cuts (PCGC)

In this section, we describe the PCGC algorithm, which assigns an integer tag line index to each tag point assuming the underlying deformation is spatially smooth and small

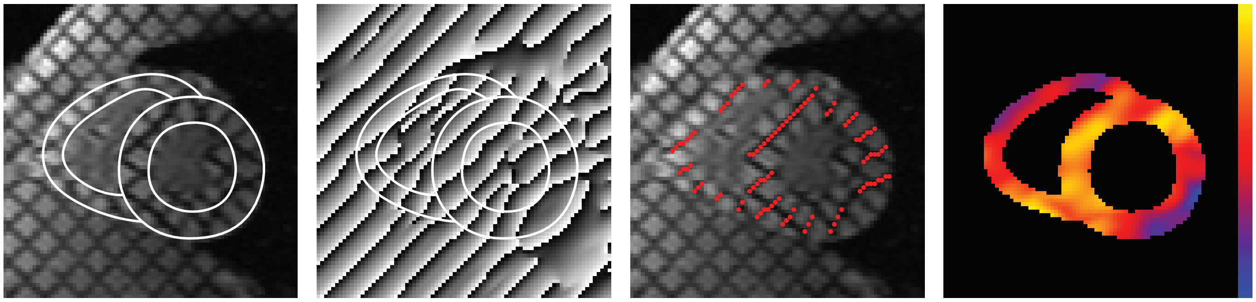

(a) (b) (c) (d)

Figure 6.3: Example of feature extraction. White borders are myocardial contours. (a) is the tagged MR image at end-systole. (b) is the phase map computed after interpolation of the complex responses from the Gabor filter bank centered at $(0.1467, \pi/4)$. (c) shows the detected tag points using the phase map from (b). Only points within contours were displayed. (d) is the estimated tag frequency map using the optimal interpolated filter parameters. The frequency ranges from 0.13 pixel^{-1} (blue) to 0.18 pixel^{-1} (yellow).

in magnitude.[1] We assume that each tag line was straight when originally applied to the tissue (i.e. undeformed) and each identified tag point belongs to only one tag line. We refer to tag lines at their undeformed position as reference tag lines.

Let Ω be the index set of all detected tag points, and each candidate reference tag line be labeled as $l \in \{0, 1, ..., N-1\}$, where N is the number of all candidates. The classification problem can be framed as follows: for each tag point $p \in \Omega$ with coordinate vector $\mathbf{p} = [x_p, y_p]'$ ($[\cdot]'$ denotes transpose), it is assigned a label l_p, indicating that the deformed tag point p moved from its original position, which was on the reference tag line with label l_p. The 1D displacement from p along the normal direction of the reference tag line is given by

$$u_p = \mathbf{n}^T \mathbf{p} + c_{l_p}, \tag{6.3}$$

where $\mathbf{n} = [\cos\theta, \sin\theta]'$ is the reference tag line normal vector, and c_{l_p} is the offset of the reference tag line with label l_p, defined by the line equation: $x\cos\theta + y\sin\theta + c_{l_p} = 0$ for any point (x, y) on the reference tag line. c_{l_p} is a one to one function of label l_p. When all

---

[1] The small deformation assumption requires a motion compensation algorithm, which we describe in Section 6.2.3

reference tag lines are separated by the same distance, which is the case in this research, c_{l_p} is a linear function of l_p, and we have $c_{l_p} = c_0 + Tl_p$, where $T > 0$ is the spacing between tag lines.

From Equation 6.3 and Figure 6.4 we can see that different labeling schemes result in different displacement patterns. We assume that spatially neighboring tag points should have similar 1D displacements and that the 1D displacement of a point is small. These two assumptions result in the following energy function of the label set for all tag points $L = \{l_p, p \in \Omega\}$:

$$\begin{aligned} E(L) &= \sum_p \sum_{q \in \mathcal{N}(p)} V(u_p - u_q, d_{pq}; \eta_p) + \lambda \sum_p u_p^2 \\ &= \sum_p \sum_{q \in \mathcal{N}(p)} U_1(l_p, l_q) + \lambda \sum_p U_0(l_p), \end{aligned} \tag{6.4}$$

where $p, q \in \Omega$ are two tag points in the domain. $q \in \mathcal{N}(p)$ indicates that q belongs to the neighborhood of p. $V(\cdot)$ is a convex pairwise potential function, which penalizes differences in displacement. $V(\cdot)$ and the neighborhood are defined below. u_p and u_q are 1D displacements defined in Equation 6.3 at point p and q with coordinate vectors $\mathbf{p}$ and $\mathbf{q}$. $d_{pq} = \|\mathbf{p} - \mathbf{q}\|_2$ is the Euclidean distance between the two tag points. λ is a weight that balances the influence of the pairwise and unary potentials. The pairwise term U_1 penalizes the displacement difference between two tag points. The unary term U_0 penalizes large displacements. The unary constraint is needed to obtain a unique solution for L. Without the unary term, when tag lines are evenly separated and c_{l_p} is a linear function of label l_p, there will be multiple optimal solutions of L differing from each other by an integer shift. Cardiac deformation, particularly near end-systole, involves large displacements, so we use the motion compensation technique described in Section 6.2.3 to reduce tag point displacements to a level where the small displacement assumption is valid.

The pairwise potential function $V(\cdot)$ in Equation 6.4 is defined as

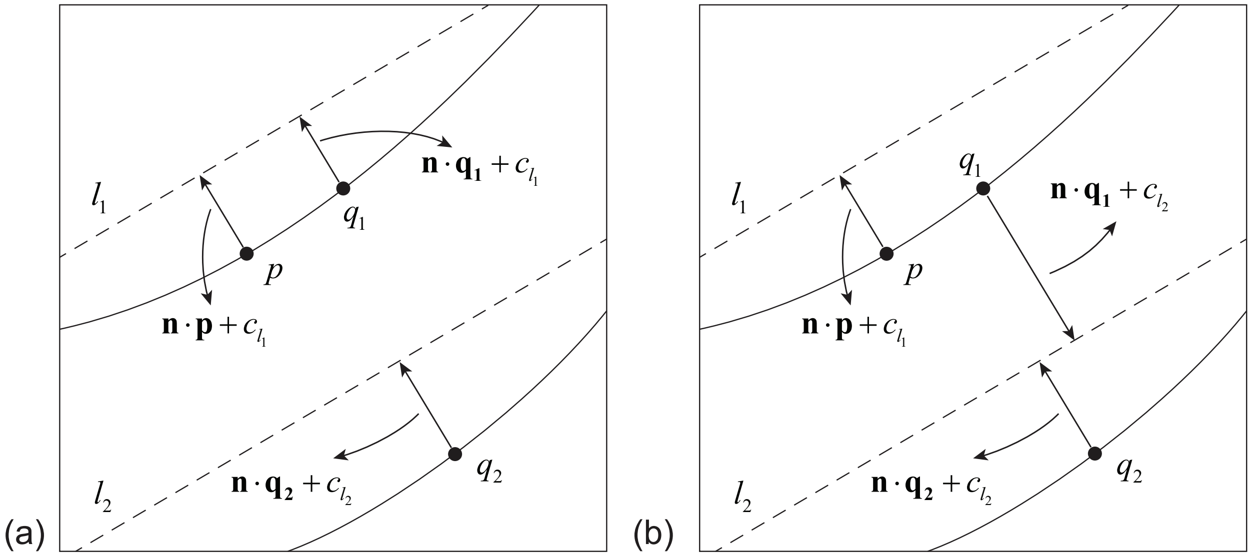

Figure 6.4: Two examples of label configurations - one resulting in a smooth deformation pattern (a) and one resulting in a nonsmooth deformation pattern (b). Two dotted reference tag lines are labeled as l_1 and l_2. $\mathbf{n}$ is the normal vector of the reference tag lines. p, q_1, and q_2 are detected tag points with coordinate vectors $\mathbf{p}$, $\mathbf{q_1}$, and $\mathbf{q_2}$.

$$V(a,b;\eta) = a^2\phi(b;\eta) = a^2\exp(-\eta^2 b^2), \tag{6.5}$$

where $\phi(\cdot)$ is a Gaussian radial basis function. This term serves as a membership weight to control the interaction between any two neighboring tag points. When two tag points are more separated, the membership weight decreases and the displacement difference is less penalized. The neighborhood $\mathcal{N}(p)$, for tag points p and q, is defined as $q \in \mathcal{N}(p)$ if and only if $\phi(d_{pq}) \geq \tau$. We set threshold $\tau = 0.1$ in this research.

The radial basis function is defined such that, as η decreases, the Gaussian weighting pattern is wider. Typically, η (and the corresponding neighborhood size) is fixed. However, in this research, we set $\eta = \eta_p = \omega_p$, the local tag frequency or the reciprocal of local tag spacing at point p, acquired from the estimated frequency map in Figure 6.3(d). This allows the neighborhood to get smaller as the heart contracts and vice versa.

The energy function in Equation 6.4 conforms to a first-order Markov Random Field (MRF), which needs to be minimized over the label set L. This combinatorial optimization problem can be solved with several discrete optimization schemes [33, 64]. In this research, we initialized the label set as $L^i = \mathbf{0}$ at step $i = 0$ and optimized L by iteratively adding binary values to it: $L^{i+1} = L^i + \Delta$, where $\Delta = \{\delta_p \in \{0, 1\}, p \in \Omega\}$. The optimal value of Δ at each iteration is obtained by minimizing the following energy function

$$\begin{aligned} \hat{E}(\Delta) = & \quad E(L^i + \Delta) \\ = & \sum_p \sum_{q \in \mathcal{N}(p)} U_1(l_p^i + \delta_p, l_q^i + \delta_q) + \lambda \sum_p U_0(l_p^i + \delta_p) \\ = & \sum_p \sum_{q \in \mathcal{N}(p)} E_1(\delta_p, \delta_q) + \sum_p E_0(\delta_p) \,. \end{aligned} \tag{6.6}$$

Similarly, the binary function $\hat{E}(\Delta)$ is composed of pairwise and unary terms, where $E_1(\cdot)$ is the first-order clique energy function of a pair of binary variables, and $E_0(\cdot)$ is the zeroth-order clique energy function of a single binary variable. According to discussions in Chapter 5, when submodularity condition is met for all pairwise terms, the binary energy at each step can be minimized globally by finding the minimum cut on the corresponding graph, and the optimal label set L can be obtained by iteratively optimizing Equation 6.6 $N - 1$ times or until no potential improvement can be done to decrease the energy in Equation 6.4. It is easy to show that the submodularity condition holds for each pairwise term of the binary energy function in Equation 6.6. Due to convexity, we have the following inequality for each pair of tag points (p, q)

$$\begin{aligned} & E_1(0,1) + E_1(1,0) = \\ & \qquad \phi(d_{pq}; \eta_p) \cdot ((\mathbf{p} - \mathbf{q})^T \mathbf{n} + T(l_p^i - l_q^i) - T)^2 \\ & \qquad + \phi(d_{pq}; \eta_p) \cdot ((\mathbf{p} - \mathbf{q})^T \mathbf{n} + T(l_p^i - l_q^i) + T)^2 \\ & \quad \geq 2\phi(d_{pq}; \eta_p) \cdot ((\mathbf{p} - \mathbf{q})^T \mathbf{n} + T(l_p^i - l_q^i))^2 \\ & \quad = E_1(0,0) + E_1(1,1) \,. \end{aligned} \tag{6.7}$$

Since the submodularity condition is met, the binary energy function is *graph representable* and a corresponding graph can be constructed. Then the binary optimization problem is transferred to finding the minimum cut on this graph, which can be efficiently computed using a max-flow/min-cut algorithm. Details of the graph construction has been introduced in Chapter 5.

After the binary set Δ is optimized by minimizing the energy function using max-flow/min-cut algorithm, the label set L is updated with $L^{i+1} = L^{i} + \Delta$. This process repeats until no potential improvement can be done to decrease the energy, or the maximum label $N - 1$ is reached. Note that the set of candidate tag lines should cover as many probable reference tag lines as possible, in order to prevent a situation where the optimal labels of some of the tag points are outside the range of the set. On the other hand, the set should cover as few candidates as possible to reduce processing time, because, at each step, a new graph is constructed and the max-flow/min-cut algorithm is run. In this research, for an image sequence the candidate tag lines are selected in following ways: we first determine the region of interest (ROI) covering the left and right ventricular myocardium at the time closest to end-diastole (ED), with an extra extension of 5 pixels; we then select candidate tag lines passing through the ROI at their undeformed positions. The pseudo code of PCGC is provided in Algorithm 2.

Algorithm 2 Point Classification with Graph Cuts

```
Input: Tag line labels $\{0, ..., N-1\}$; neighborhood $\mathcal{N}(p)$ and $\phi(d_{pq})$ for each $p$ and $q \in \mathcal{N}(p)$.
Output: Optimal label set $L$.
initial $i = 0$, $L^{i} = \mathbf{0}$, possible improvement = true
while possible improvement and $i + 1 < N$ do
    Compute binary energies for each tag point and pair of tag points.
    Construct graph $\mathcal{G} = (\mathcal{V}, \mathcal{E})$.
    Compute $s/t$ cut based on $\mathcal{G}$ and get $\Delta$.
    if $E(L^{i} + \Delta) < E(L^{i})$ then
        $L^{i+1} = L^{i} + \Delta$, $i = i + 1$
    else
        possible improvement = false
    end if
end while
```

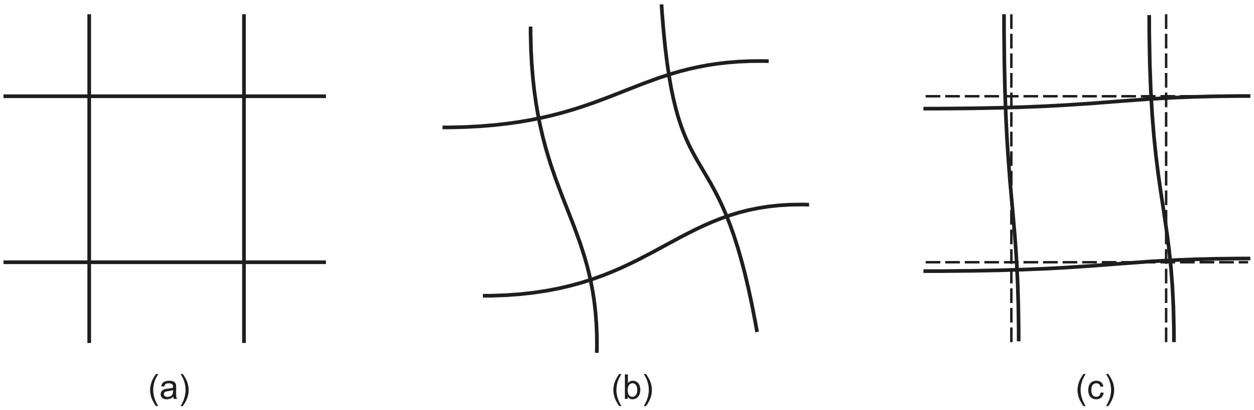

Figure 6.5: Illustration of motion compensation. (a) shows tag lines at their initial positions without deformation. (b) shows the deformed tag lines. (c) is the result after motion compensation. Dashed lines are reference positions.

6.2.3 Motion Compensation and Strain Reconstruction

As mentioned earlier, the PCGC algorithm assumes small displacements from the undeformed tag line, which is a poor assumption in cardiac motion. To make the PCGC algorithm applicable to tagged images with large displacements, we use a motion compensation technique, which transforms tag points at a deformed time frame to new positions that are close to the reference tag line positions. Figure 6.5 is an illustration of this process. The 1D tag point displacements in Equation 6.4 are computed from the motion compensated tag point positions, whereas the distance between tag points d_{pq} in Equation 6.4 and the neighborhood system are determined from the original (not motion compensated) tag point locations.

Several methods can be used for motion compensation. In this research, we used a 2D version of the discrete model-free (DMF) algorithm [40] to reconstruct a dense deformation field from sparse displacement measurements. The DMF algorithm uses a finite difference-based technique to map tag points in a deformed configuration back to their (undeformed) reference position. In the PCGC algorithm, tag points in the first imaged time frame are assumed to have small displacements, so they are classified with no motion compensation. In subsequent time frames, each tag point location is compensated with the dense deformation map computed from the classified tag points at the previous time frame using the 2D DMF algorithm.

After all tag points were detected and classified using the PCGC, 1D displacement measurements are computed from the classified tag points. At each time frame, there are 1D displacement measurements from all tag line orientations. We use the original 3D DMF method to estimate a 3D dense deformation field and to compute 3D biventricular Lagrangian strain. This process is repeated for each time frame to compute 3D+time biventricular strain as was done in previous work [121].

6.3 Experiments and Results

In this section, we evaluate the performance of the PCGC and validate the reconstructed biventricular strains with *in-vivo* data. A total of 40 human studies were used, including images from normal volunteers (NL) and patients with pathologies including diabetes with infarction (DMI), resistant hypertension (HTN) and pulmonary arterial hypertension (PAH). 10 studies (4 NL, 3 DMI, and 3 HTN) out of the dataset were selected randomly and used to optimize the parameter λ. The proposed method was tested on the remaining 30 studies (10 NL, 5 DMI, 8 HTN, and 7 PAH) and then validated by comparing the reconstructed strains to those obtained with a feature-based method with edited tag points [39, 40] and a manually unwrapped phase-based method [121].

All participants underwent the MRI scan on a 1.5 Tesla machine (GE Healthcare, Milwaukee, WI) optimized for cardiac application. $8 - 12$ short-axis slices and 6 radially-prescribed long-axis slices were imaged with a fast gradient-echo cine sequence using the following parameters: field of view = 40×40 cm, scan matrix = 256×128, flip angle = 10°, repetition/echo time = 8.0/4.2 ms, views per segment = $8 \sim 10$, 20 time frames per cardiac cycle with a typical temporal resolution of 50 ms, slice thickness = 8 mm. Grid spatial modulation of magnetization (SPAMM) was applied to short-axis slices, while line tags were applied to long-axis slices. All tag lines were separated with a tag spacing (T) of

7 pixels. The validation dataset with 30 human studies covered a wide diversity of human hearts including both geometries and motion patterns, and was also used in [121] to test the manually unwrapped phase-based method.

Preparation of these cardiac studies included myocardium segmentation, for which we used the dual-contour propagation method [46, 137] introduced previously in Section 6.2.1. First, we manually drew epicardial and endocardial contours for both left ventricle (LV) and right ventricle (RV) near end-diastole (ED) and end-systole (ES). Then contours were automatically propagated to all other time frames with the dual-contour method. The contouring and propagation took approximately 30 minutes for each study. Contouring was the only manual intervention used in the study. Once the contours near ED and ES were specified, the remaining processing was fully automatic, and no editing of tag points was performed in this research.

All programs were implemented with MATLAB (Mathworks, MA) on a laptop computer with Intel Core i5 CPU (2.27 GHz). We used a Quadratic Pseudo-Boolean Optimization (QPBO) algorithm [22, 23, 57, 62] for the max-flow/min-cut computation, the code of which was publicly available. Though the algorithm was implemented for Markov random field problems with nonsubmodular terms, it also can be used for submodular problems. The processing time with the proposed method (including Gabor filtering, PCGC and motion compensation) was 1 minute for a typical cardiac slice composed of 20 256×256 pixel images with grid tags. 3D+t strain computation using the DMF method for a typical cardiac study was 30 min. A typical cardiac imaging study with 10 short-axis slices and 6 long-axis slices required 30 minutes for contouring followed by 44 minutes of automated processing.

6.3.1 Optimization of λ

We optimized the parameter λ in Equation 6.4 on a set of 10 human studies which were not part of the validation dataset. For different choices of λ values ($\lambda \in \{10^{-4}, 10^{-3}, 10^{-2}, 10^{-1}, 1\}$), we compared 1D displacements of tag points identified and classified with the PCGC to

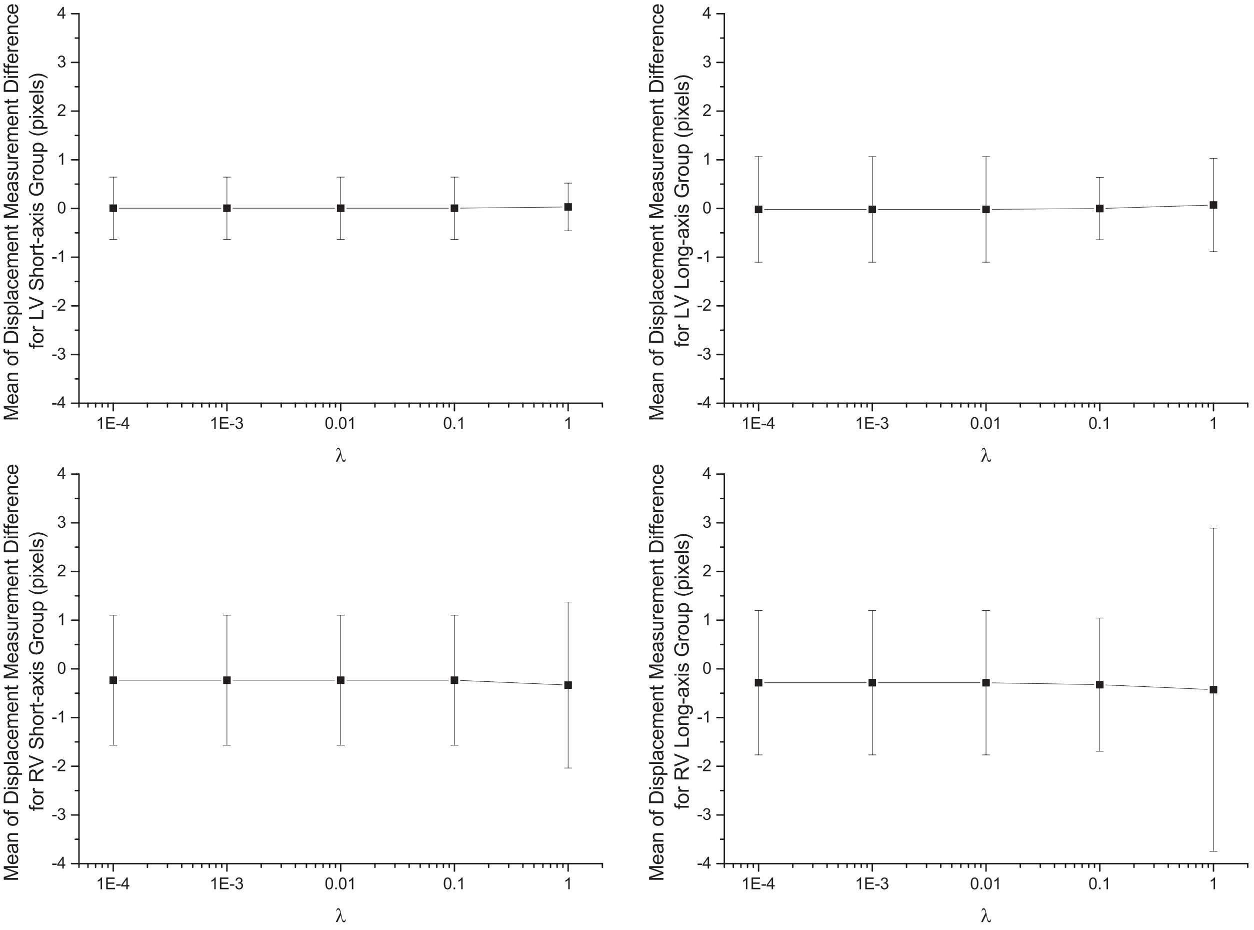

Figure 6.6: Mean 1D displacement measurement differences at ES with different choices of λ for (upper left) LV short-axis groups, (upper right) LV long-axis groups, (lower left) RV short-axis groups, and (lower right) RV long-axis groups from the 10 human studies. Manually identified tag points were used for comparison. Error bar represents one standard deviation.

those from manually identified tag points at the time frame closest to end-systole. Figure 6.6 shows the mean and standard deviation of the displacement measurement differences for LV short-axis groups, LV long-axis groups, RV short-axis groups, and RV long-axis groups. We conclude that the PCGC algorithm is not sensitive to choices of λ values less than or equal to 0.1. We used $\lambda = 0.01$ for the following validation experiment.

6.3.2 *In-vivo* Validation Experiment

In order to validate the proposed method on the set of 30 human subjects described previously, tag points were manually identified and edited at the time frame nearest end-systole in each study by an expert user. Accuracy of tag points detected and classified by the PCGC was evaluated by comparing the 1D displacement measurements from classified tag points to those from the manually identified tag points. Figure 6.7 shows plots of the differences for short- and long-axis slices in both the RV and LV. The displacement measurement differences were -0.002 ± 0.442 (pixels) for LV short-axis groups, -0.061 ± 0.69 (pixels) for LV long-axis slices, -0.009 ± 0.880 (pixels) for RV short-axis slices, and -0.337 ± 1.879 (pixels) for RV long-axis slices. The classified tag point locations were notably less accurate for RV than for LV. There are multiple reasons for this difference in accuracy. First, due to the thinness of the RV free wall, accuracy of the deteted tag points can be largely affected by the noisy signal present over the myocardium. Second, the endocardial and epicardial boundaries of the RV can sometimes look like tag lines. Third, the interframe deformation of RV free wall, especially at long-axis view, is larger in the RV relative to the LV.

Strains were computed in regions defined by the American Heart Association (AHA) 17 segment model [26] excluding the apex. RV free wall strains were computed on a similar model adapted to the RV. LV and RV cardiac strain parameters (unitless) were averaged over the mid-ventricular segments. We also computed LV twist (in degrees), which was defined as the rotation angle difference between LV apex and base [132].

We compared the resulted strain parameters from the proposed method (PCGC tag point classification and DMF strain reconstruction) to those from two other methods. The first method used manually identified tag points at end-systole (ES) as described above [40]. The second method used unwrapped HARP images from all time frames with manually placement branch cuts and quality-guided phase unwrapping for 1D displacement measurements [121]. For both of these methods, the DMF strain reconstruction was used, resulting

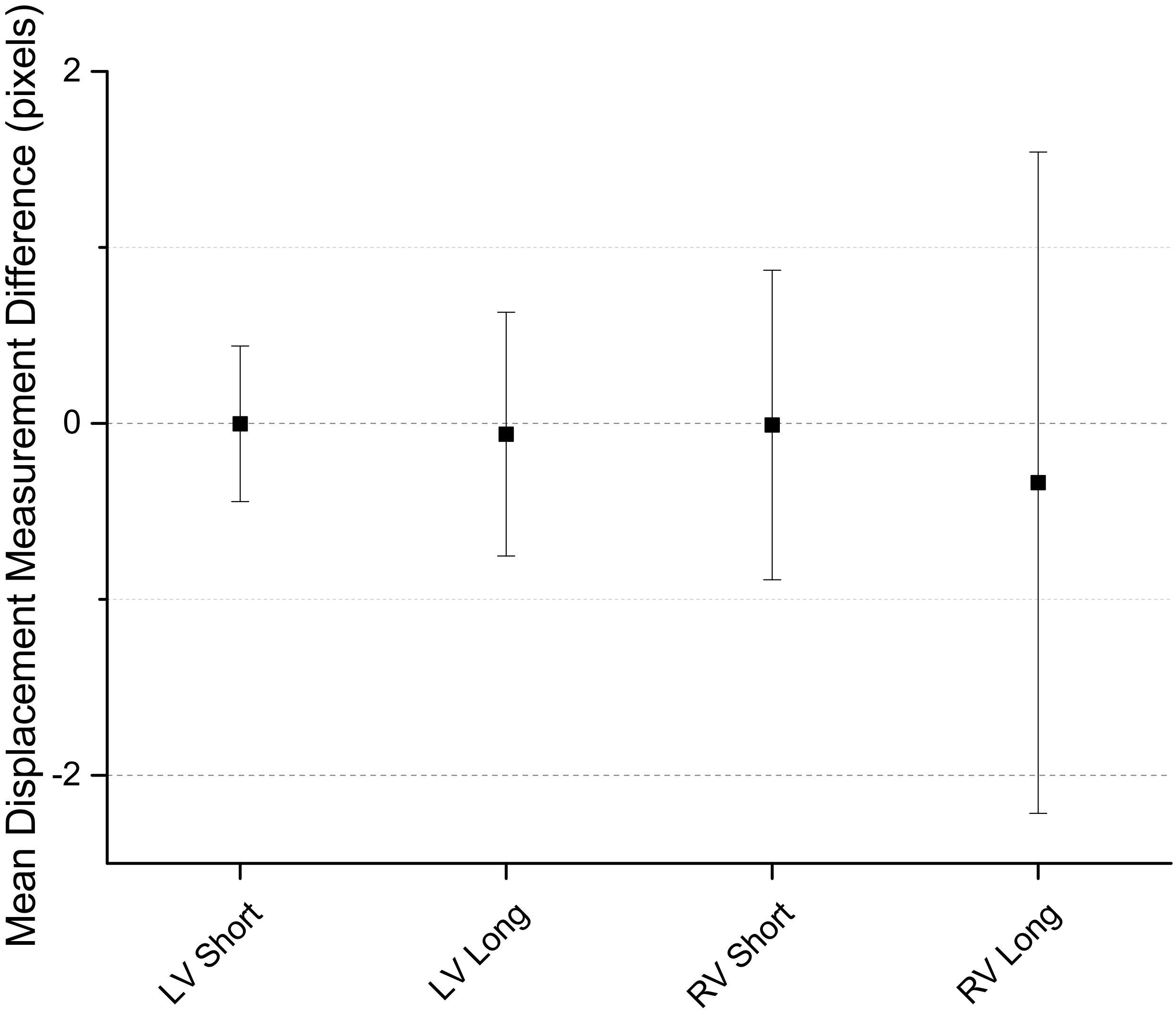

Figure 6.7: Mean displacement measurement differences at ES for LV short-axis, LV long-axis, RV short-axis, and RV long-axis groups from the 30 validation studies. Manually identified tag points were used for comparison. Error bar represents one standard deviation.

Table 6.1: Statistics of differences between end-systolic strains (unitless) and twists (degrees) from the proposed method and FB method for 30 validation studies. Differences = Mean ± Standard Error. ρ = Correlation Coefficient. For all correlation coefficients, $p < 0.001$. CV = Coefficient of Variance. E_{cc} = LV circumferential strain. E_{ll} = LV longitudinal strain. E_{min} = LV minimum principal strain. $E_{\text{tt}}RV$ = RV tangential strain. $E_{\text{ll}}RV$ = RV longitudinal strain. $E_{\text{min}}RV$ = RV minimum principal strain.

Strain	Differences	p	ρ	CV
E_{cc}	0.0047 ± 0.0023	0.52	0.90	2.33%
E_{ll}	0.0037 ± 0.0018	0.68	0.96	1.57%
E_{min}	0.0004 ± 0.0010	0.96	0.99	0.70%
$Twist$	-0.1539 ± 0.0787	0.82	0.99	1.61%
$E_{\text{tt}}RV$	0.0102 ± 0.0044	0.27	0.79	4.66%
$E_{\text{ll}}RV$	0.0125 ± 0.0044	0.18	0.77	4.14%
$E_{\text{min}}RV$	0.0003 ± 0.0019	0.98	0.96	1.32%

in 3D cardiac strains at ES for the first one and 3D+time strain curves for the second. We refer to the first method as the Feature-Based method (FB) and the second as the manual Strain from Unwrapped Phase (mSUP) method.

ES strain parameters from the proposed method were compared to those from the feature-based method (FB) using paired t-tests. The results are shown in Table 6.1. A P-value equal to or less than 0.05 was considered statistically significant. Strains and twists from these two methods were not significantly different. Correlations were quite high except for RV tangential strains and RV longitudinal strains for the reasons described above. The maximum coefficient of variance (CV) of the LV strain parameters was 2.33% and that of the RV strain parameters was 4.66%. The CV for twist was 1.61%.

In Table 6.2 we compared peak strains (twists) and strain rates (twist rates) from the reconstructed strain time curves using the proposed method to those reconstructed using mSUP. Parameters except for systolic twist rates were not significantly different using these two methods. Correlations were high except for $E_{\text{tt}}RV$ and $E_{\text{min}}RV$ strain rates. CV for RV strain rates and twist rates were higher than LV strain rates.

Table 6.2: Comparison of peak strains and strain rates (twists and twist rates) computed using the proposed method and mSUP. Differences = Mean ± Standard Error. ρ = Correlation Coefficient. CV = Coefficient of Variance. E_{cc} = LV circumferential strain. E_{min} = LV minimum principal strain. $E_{\text{tt}}RV$ = RV tangential strain. $E_{\text{min}}RV$ = RV minimum principal strain. Peak = peak strain (unitless) / twist (degrees) during the cycle. Sys Rate = systolic strain rate (sec^{-1}) / twist rate (degrees/sec). E Dia Rate = early diastolic strain rate (sec^{-1}) / twist rate (degrees/sec).

Strain	Differences	p	ρ	p	CV
E_{cc} Peak	-0.0055 ± 0.0003	0.44	0.94	<0.001	1.86%
Sys Rate	0.0023 ± 0.0032	0.96	0.84	<0.001	3.34%
E Dia Rate	0.0274 ± 0.0067	0.67	0.71	<0.001	6.92%
E_{min} Peak	-0.0037 ± 0.0004	0.65	0.93	<0.001	1.55%
Sys Rate	-0.0196 ± 0.0040	0.75	0.87	<0.001	3.42%
E Dia Rate	-0.0502 ± 0.0046	0.38	0.80	<0.001	5.46%
$Twist$ Peak	1.2900 ± 0.0541	0.22	0.96	<0.001	3.37%
Sys Rate	13.5935 ± 0.6530	0.04	0.81	<0.001	8.05%
E Dia Rate	-9.6224 ± 0.5940	0.11	0.71	<0.001	7.90%
$E_{\text{tt}}RV$ Peak	-0.0058 ± 0.0007	0.52	0.85	<0.001	4.02%
Sys Rate	-0.0637 ± 0.0084	0.30	0.44	0.015	8.42%
E Dia Rate	0.0081 ± 0.0102	0.93	0.62	<0.001	9.74%
$E_{\text{min}}RV$ Peak	-0.0095 ± 0.0005	0.29	0.90	<0.001	1.94%
Sys Rate	-0.1211 ± 0.0092	0.10	0.53	0.003	7.40%
E Dia Rate	-0.0631 ± 0.0094	0.35	0.43	0.019	10.76%

Figure 6.8 shows the minimum principal strain at end-systole for a representative from each of the subject groups (normal volunteers (NL), diabetic patients with myocardial infarction (DMI), resistant hypertensive patients (HTN), and patients with pulmonary arterial hypertension (PAH)) using the FB, mSUP and the proposed method. Qualitatively, the strain maps from all three methods are similar.

Minimum principal strains averaged over each subject group using the proposed method, mSUP and 2D HARP strain [86], are shown in Figure 6.9. Because different subjects have different heart rates, the strain curves were normalized in time by dividing the QRS delay time of each time point by the systolic interval in that subject and multiplying the result by 100%. This resulted strains versus % systolic interval, which were averaged and plotted in Figure 6.9. PCGC strain curves were similar to those from the mSUP method and were smoother. Because the HARP algorithm computes 2D Eulerian strain, there were some differences between the strain curves from HARP strain and those from mSUP or the PCGC. As expected, strain magnitudes from all three methods were lower in the DMI and PAH groups than in NL and HTN.

6.4 Discussion and Conclusion

The motion reconstruction accuracy from tagged MR images largely depends on the performance of the tag point extraction method. In our work, we used a bank of Gabor filters to detect the tag points, which adjust parameters to fit to the local tag features, and potentially perform better than the bandpass filter with fixed window. However, the tag points were detected pixel-wise. Tag detection accuracy could potentially be improved by spatially smoothing the tag points in a given tag line.

We used a graph cuts-based method for tag point classification (PCGC), which assumes the 1D displacement field is spatially smooth. For computing the neighborhood of the tag point and the membership weight, we used the local frequency map which is a byproduct

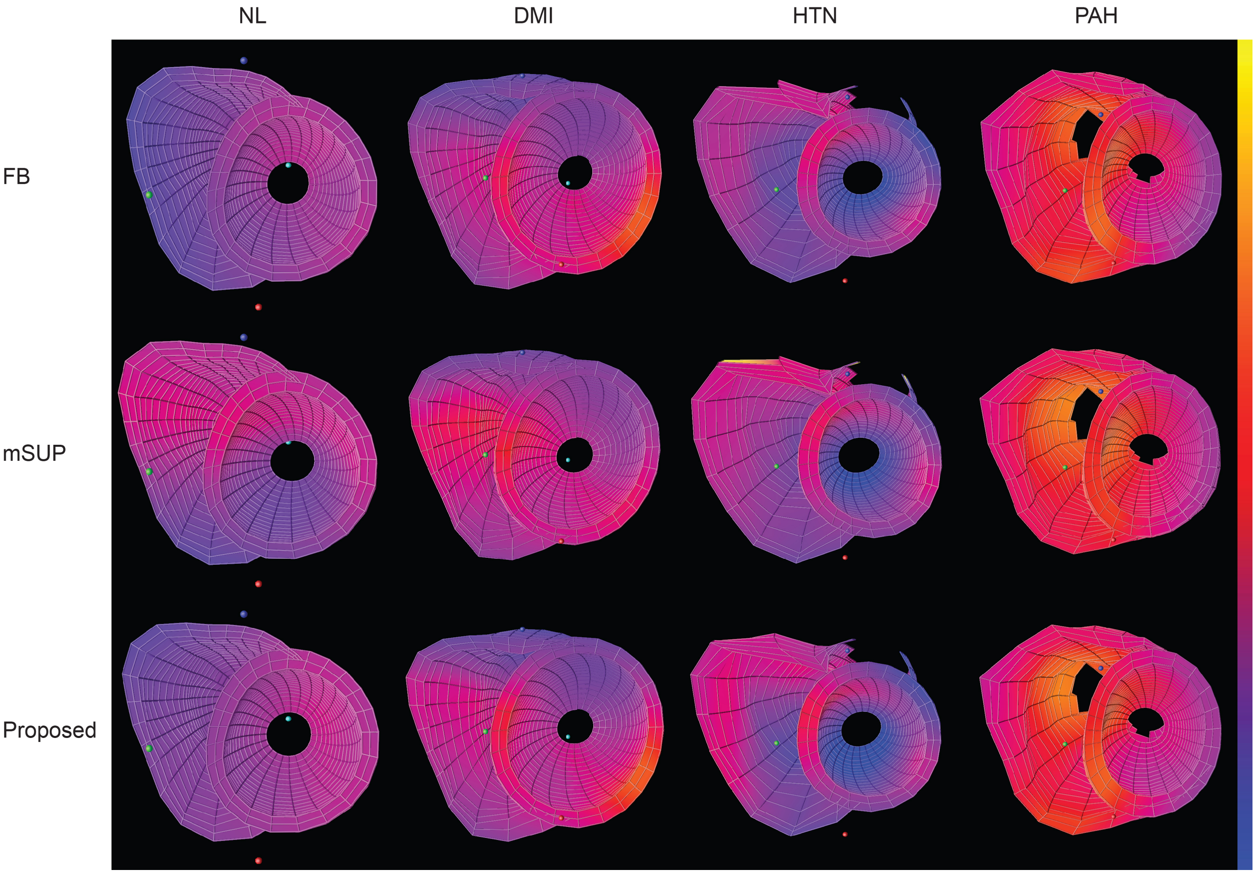

Figure 6.8: Representative end-systolic minimum principal strains ($E_{\min}$ and $E_{\min}RV$) computed using (top to bottom) FB, mSUP and the proposed method for (left to right) a normal volunteer (NL), and patients with myocardial infarction and diabetes (DMI), resistant hypertension (HTN), and pulmonary arterial hypertension (PAH). Strain ranges from blue (25% contraction) to yellow (no change).

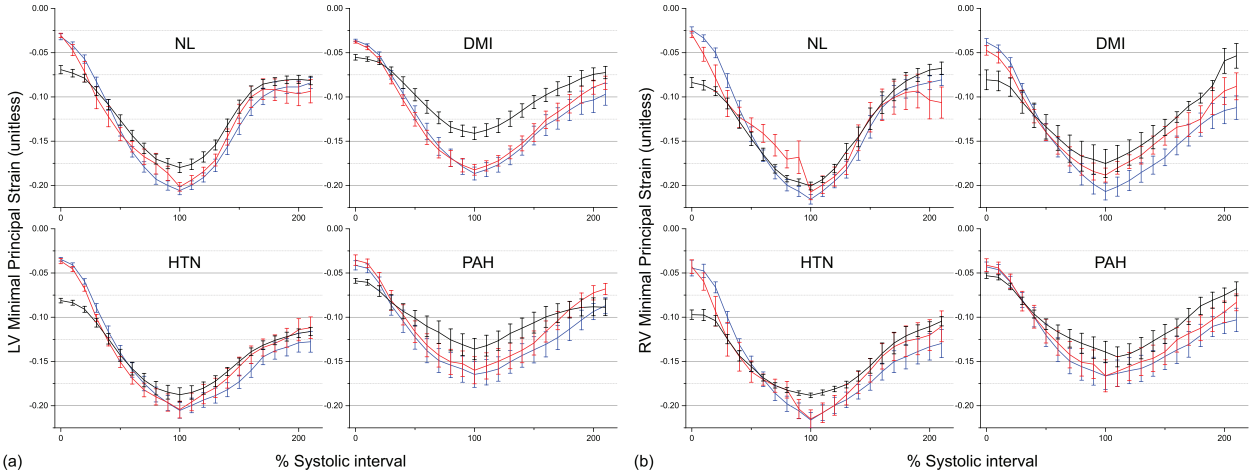

Figure 6.9: (a) LV minimum principal strains ($E_{\min}$) and (b) RV minimum principal strains ($E_{\min}RV$) with the proposed method (blue), mSUP (red) and HARP strain technique (black) averaged over 10 normal volunteers (NL), 5 diabetic patients with myocardial infarction (DMI), 8 resistant hypertensive patients (HTN), and 7 patients with pulmonary arterial hypertension (PAH). Strains were plotted against the percentage of the systolic cycle. Error bar represents one standard error.

from the Gabor filter bank, and a Gaussian type radial basis function. Other types of neighborhood functions could potentially be used.

One modification we made for the PCGC is that we generated auxiliary points to improve the classification accuracy. The phase shifted map was used with half a cycle difference. Theoretically, we can generate any times dense auxiliary points by changing the shifted phase. For example, shifting the phase map with $2\pi/3$ and $4\pi/3$ will generate auxiliary points at one-third and two-third positions between neighboring tag lines, thus giving a two times denser point set. However, more auxiliary points will increase computation time of the PCGC algorithm.

We used the discrete model-free method for motion compensation. However, there are more options that can be adopted, such as non-rigid registration, which aligns two images by warping one with parametric transformation. One of the future research topics is an investigation of other motion compensation techniques.

In this chapter, we presented a method for cardiac motion and strain analysis using tagged MR images. We used Gabor filter banks for tag point extraction, and a graph cuts-based algorithm to classify each of the detected tag points for displacement measurement. We also introduced a motion compensation technique with the discrete model-free method to improve the classification accuracy. A typical cardiac imaging study with 10 short-axis slices and 6 long-axis slices required 30 minutes for contouring followed by 44 minutes of automated processing. With a set of *in-vivo* data we also validated the proposed method by comparing strains to those from a feature-based method with manually specified tag points, and a manual unwrapped phase-based method.

Chapter 7

MOTION MEASUREMENT AND STRAIN ANALYSIS OF EXTRAOCULAR MUSCLES WITH TAGGED MR IMAGING

7.1 Introduction

The extraocular muscles have the function to control the motion of the eye globe. Different parts of the extraocular muscles (four rectus muscles and two oblique muscles) cooperate under the neural inputs and mechanical constraints to conduct the correct motion. This coordination sometimes is impaired due to diseases or anomalies known as eye motion disorders. One of the most common disorders is strabismus, a condition in which a lack of binocular coordination among the extraocular muscles prevents the eye from gazing at the same point. The mechanism of the extraocular muscles is under active research but a solid and comprehensive theory has not yet been published.

There have been several models proposed in order to explain the cooperative behavior of the extraocular muscles [81]. In [82, 103], the authors questioned the classic model because if the rectus extraocular muscles were constrained only at their ends, the muscles would sideslip widely about the globe, making eye rotations uncontrollable. These observations gave rise to a passive pulley model in [80] that described the motion of the rectus muscles as a constraint one that was stabilized with the help of a sheath, which functioned like a pulley. In [35], an active pulley theory was proposed, in which the pulley was considered to be active and connected to the orbital layer such that the pulley could move longitudinally.

Recently, tagged MRI has been applied to better understand the mechanism of the extraocular muscles [92, 93]. The relative motion of the soft tissue pulleys with respect to the orbit, globe and extraocular muscles can potentially be identified with this imaging technique. In this chapter, we conducted tagged MRI scans for human subjects under horizontal saccadic, horizontal smooth pursuit, and asymmetric convergence saccadic eye motions. These tagged studies were further analyzed by computing strain maps for the orbital and global components of the right lateral rectus (RLR) muscle, with the hope to better understand the function of the rectus muscle layers.

7.2 Methods and Experiments

7.2.1 Material Preparation

Six normal volunteers were imaged in a Magnetom 7 Tesla scanner (Siemens Healthcare, Erlangen, Germany) while undergoing the eye motions of horizontal saccades, horizontal smooth pursuit, and asymmetric convergence saccades induced from gazing at a moving target projected on the screen. Saccadic eye motions were generated by displaying a white cross on a black background that alternated between two positions with an amplitude of $\pm 6.8^{\circ}$ and a period of 2256ms. Smooth pursuit motion was generated by displaying the target with a sinusoidal motion from left to right with an amplitude of $\pm 6.8^{\circ}$ and a period of 2000ms. For asymmetric convergence, the cross was displayed on a screen 106cm away from the right eye and alternated with an LED placed 10cm away from the eye. There is a random delay of $150 - 250$ms between the target change and the start of a saccadic movement, and this delay is different for each scan [67]. consequently, the saccadic eye movements were timed to allow for acquisition of an initial, single undeformed time frame before the movement, a period of 2-3 time frames that were unusable due to the random delay and movement, and series of time frames where the eye was stable after the movement in the contracted state. Each display sequence began with a trigger to the MRI scanner to display tags and begin acquisition. For saccades, the target stayed in position 1 for 119ms to allow acquisition of an undeformed tagged image. The target then moved to position 2 for 1484ms and back to position 1 for 653ms. Tagged images were acquired continuously for 1603ms after the scanner was triggered. Figure 7.1 shows the timing of the saccadic scan.

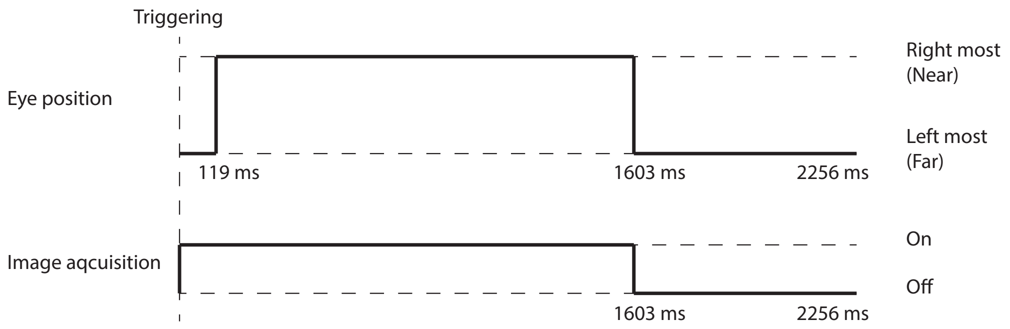

Figure 7.1: Display sequence induced eye motion and image acquisition for saccadic scans.

7.2.2 Proton Density Weighted Protocol

An MPRAGE anatomical scan was acquired first with no eye motion for subsequent motion slice planning. Tagged image planes were approximately transverse, but were slightly oblique to align the planes parallel to the RLR muscle and with the rotation plane of the eye globe. Tagged images were acquired in a double-oblique transverse plane with a standard cardiac, prospectively gated, gradient-echo sequence using a 32-channel head coil (Nova Medical, Boston, Massachusetts). Two tagged acquisitions with spacing of 4mm were performed for each motion with tags oriented perpendicular to the RLR in one acquisition and parallel to the RLR in the other. Scanning parameters were $0.44 \times 0.44\text{mm}^2$ in plane resolution, 1.5mm slice thickness, TR/TE=8.4ms/4.0ms, flip angle=10°, 302 Hz/pixel. For saccadic motions, 14 segments were acquired per phase for a temporal resolution of 119ms. For smooth pursuit, 7 segments were acquired per phase for a temporal resolution of 59ms.

7.2.3 Image Analysis and Strain Computation

The contours for the orbital and global layers of the RLR muscle were manually drawn at the first time frame and the time frame either when the eye movement is stabilized (saccades) or when the muscle deformation is maximized (smooth pursuit). Then tag points were manually identified and drawn along the tag line within the segmented masks. These manual tag points were used to calculate the 1D displacement measurements of the tag

Table 7.1: Comparison of medial normal and shear strains (unitless) for global and orbital layers of the right lateral rectus muscle under movements of horizontal saccades, horizontal smooth pursuit, and asymmetric convergence saccades.

Strain		Global Layer	Orbital Layer	p
Horizontal Saccades	Normal	-0.089 ± 0.012	-0.099 ± 0.007	0.40
	Shear	-0.006 ± 0.002	0.030 ± 0.006	0.01
Horizontal Smooth Pursuit	Normal	-0.092 ± 0.005	-0.081 ± 0.006	0.22
	Shear	-0.003 ± 0.001	0.016 ± 0.002	0.00
Asymmetric Convergence Saccades	normal	-0.025 ± 0.009	-0.023 ± 0.008	0.39
	Shear	-0.000 ± 0.001	0.000 ± 0.001	0.41

lines. Then the 2D discrete model-free method [40] introduced in Chapter 6 was used to interpolate a dense 2D motion field from the sparse displacement measurements based on a spatial smoothness assumption. 2D normal strains (E_{xx}) along the longitudinal orientation of the muscle and shear strains (E_{xy}) were computed under the Cartesian coordinate for both the orbital and the global layers. Strains averaged over the medial third were used for comparison between the two layers.

7.3 Results

Normal strains and shear strains under each of the three eye movements have been computed for all six human studies. Figure 7.2 shows the normal strain and shear strain maps under the horizontal saccadic movement for one of the subjects. For each type of the eye movement, normal strains and shear strains were averaged over the medial third of the orbital and global layers for all six subjects. Then the strain values were compared between the two layers with t-tests. Table 7.1 shows the comparison results. Significant differences of the shear strains were found in the orbital and the global layers of the RLR muscle with both horizontal saccadic and smooth pursuit movements. But no significant differences were found for the normal strains. For asymmetric convergence saccadic movement, no significant differences were found either for the normal or the shear strain in the two layers.

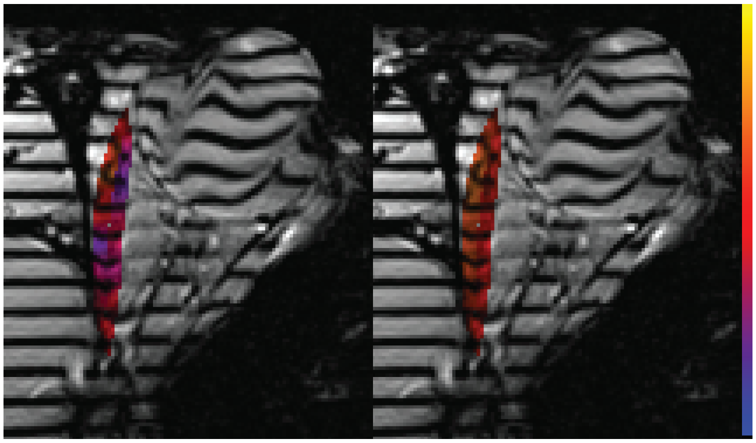

Figure 7.2: Representative normal strain (left) and shear strain (right) maps for the orbital and global layers of the right lateral rectus muscle. The normal strain ranges from -20% (blue) to 20% (yellow) and the shear strain ranges from -15% (blue) to 15% (yellow).

7.4 Discussion and Conclusion

In this chapter, we used tagged MRI with high resolution to image the deformation pattern of the right lateral rectus muscle during three kinds of eye movements: horizontal saccades, horizontal smooth pursuit, and asymmetric convergence saccades. Based on our results, the orbital and the global layers of the right lateral rectus muscle showed different strain patterns with horizontal but not asymmetric convergence movement, which suggest that these two layers move relatively independently of each other. Even though the detailed mechanism of the extraocular muscle during eye motion is still unknown, our method may contribute to a better understanding of the pulley structure of the extraocular muscle.

Chapter 8

VITREOUS HUMOUR MOTION AND STRAIN ANALYSIS WITH TAGGED MR IMAGING

8.1 Introduction

The vitreous humour is a transparent viscoelastic fluid that fills in between the lens and the retina in the eyeball. Besides the optical function it supports, this fluid has complex mechanical property due to the presence of a network of collagen fibrils and polyanionic hyaluronan macromolecules of high molecular weight [21]. The rheological property of the vitreous humour is directly related to the motion pattern and the shear stress induced by the vitreous motion. Measurement of the rheological properties of the vitreous humour has only been conducted *ex-vivo* and the values can differ from the true ones due to mass loss and microstructural changes after dissection [84, 117].

It is believed that the tension exerted on the retina plays an important role in the development of retinal detachment. One common type of the detachment is rhematogenous retinal detachment, which occurs when a tear forms in the retina and the liquefied vitreous fills in the space, preventing the retina from functioning normally. Many of the rhematogenous retinal detachment happened to older people, whose vitreous humor is less viscous compared to younger group and has significantly different mechanical properties [112, 123]. Therefore, examining the relationship between shear stress and the mechanical properties of the vitreous humour is helpful for a better understanding of the process of the retinal detachment development.

Many studies have been conducted using mathematical models of vitreous humour motion under eye rotations to evaluate the shear stresses exerted on the retina and their relationship to the mechanical properties of the vitreous. [24] studied the linearized behavior of a viscoelastic fluid in a sphere performing periodic and impulsive rotations. [34] used a similar model to analyze the motion behavior of vitreous humour and the peripheral shear stress. However, these analytical models all assumed the vitreous cavity to be of a spherical shape, while actually the true shape should be like an ellipsoid with an indentation at the lens. As indicated by [4, 102], a deformation on the spherical shape of the vitreous cavity affects the flow pattern significantly. On the other hand, [66] showed that the vitreous humour was inhomogeneous across the space and had spatially dependent rheological properties.

Compared to mathematical models developed for analyzing motion pattern of the vitreous humour under forced rotations, *in-vivo* experiments are limited. [138] measured the relaxation pattern of the vitreous humour after impulsive eye rotation by using a light source. [123] used ultrasound to track the speckles of the vitreous humour under impulsive rotations. However, these measurements were limited as the inhomogeneity of the vitreous humour was not considered and only bulk movements were recorded. To better measure the regional deformation within the vitreous, [91] used tagged MRI to non-invasively scan the vitreous equatorial plane and encode the vitreous deformation. A phase-based tracking method was then used to track the local deformation at each concentric circle mesh point. [91] estimated viscoelastic parameters by fitting an analytical model [34] to the experiment result. The difference between the observed complex deformation and reported *ex-vivo* measurements was evident.

In this chapter we also used tagged MRI images to obtain the motion pattern of the vitreous humour. Besides estimating the viscoelastic properties and comparing the vitreous deformation to the analytical result, we also conducted the strain analysis directly from the tagged images, revealing the regional shear strain pattern of the vitreous. In this way, we do not need to assume the geometry and the homogeneity of the vitreous humour. We also compared the experimental strain results to those from the analytical model by [34] with the hope to improve the understanding of the effect of vitreous mechanical properties on the deformation pattern *in-vivo*, as well as its relationship to the development of retinal detachment.

8.2 Method and Experiment

8.2.1 Analytical Model of Deformation and Strain

By assuming the vitreous cavity is spherical and the vitreous humour is a spatially homogeneous viscoelastic fluid, [34] provided a time-dependent analytical solution to the vitreous humour deformation under a periodic sinusoidal left-right movement of the eye globe. In this model, the circumferential velocity in radial coordinate has the form

$$V_\phi = U\Im\left[f(R)e^{iT}\right]\sin\theta, \tag{8.1}$$

where U is the maximum circumferential velocity at the eye wall during periodic rotation, $R \in [0,1]$ is the normalized radius, $T = \omega t$ is the non-dimensional time with rotation frequency ω and time t, and θ is the polar angle. Since we only investigate motion pattern on the equatorial plane, the $\sin\theta$ term can be omitted. $\Im[\cdot]$ indicates taking the imaginary part. The solution to $f(R)$ is given as

$$\begin{aligned} f(z) &= \frac{F(z)}{F(i^{1/2}\alpha)} \\ F(z) &= -\frac{\sinh(z)}{z^2} + \frac{\cosh(z)}{z}, \end{aligned} \tag{8.2}$$

where $z = i^{1/2}\alpha R$ and $\alpha = R_0\sqrt{\omega/v^\star}$. R_0 is the radius of the eye and $v^\star$ is the complex kinematic viscosity, defined as $v^\star = v' - iv''$, with v' denoting the viscosity and v'' the elasticity. By using a modified Womersley number a, defined as $a = R_0\sqrt{\omega/|v^\star|}$, and a phase angle b, defined as $b = \tan^{-1}(-v'/v'')$, we can reformulate the equation with $i^{1/2}\alpha = ae^{ib/2}$ and $z = ae^{ib/2}R$ and get

$$f(R) = F(ae^{ib/2}R)/F(ae^{ib/2}). \tag{8.3}$$

With the solution to the circumferential velocity, we can derive the circumferential deformation as

$$\begin{aligned} d_\phi(R,T) &= \int_0^T U\mathfrak{I}\left[f(R)e^{iT}\right] dt \\ &= U\mathfrak{R}\left[f(R)\right](1-\cos T) + U\mathfrak{I}\left[f(R)\right]\sin T. \end{aligned} \tag{8.4}$$

$\mathfrak{R}\left[f(R)\right]$ and $\mathfrak{I}\left[f(R)\right]$ are real and imaginary parts of $f(R)$, respectively. Following this we can derive the equation for shear strain in the polar coordinate system

$$e_{r\phi}(R,T) = \frac{1}{2}\left(\frac{\partial d_\phi(R,T)}{\partial R} - \frac{d_\phi(R,T)}{R}\right). \tag{8.5}$$

Figure 8.1(a) shows the plot of rotation angles as functions of time at discrete radial positions by using the above analytical model. The modified Womersley number and the phase angle used are $a = 4.3$ and $b = 1.67$. The maximum angular velocity is $5^\circ/s$ and the angular frequency is $\omega = \pi$. Note that the range of phase angle should be $b \in [\pi/2, \pi]$ in order to make sure that the kinematic viscosity v' and v'' are both non-negative, as $\cos(b) = -v''/|v^\star|$ and $\sin(b) = v'/|v^\star|$. The phase angle mentioned in this research is not the same as that mentioned in [66], which was reported to be -1.47 in the anterior part. Nevertheless, $b = \pi + (-1.47) \approx 1.67$ and $b = -1.47$ provide the same tangential value as a result of periodicity.

Figure 8.1(b) shows the plot of shear strain at discrete radial positions and times using the same parameters. From this analytical result we can see that the peak shear strain occurred at the eye wall but not at the time when peak rotation happens.

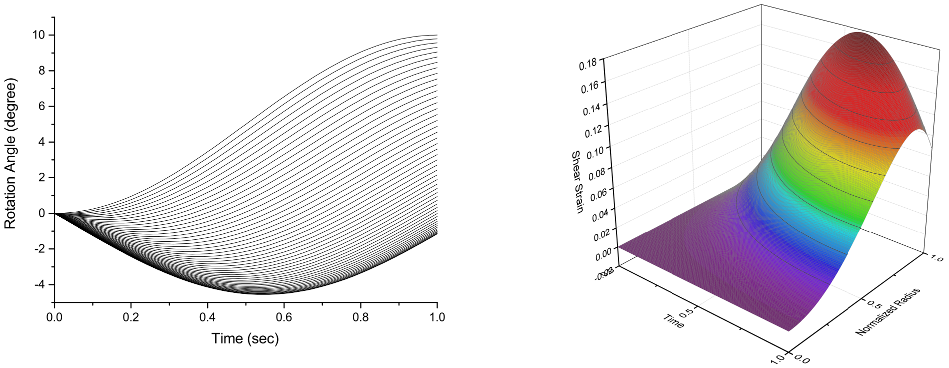

(a) Rotation angle changing with time and radius

(b) Shear strain changing with time and radius

Figure 8.1: Rotation angle and shear strain from the analytical model with $a = 4.3$, $b = 1.67$, $\omega = \pi$ and maximum angular velocity of $5^\circ/s$ at different time and radial locations.

8.2.2 Materials and Experiments

5 subjects with the age ranging from 20 to 54 undertook the MRI scan. While scanning was on, all subjects were asked to look at the horizontal moving square projected on the screen, with an induced 10° left to right sinusoidal movement of the eye globe. The oscillation period was 2 second and the first half of the cycle was imaged, recording the eye rotating from the left most position to the right most position.

The lens center and the scleral insertion of the optic nerve defined the imaging plane. Two scans were performed with a prospectively ECG gated fast gradient-echo cine sequence on a Magnetom 7 Tesla MRI scanner (Siemens Healthcare, Erlangen, Germany) using a 32-channel head coil (Nova Medical, Boston, Massachusetts). One has horizontal tags and the other one has vertical tags, all spaced 4mm apart. 16 frames of images were acquired for each scan, with a temporal resolution of 60ms.

The motion estimation method with PCGC algorithm in Chapter 6 developed for cardiac tagged MRI analysis was adopted. Gabor filter banks were used to get the angle map from the tagged images. Then tag points were detected by extracting the edge information from the angle map. Since the detected tag points had only pixel-wise accuracy, their positions were further refined by using an active contour-based algorithm in [39], followed by the manual inspection and modification, if necessary. After classification of the detected tag points, a 2D version of the discrete model-free method [40] was then used to interpolate and estimate the deformation at each pixel in the region of interest.

To quantify the rotational deformation at each radial position, we utilized a mesh approach mentioned in [91] with the 36 × 60 mesh points generated evenly along radial and polar directions within the vitreous region. Rotational deformation at each of the 60 point locations from one of the 36 concentric circles was estimated using the dense deformation field. Averaging all these values provided the estimation of the rotation at that specific radial position. Minimizing the squared difference between the observed rotation deformation and that from the analytical model over a and b gave the estimation of these two viscoelastic parameters. The search for a and b was restricted as $a \in [3, 8]$ with a step size of 0.05 and $b \in [1.6, 3.1]$ with a step size of 0.02. In this research, deformations of the three innermost and three outermost concentric layers were dropped out to avoid bad fitting result. Deformations from the innermost layers were not reliable because the measurements were sensitive to the choice of the rotation center, which was defined manually. The outermost layers may overlap with the sclera section and therefore should also be avoided.

With the dense deformation field we were also able to reconstruct the 2D strain in Cartesian coordinate, and then to convert this strain to polar coordinate system. Let E be the strain tensor in Cartesian coordinate and S the strain tensor in polar coordinate, the conversion from E to S is provided as

$$S = \begin{bmatrix} s_{rr} & s_{r\phi} \\ s_{\phi r} & s_{\phi\phi} \end{bmatrix} = \begin{bmatrix} \cos\phi & \sin\phi \\ -\sin\phi & \cos\phi \end{bmatrix} \begin{bmatrix} e_{xx} & e_{xy} \\ e_{yx} & e_{yy} \end{bmatrix} \begin{bmatrix} \cos\phi & -\sin\phi \\ \sin\phi & \cos\phi \end{bmatrix} = RER^T.$$

The shear strain $s_{r\phi}$ is directly related to the shear stress by a complex shear modulus $G = G' + iG'' = \rho\omega(v'' + iv')$, where ρ is the density, ω is the frequency of oscillation, v' and v'' are kinematic viscosity and elasticity, respectively. If the viscoelastic property is

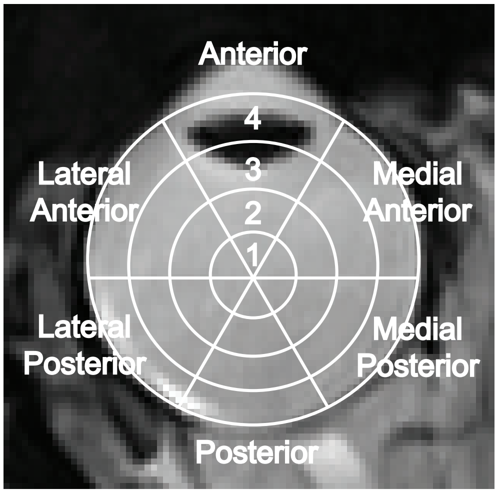

Figure 8.2: Vitreous separated into 4 × 6 segments. Each layer labeled with a number from 1 to 4 is divided into 6 regions: anterior, medial anterior, medial posterior, posterior, lateral posterior, and lateral anterior.

homogeneous across the vitreous cavity, the shear strain will differ from the shear stress by only a magnitude and a phase delay and the peak shear strain location shall coincide with that of the peak shear stress, which is supposedly at the eye wall, as shown in Figure 8.1(b). Though the shear stress cannot be readily evaluated *in-vivo*, we can take the advantage of the computed shear strain from this experiment.

In order to quantify the shear strains at different regions of the vitreous and to compare them against the analytical results, we divided the vitreous region into 24 segments as shown in Figure 8.2. After manually setting up the landmarks for the rotation center and the lens front, the circular region of vitreous was radially divided into 4 layers of ring, with each layer segmented into 6 compartments: anterior, medial anterior, medial posterior, posterior, lateral posterior and lateral anterior regions. Shear strain was estimated within each of the 24 regions such that the comparison between the experimental result and the analytical solution could be conducted.

8.3 Results

For all subjects, tag points were tracked at each time frame and the dense deformation fields were also computed based on these deformed tag points. Figure 8.3 shows the tracked tag points overlaid on the tagged images, the dense deformation fields and shear strains for a subject with the age of 23 and the other one with the age of 46 when subjects' eyes rotated to the right most position, corresponding to the non-dimensional time $T = \pi$. We can tell a qualitatively significant difference between the two deformation patterns from the deformed tag lines of the left two column images in Figure 8.3: the first subject's vitreous humour deformed more rigidly, indicating a potential higher viscoelastic property; while the second subject's vitreous humour has larger deformation and shearing near the outermost layer of the vitreous, suggesting less viscoelasticity (or more liquefaction). The dense deformation fields in the middle right column show the difference more clearly. For the second subject, we can see that most of the large deformation concentrated near the boundary of the vitreous. Also we notice an obvious vortex of motion right behind the lens position which cannot be seen in the deformation field of the first subject. We attribute this phenomenon to a larger modified Womersley number and the effect of the vitreous cavity geometry (indentation at the lens) [116]. Besides the motion fields, the shear strains came up with different patterns too. We can see at this specific time ($T = \pi$), peak shear strain position for the first subject is more inward and the peak strain values is lower than that from the second subject. We will evaluate and discuss the shear strain in a more systematic way in the later part of this section.

Figure 8.4 shows the plot of rotation angles as functions of time for the middle 30 concentric circles of the mesh. Figure 8.4(a) and (b) are experimental result and analytical fitting result for the same subject in Figure 8.3(a). Figure 8.4(c) and (d) are experimental result and analytical fitting result for the subject in Figure 8.3(b). We noticed some discrepancies between the observed rotation angle and the fitting result, especially for concentric circles near the center. This was partly due to the motion complexity induced either by

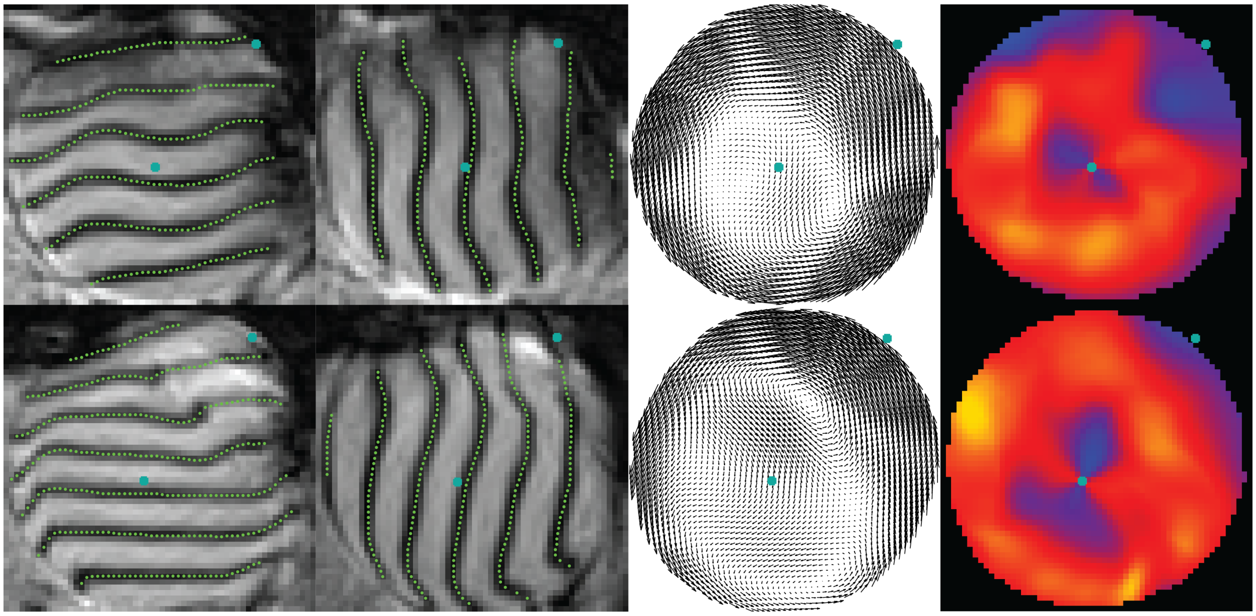

Figure 8.3: Tracked tag points of horizontal orientation (left column) and vertical orientation (middle left column), dense deformation fields (middle right column) and shear strains (right column) for a 23 years old subject (top row) and a 46 years old subject (bottom row) when subjects' eyes rotated to the right most position. Cyan dots near centroid are the rotation centers used to compute shear strains, and dots near boundary denote the center the cornea.

the nonuniform vitreous cavity shape or the inhomogeneous viscoelasticity. The choice of the rotation center also influenced the computed rotation near the center. Despite these discrepancies the analytical fitting results conform to the experimental results globally.

By repeating this fitting procedure to all the 5 subjects, we estimated the modified Womersley number, the phase angle, kinematic viscosity and elasticity for these subjects, as listed in Table 8.1. Subjects shown before in Figure 8.3 and Figure 8.4 are subject 2 and subject 4 in Table 8.1. We expected to see an increasing of the modified Womersley number and a decreasing of the viscosity with the age as a result of liquefaction. However, the correlation between a and age is 0.34 and the correlation between v' and age is -0.51, both not significant. More samples from more subjects need to be acquired in order to draw a conclusion.

Figure 8.5 shows two representative regional shear strains $s_{r\phi}$ against time for the two subjects in Figure 8.3. Each column in the figure represents the shear strains in six regions

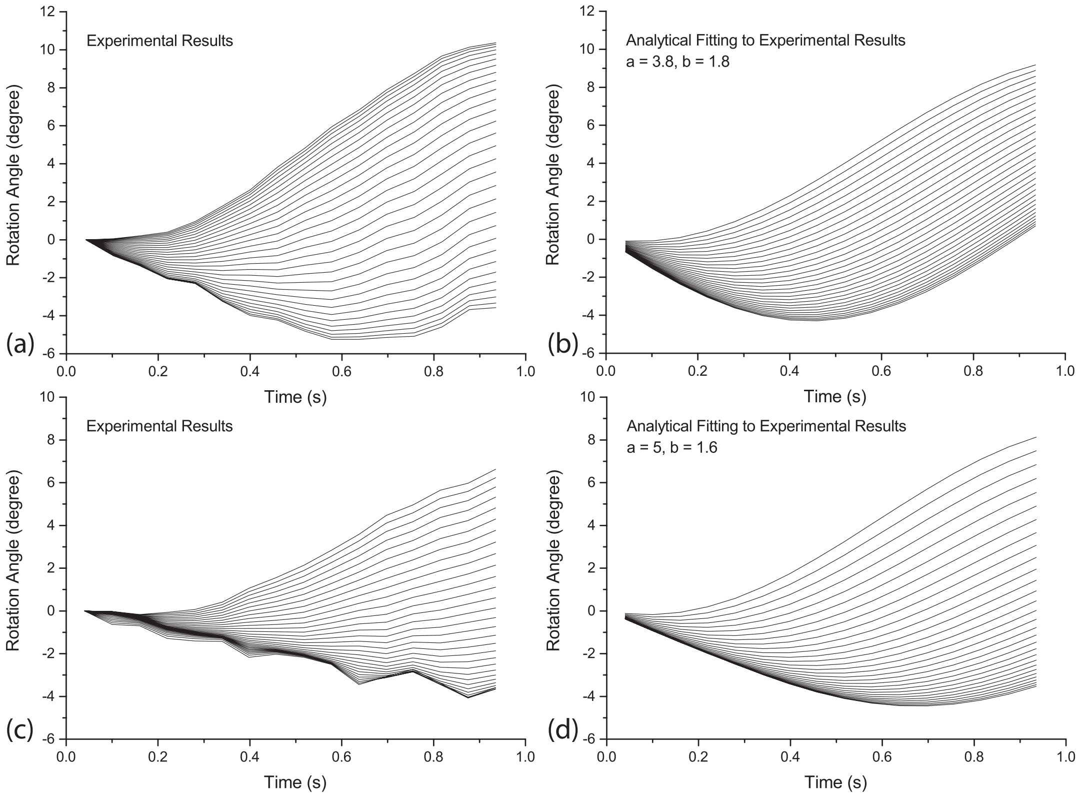

Figure 8.4: (a) Rotation angles as functions of time for the middle 30 concentric circles of the mesh for the same subject in Figure 8.3(a). (b) The analytical fitting to the experimental result in (a). a = 3.8, b = 1.8. (c) Rotation angle for the same subject in Figure 8.3(b). (d) The analytical fitting to the experimental result in (c). a = 5, b = 1.6.

Table 8.1: Fitting results of the modified Womersley number a, the phase angle b, the kinematic viscosity v' and the kinematic elasticity v'' for 5 subjects.

	a(unitless)	b(rad)	$v'(10^{-5}\mathrm{m}^2/\mathrm{s})$	$v''(10^{-6}\mathrm{m}^2/\mathrm{s})$	age
subject 1	4.50	1.66	2.29	2.05	20
subject 2	3.80	1.80	2.89	6.74	23
subject 3	4.65	1.60	2.27	0.66	29
subject 4	5.00	1.60	1.93	0.56	46
subject 5	4.30	1.86	2.31	6.87	54

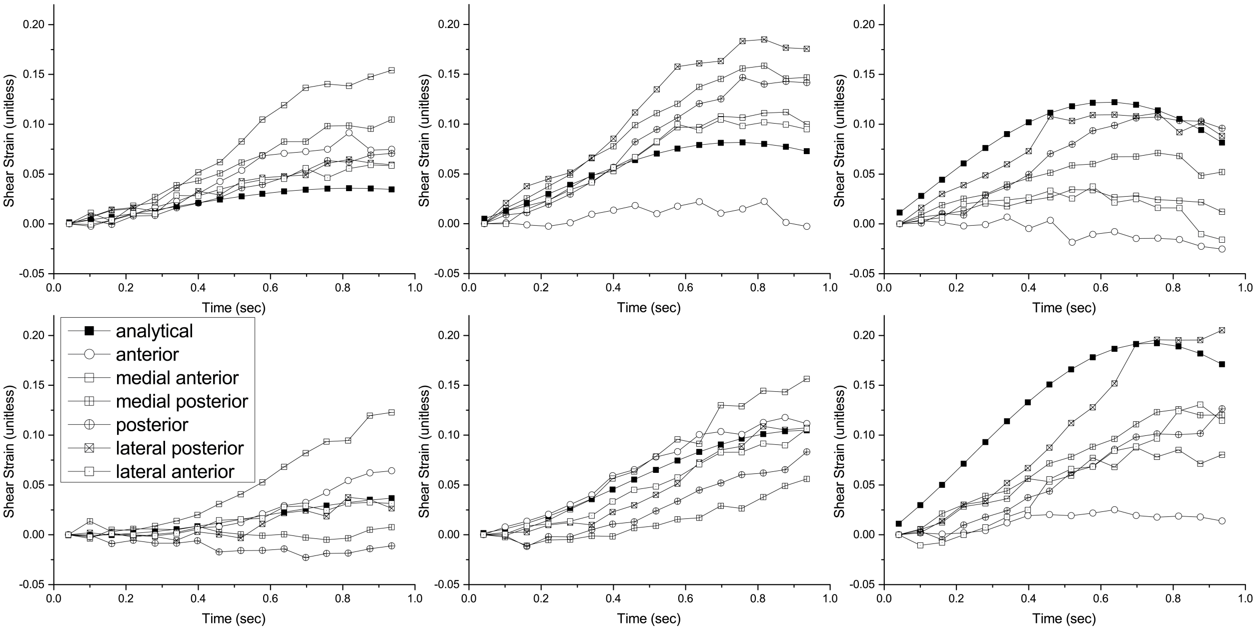

Figure 8.5: Shear strain plot against time for each of the six region at layer 2 (left column), layer 3 (middle column), and layer 4 (right column) for the 23 years old subject (top) and the 46 years old subject (bottom). Shear strains from the analytical model are shown with black square symbol.

(anterior, medial anterior, medial posterior, posterior, lateral posterior, and lateral anterior) at a certain layer as defined in Figure 8.2. The first layer of the core region was not shown in this figure, as the averaging of the shear strain over such a small region is very sensitive to the deformation inhomogeneity and the choice of the rotation center. We expect to observe a higher accordance with the analytical results at the layer 2, 3, and 4. The analytical models were decided from fitting results of the viscoelastic properties (Table 8.1).

From the plot we can see, the shear strain differs from region to region in the same layer. Posterior, medial posterior and lateral posterior regions have the peak shear strain at layer 3 or 4, while anterior, medial anterior and lateral anterior regions have the peak shear strain at layer 2 or 3. This was due to the indentation of the vitreous cavity near the lens, which creates a vortex of vitreous humour deformation behind the lens, as shown in the dense deformation field in Figure 8.3.

Another finding is that, when the modified Womersley a increases, the peak strain value at layer 4 increases, while the peak strain value at layer 2 and 3 decreases. It is also noticed that for small modified Womersley number ($a = 3.8$), the peak strain value at layer 3 is higher than that at layer 4. But for large modified Womersley number ($a = 5$), the peak strain value at layer 4 is higher than that at layer 3. This phenomenon suggests that when the modified Womersley number increases, the peak strain location tends to be more outward, approaching the periphery of the vitreous, and vice versa. Considering that this trend is more obvious with the experimental result than with the analytical model, the vitreous humour near the retina of a subject with small modified Womersley number seems to have a relatively higher viscoelasticity than the other regions of the vitreous. With the process of aging and liquefaction of the vitreous humour, the vitreous humour layer near the retina undergoes certain degeneration and the mechanical property changes significantly.

Besides the comparison to the analytical shear strains, we also computed the correlation between each regional shear strain and age. Because the regional shear strain computation does not require the assumption of the vitreous cavity geometry or the mechanical property of the vitreous humour, we could skip the viscoelastic parameter fitting step and analyze the relationship between regional shear strains and the age directly. Peak shear strain in the medial anterior sector at layer 2 was correlated with the age (-0.92, p=0.027). All other parameters and sectors including viscosity parameters calculated from the analytical model were not significantly correlated. Therefore there is a need to include more human subjects in the experiment in order to improve the confidence of the correlations.

8.4 Conclusion and Discussion

In this chapter we quantified the vitreous humour deformation and estimated its viscoelastic property by fitting the observed deformation to that from the analytical model. For the first time, as far as we know, the detailed shear strain pattern within the vitreous under a forced sinusoidal rotation of the eye was acquired non-invasively, and the computation of the regional shear strain is not affected by the hypothesis of the vitreous geometry and property as what was made by the analytical model. Both the deformation field and the shear strain differ from the analytical solution somehow, suggesting that the vitreous humour is a spatially inhomogeneous viscoelastic fluid, and that the true vitreous cavity geometry (indented at the lens) has an effect on the vitreous flow. With a smaller modified Womersley number, the peak shear strain is more likely to happen at the location further from the vitreous boundary, i.e., the retina.

Although the shear stress could not be evaluated in this work, the shear strain is directly related to the shear stress by a complex modulus. As we have seen from the experiment, with an increasing modified Womersley number, the peak strain gets higher and is more likely to happen near the vitreous boundary. This may indicate that for patient with highly liquefied vitreous, especially for patients with high age, retinal detachment is more likely to happen due to a larger shearing force near the retina.

Chapter 9

CONCLUSION AND FUTURE WORK

9.1 Conclusion

In this dissertation, we first discussed the existing motion estimation methods using tagged MRI for cardiac analysis and their intrinsic limitations. Then we improved and extended a computer-assisted phase unwrapping method (caSUP) for biventricular strain analysis, that optimizes the branch cut configuration based on an area preserving assumption for the interframe deformation. Although manual intervention has been reduced significantly by using this method, the computational efficiency is relatively low.

In the following chapter, we proposed a new phase unwrapping method for unwrapping the HARP images using an integer optimization technique (SUPIO). We further improved this method by incorporating a cardiac dynamic model. The Kalman filter predicts unwrapped phases for the following time frame and was shown to be beneficial especially for RV region unwrapping. Resulted demodulated HARP image sequence can achieve both spatial and temporal smoothness. Also, due to the Kalman filter prediction step, we can evaluate the unwrapped phase image to see whether there is any unwrapping errors by checking the difference between computed unwrapped phases and predicted phase values.

Besides this unwrapped phase-based method for motion estimation, we also proposed a tag point classification algorithm (PCGC) for the feature-based analysis. The tag point features were first detected with a bank of Gabor filters. Then the tag point classification problem was solved by optimizing the labeling for the set of all tag points based on a spatial smoothness priori. Configurations corresponding to large displacements were penalized in order to regularize and stabilize the solution. The labeling optimization was similar to the integer optimization problem of the SUPIO method and could be solved with the same graph cuts method. Because the deformation of the myocardium can be potential large, and the small deformation assumption made by the PCGC algorithm was therefore violated, we introduced a motion compensation technique that compensated 1D displacements using the dense displacement field calculated from the previous time frame. The proposed method was validated with *in-vivo* data.

In Table 9.1 we summarize some of the characteristics of the three proposed methods introduced in previous chapters: caSUP for computer-assisted Strain from Unwrapped Phase, SUPIO for Strain from Unwrapped Phase with Integer Optimization, and PCGC for Point Classification with Graph Cuts. This table includes the segmentation method they used and the time required for contouring and propagation, the time for automated processing, the error correction rate and time, the strain reconstruction method and time, and the accuracy of the key strain parameters after reconstruction. We compared their performances on the same biventricular dataset with the same strain reconstruction method (DMF). We can see that SUPIO is similar to PCGC in regard of the accuracy of strain reconstruction (note that the PCGC method did not include an error correction step) and both of these two outperform the caSUP method, in the sense of both speed and accuracy.

Although the SUPIO and PCGC methods may seem distinct, the basic ideas behind them are identical, which are to convert the computation of the feature tracking or correspondence into a combinatorial optimization problem, in which the wrap count field (SUPIO) or the integer label set (PCGC) is optimized based on a spatial smoothness and temporal smoothness priori. For both the methods, the same graph cuts method was applied to the optimization and a max-flow/min-cut algorithm was utilized for computational efficiency.

Despite these similarities, the differences are apparent. First, in SUPIO, the unwrapped phase was modeled with a first-order Markov random field framework, and the clique was defined with a 4-connected system of the pixel grid. In PCGC, the first-order clique was defined with a neighborhood of wider range, because the detected tag points are relatively sparser than the pixel points. The frequency map from the Gabor filter bank was used

Table 9.1: Summary of the three motion estimation methods: caSUP, SUPIO and PCGC for a typical biventricular tMRI study. Strain reconstruction accuracy is evaluated with the coefficient of variance (CV) reported in previous chapters. Key parameters are chosen to be $E_{\min}$, $E_{\min}RV$, and $Twist$. CV for ES strain differences between proposed methods and the feature-based method (FB) or the manual unwrapped phase-based method (mSUP) are shown below. CV for the peak values, systolic rates, and early diastolic rates of some key parameters are also shown by comparing to mSUP. Notice that the PCGC method has no error correction after the automated processing.

Motion estimation	caSUP	SUPIO	PCGC
Segmentation	Dual contour propagation	Dual contour propagation	Dual contour propagation
	30 min	30 min	30 min
Automated processing time	60 min	5 min	14 min
Error correction (rate and time)	4%	4%	N/A
	5 min	10 min	N/A
Strain reconstruction	DMF	DMF	DMF
	30 min	30 min	30 min
CV of $E_{\min}$ (FB)	1.81%	1.48%	0.70%
CV of $E_{\min}RV$ (FB)	2.48%	1.84%	1.32%
CV of $Twist$ (FB)	4.07%	3.38%	1.61%
CV of $E_{\min}$ (mSUP)	1.67%	0.73%	N/A
CV of $E_{\min}RV$ (mSUP)	2.69%	1.19%	N/A
CV of $Twist$ (mSUP)	3.79%	2.04%	N/A
CV of $E_{\min}$ peak	1.42%	0.89%	1.55%
CV of $E_{\min}$ Sys rate	2.22%	2.59%	3.42%
CV of $E_{\min}$ E Dia rate	7.07%	5.67%	5.46%
CV of $E_{\min}RV$ peak	2.11%	1.41%	1.94%
CV of $E_{\min}RV$ Sys rate	8.92%	7.04%	7.40%
CV of $E_{\min}RV$ E Dia rate	8.53%	7.77%	10.76%
CV of $Twist$ peak	3.65%	1.65%	3.37%
CV of $Twist$ Sys rate	4.13%	2.28%	8.05%
CV of $Twist$ E Dia rate	14.19%	6.55%	7.90%

to adjust the neighborhood and the membership weights for PCGC, while for SUPIO the neighborhood system did not change throughout the time sequence. Second, for SUPIO the wrap counts were optimized for spatial points (pixels), while PCGC optimized the labels for material points (tag points). Third, because a motion compensation technique was used for the PCGC method in order to process tagged images with large deformation, the computation time was lengthened. Finally, since the candidate wrap count in SUPIO was not limited for phase unwrapping, the iteration scheme had to involve a pair of *up* and *down* operations. On the other hand, the label set range in PCGC is limited and therefore the *down* operation was not needed. According to our observations, the PCGC method can provide more accurate motion field with large interframe deformation, partly because PCGC is optimizing the label set for the material tag points, instead of spatial pixels, and the neighborhood system is boarder and more robust than that of the SUPIO method. Also, the SUPIO method is currently limited to cardiac application because we used a cardiac dynamic model for Kalman filter prediction. However, SUPIO is a lot faster than PCGC, and can be potentially applied to other phase unwrapping problems in cardiac imaging, like DENSE and phase contrast imaging.

The proposed two motion estimation methods were applied to the cardiac strain computation and the ophthalmic dynamics analysis. In the last two chapters, dynamics of the extraocular muscle (right lateral rectus) and the vitreous humour under eye movements have been studied. From these researches, we found tagged MRI to be a powerful tool for non-invasive deformation measurements. Contrary to the inability of investigating the relative motion within the tissue using traditional anatomical imaging techniques, Tagged MRI can provide motion pattern with high spatial resolution, especially with the help of high field MRI scanner.

9.2 Directions for Future Work

A potential future work can be the application of SUPIO method to other phase imaging techniques like DENSE. Most current methods for unwrapping DENSE images still use path dependent unwrapping and is therefore sensitive to phase inconsistensies. With the proposed SUPIO method the phase image will be optimized globally in the sense of spatial and temporal smoothness and the computation is fast. Another potential research work is to optimize the tag point detection algorithm in the PCGC method. Current tag point location is pixel-wise, but a subpixel accuracy can bring less error. This can be done by spatially matching the tag point location to the local intensity valley after classification completes.

Bibliography

[1] Khaled Z. Abd-Elmoniem, Nael F. Osman, Jerry L. Prince, and Matthias Stuber. Three-dimensional magnetic resonance myocardial motion tracking from a single image plane. *Magnetic Resonance in Medicine*, 58(1):92–102, July 2007.

[2] Khaled Z. Abd-Elmoniem, Smita Sampath, Nael F. Osman, and Jerry L. Prince. Real-time monitoring of cardiac regional function using fastHARP MRI and region-of-interest reconstruction. *IEEE Transactions on Biomedical Engineering*, 54(9):1650–1656, September 2007.

[3] Khaled Z. Abd-Elmoniem, Matthias Stuber, Nael F. Osman, and Jerry L. Prince. ZHARP: three-dimensional motion tracking from a single image plane. *Inf Process Med Imaging*, 19:639–651, 2005.

[4] Omid Abouali, Amirreza Modareszadeh, Alireza Ghaffariyeh, and Jiyuan Tu. Numerical simulation of the fluid dynamics in vitreous cavity due to saccadic eye movement. *Medical Engineering & Physics*, 34(6):681–692, July 2012.

[5] Mustafa I Ahmed, Inmaculada Aban, Steven G Lloyd, Himanshu Gupta, George Howard, Seidu Inusah, Kalyani Peri, Jessica Robinson, Patty Smith, David C McGiffin, Chun G Schiros, Thomas Jr Denney, and Louis J Dell'Italia. A randomized controlled phase IIb trial of beta(1)-receptor blockade for chronic degenerative mitral regurgitation. *J Am Coll Cardiol*, 60(9):833–838, Aug 2012.

[6] Mustafa I Ahmed, Ravi V Desai, Krishna K Gaddam, Bharath A Venkatesh, Shilpi Agarwal, Seidu Inusah, Steven G Lloyd, Thomas S Jr Denney, David Calhoun, Louis J

Dell'italia, and Himanshu Gupta. Relation of torsion and myocardial strains to LV ejection fraction in hypertension. *JACC Cardiovasc Imaging*, 5(3):273–281, Mar 2012.

[7] Mustafa I Ahmed, James D Gladden, Silvio H Litovsky, Steven G Lloyd, Himanshu Gupta, Seidu Inusah, Thomas Jr Denney, Pamela Powell, David C McGiffin, and Louis J Dell'Italia. Increased oxidative stress and cardiomyocyte myofibrillar degeneration in patients with chronic isolated mitral regurgitation and ejection fraction $> 60\%$. *J Am Coll Cardiol*, 55(7):671–679, Feb 2010.

[8] Martino Alessandrini, Adrian Basarab, Herve Liebgott, and Olivier Bernard. Myocardial motion estimation from medical images using the monogenic signal. *IEEE Transactions on Image Processing*, 22(3):1084–1095, March 2013.

[9] Anthony H. Aletras, Shujun Ding, Robert S. Balaban, and Han Wen. DENSE: Displacement encoding with stimulated echoes in cardiac functional MRI. *Journal of Magnetic Resonance*, 137(1):247–252, March 1999.

[10] B. Ambale, T.S. Denney, H. Gupta, S. Lloyd, and L. Dell'Italia. 3d left ventricular strain by phase unwrapping: A simulated annealing based branch-cut placement method. In *IEEE International Symposium on Biomedical Imaging: From Nano to Macro, 2009*, pages 466–469, June 2009.

[11] A. A. Amini, Y. Chen, R. W. Curwen, V. Mani, and J. Sun. Coupled B-snake grids and constrained thin-plate splines for analysis of 2-D tissue deformations from tagged MRI. *IEEE Transactions on Medical Imaging*, 17(3):344–356, June 1998.

[12] A. A. Amini, Y. Chen, M. Elayyadi, and P. Radeva. Tag surface reconstruction and tracking of myocardial beads from SPAMM-MRI with parametric B-spline surfaces. *IEEE Transactions on Medical Imaging*, 20(2):94–103, February 2001.

[13] A. A. Amini and Jerry L. Prince. *Measurement of Cardiac Deformations from MRI: Physical and Mathematical Models.* Springer Science & Business Media, December 2001.

[14] Amir A. Amini, Rupert W. Curwen, and John C. Gore. Snakes and splines for tracking non-rigid heart motion. In Bernard Buxton and Roberto Cipolla, editors, *Computer Vision - ECCV '96*, number 1065 in Lecture Notes in Computer Science, pages 249–261. Springer Berlin Heidelberg, January 1996.

[15] T. Arts, Frits W. Prinzen, T. Delhaas, J. R. Milles, Alessandro C. Rossi, and Patrick Clarysse. Mapping displacement and deformation of the heart with local sine-wave modeling. *IEEE Transactions on Medical Imaging*, 29(5):1114–1123, May 2010.

[16] L Axel and L Dougherty. MR imaging of motion with spatial modulation of magnetization. *Radiology*, 171(3):841–845, June 1989.

[17] Clerio F. Azevedo, Luciano C. Amado, Dara L. Kraitchman, Bernhard L. Gerber, Nael F. Osman, Carlos E. Rochitte, Thor Edvardsen, and Joao A. C. Lima. Persistent diastolic dysfunction despite complete systolic functional recovery after reperfused acute myocardial infarction demonstrated by tagged magnetic resonance imaging. *European Heart Journal*, 25(16):1419–1427, August 2004.

[18] Yaakov Bar-Shalom, X. Rong Li, and Thiagalingam Kirubarajan. *Estimation with Applications to Tracking and Navigation: Theory Algorithms and Software.* Wiley, 2001.

[19] J. Gordon Betts. *Anatomy and Physiology.* OpenStax College, Rice University, 2013.

[20] Jose M. Bioucas-Dias and Goncalo Valadao. Phase unwrapping via graph cuts. *IEEE Transactions on Image Processing*, 16(3):698–709, March 2007.

[21] P. N. Bishop. Structural macromolecules and supramolecular organisation of the vitreous gel. *Progress in Retinal and Eye Research*, 19(3):323–344, May 2000.

[22] Endre Boros and Peter L. Hammer. Pseudo-boolean optimization. *Discrete Appl. Math.*, 123(1-3):155–225, November 2002.

[23] Y. Boykov and V. Kolmogorov. An experimental comparison of min-cut/max- flow algorithms for energy minimization in vision. *IEEE Transactions on Pattern Analysis and Machine Intelligence*, 26(9):1124–1137, September 2004.

[24] G. Buchsbaum, M. Sternklar, M. Litt, J. E. Grunwald, and C. E. Riva. Dynamics of an oscillating viscoelastic sphere: a model of the vitreous humor of the eye. *Biorheology*, 21(1-2):285–296, 1984.

[25] N. Carranza-Herrezuelo, A. Bajo, F. Sroubek, C. Santamarta, G. Cristobal, A. Santos, and M. J. Ledesma-Carbayo. Motion estimation of tagged cardiac magnetic resonance images using variational techniques. *Computerized Medical Imaging and Graphics*, 34(6):514–522, September 2010.

[26] M. D. Cerqueira, N. J. Weissman, V. Dilsizian, A. K. Jacobs, S. Kaul, W. K. Laskey, D. J. Pennell, J. A. Rumberger, T. Ryan, and M. S. Verani. Standardized myocardial segmentation and nomenclature for tomographic imaging of the heart: A statement for healthcare professionals from the cardiac imaging committee of the Council on Clinical Cardiology of the American Heart Association. *Circulation*, 105(4):539–542, 2002.

[27] Raghavendra Chandrashekara, Raad H. Mohiaddin, and Daniel Rueckert. Analysis of 3-D myocardial motion in tagged MR images using nonrigid image registration. *IEEE Transactions on Medical Imaging*, 23(10):1245–1250, October 2004.

[28] Ting Chen and Leon Axel. Using Gabor filter banks and temporal-spatial constraints to compute 3D myocardium strain. *Conf Proc IEEE Eng Med Biol Soc*, 1:4755–4758, 2006.

[29] Ting Chen, Xiaoxu Wang, Sohae Chung, Dimitris Metaxas, and Leon Axel. Automated 3d motion tracking using Gabor filter bank, robust point matching, and deformable models. *IEEE Transactions on Medical Imaging*, 29(1):1–11, January 2010.

[30] Ting Chen, Xiaoxu Wang, Dimitris Metaxas, and Leon Axel. Fast motion tracking of tagged MRI using angle-preserving meshless registration. *Medical Image Computing and Computer Assisted Intervention: MICCAI*, 11(Pt 2):313–320, 2008.

[31] Yasheng Chen and Amir A. Amini. A MAP framework for tag line detection in SPAMM data using Markov random fields on the B-spline solid. *IEEE Transactions on Medical Imaging*, 21(9):1110–1122, September 2002.

[32] Patricia Chiang, Yiyu Cai, Koon Hou Mak, and Jianmin Zheng. A B-spline approach to phase unwrapping in tagged cardiac MRI for motion tracking. *Magnetic Resonance in Medicine*, 69(5):1297–1309, May 2013.

[33] William J. Cook, William H. Cunningham, William R. Pulleyblank, and Alexander Schrijver. *Combinatorial optimization*. Wiley-Interscience, 1997.

[34] T. David, S. Smye, T. Dabbs, and T. James. A model for the fluid motion of vitreous humour of the human eye during saccadic movement. *Physics in Medicine and Biology*, 43(6):1385–1399, June 1998.

[35] J. L. Demer, S. Y. Oh, and V. Poukens. Evidence for active control of rectus extraocular muscle pulleys. *Investigative Ophthalmology & Visual Science*, 41(6):1280–1290, May 2000.

[36] Xiang Deng and Thomas S. Denney. Three-dimensional myocardial strain reconstruction from tagged MRI using a cylindrical B-spline model. *IEEE Transactions on Medical Imaging*, 23(7):861–867, July 2004.

[37] Xiang Deng and Thomas S. Denney. Combined tag tracking and strain reconstruction from tagged cardiac MR images without user-defined myocardial contours. *Journal of Magnetic Resonance Imaging*, 21(1):12–22, January 2005.

[38] T. R. Denney and J. L. Prince. Optimal brightness functions for optical flow estimation of deformable motion. *IEEE Transactions on Image Processing*, 3(2):178–191, 1994.

[39] T. S. Denney. Estimation and detection of myocardial tags in MR image without user-defined myocardial contours. *IEEE Transactions on Medical Imaging*, 18(4):330–344, April 1999.

[40] T. S. Denney and E. R. McVeigh. Model-free reconstruction of three-dimensional myocardial strain from planar tagged MR images. *Journal of Magnetic Resonance Imaging*, 7(5):799–810, October 1997.

[41] Thomas S. Denney, Mark S. Bolding, Ronald J. Beyers, Nouha Salibi, Ming Li, Xiaoxia Zhang, and Paul Gamlin. Differential motion in orbital and global layers of extraocular muscles measured by tagged MRI at 7T. In *22nd Annual Meeting & Exhibition of International Society for Magnetic Resonance in Medicine*, 2014.

[42] T.S. Denney and J.L. Prince. Reconstruction of 3-D left ventricular motion from planar tagged cardiac MR images: an estimation theoretic approach. *IEEE Transactions on Medical Imaging*, 14(4):625–635, December 1995.

[43] A Ray Dillon, Louis J Dell'Italia, Michael Tillson, Cheryl Killingsworth, Thomas Denney, John Hathcock, and Logan Botzman. Left ventricular remodeling in preclinical experimental mitral regurgitation of dogs. *J Vet Cardiol*, 14(1):73–92, Mar 2012.

[44] S. J. Dong, A. P. Crawley, J. H. MacGregor, Y. F. Petrank, D. W. Bergman, I. Belenkie, E. R. Smith, J. V. Tyberg, and R. Beyar. Regional left ventricular systolic function in relation to the cavity geometry in patients with chronic right ventricular pressure

overload. a three-dimensional tagged magnetic resonance imaging study. *Circulation*, 91(9):2359–2370, May 1995.

[45] L. Dougherty, J. C. Asmuth, A. S. Blom, L. Axel, and R. Kumar. Validation of an optical flow method for tag displacement estimation. *IEEE Transactions on Medical Imaging*, 18(4):359–363, April 1999.

[46] Wei Feng, Hosakote Nagaraj, Himanshu Gupta, Steven G. Lloyd, Inmaculada Aban, Gilbert J. Perry, David A. Calhoun, Louis J. Dell'Italia, and Thomas S. Denney. A dual propagation contours technique for semi-automated assessment of systolic and diastolic cardiac function by CMR. *Journal of Cardiovascular Magnetic Resonance*, 11:30, 2009.

[47] S. E. Fischer, G. C. McKinnon, S. E. Maier, and P. Boesiger. Improved myocardial tagging contrast. *Magnetic Resonance in Medicine*, 30(2):191–200, August 1993.

[48] David J. Fleet and A. D. Jepson. Computation of component image velocity from local phase information. *Int. J. Comput. Vision*, 5(1):77–104, September 1990.

[49] L. Florack, H. van Assen, and A. Suinesiaputra. Dense multiscale motion extraction from cardiac cine MR tagging using HARP technology. In *IEEE 11th International Conference on Computer Vision, 2007. ICCV 2007*, pages 1–8, October 2007.

[50] A. F. Frangi, W. J. Niessen, and M. A. Viergever. Three-dimensional modeling for functional analysis of cardiac images: a review. *IEEE Transactions on Medical Imaging*, 20(1):2–25, January 2001.

[51] Dennis C. Ghiglia and Mark D. Pritt. *Two-dimensional phase unwrapping: theory, algorithms, and software.* Wiley, April 1998.

[52] A Gupta, C G Schiros, K K Gaddam, I Aban, T S Denney, S G Lloyd, S Oparil, L J Dell'Italia, D A Calhoun, and H Gupta. Effect of spironolactone on diastolic function

in hypertensive left ventricular hypertrophy. *J Hum Hypertens*, 29(4):241–246, Apr 2015.

[53] B. Gutmann and H. Weber. Phase unwrapping with the branch-cut method: clustering of discontinuity sources and reverse simulated annealing. *Applied Optics*, 38(26):5577–5593, September 1999.

[54] M. A. Guttman, J. L. Prince, and E. R. McVeigh. Tag and contour detection in tagged MR images of the left ventricle. *IEEE Transactions on Medical Imaging*, 13(1):74–88, 1994.

[55] Michael A. Guttman, E.A. Zerhouni, and E.R. McVeigh. Analysis of cardiac function from MR images. *IEEE Computer Graphics and Applications*, 17(1):30–38, January 1997.

[56] I. Haber, D. N. Metaxas, and L. Axel. Three-dimensional motion reconstruction and analysis of the right ventricle using tagged MRI. *Medical Image Analysis*, 4(4):335–355, December 2000.

[57] P. L. Hammer, P. Hansen, and B. Simeone. Roof duality, complementation and persistency in quadratic 0-1 optimization. *Mathematical Programming*, 28(2):121–155, February 1984.

[58] J. Huang, D. Abendschein, V. G. Davila-Roman, and A. A. Amini. Spatio-temporal tracking of myocardial deformations with a 4-D B-spline model from tagged MRI. *IEEE Transactions on Medical Imaging*, 18(10):957–972, October 1999.

[59] William S. Kerwin and Jerry L. Prince. Cardiac material markers from tagged MR images. *Medical Image Analysis*, 2(4):339–353, December 1998.

[60] Ayman Khalifa, A. B. M. Youssef, and Nael Osman. Improved harmonic phase (HARP) method for motion tracking a tagged cardiac MR images. *Conf Proc IEEE Eng Med Biol Soc*, 4:4298–4301, 2005.

[61] Richard Klabunde. *Cardiovascular Physiology Concepts.* Lippincott Williams & Wilkins, November 2011.

[62] V. Kolmogorov and C. Rother. Minimizing nonsubmodular functions with graph cuts-a review. *IEEE Transactions on Pattern Analysis and Machine Intelligence*, 29(7):1274–1279, July 2007.

[63] V. Kolmogorov and R. Zabin. What energy functions can be minimized via graph cuts? *IEEE Transactions on Pattern Analysis and Machine Intelligence*, 26(2):147–159, February 2004.

[64] Vladimir Kolmogorov. Primal-dual algorithm for convex Markov random fields. Technical report, Microsoft Research MSR-TR-2005-117, 2005.

[65] Maria J. Ledesma-Carbayo, J. Andrew Derbyshire, Smita Sampath, Andres Santos, Manuel Desco, and Elliot R. McVeigh. Unsupervised estimation of myocardial displacement from tagged MR sequences using nonrigid registration. *Magnetic Resonance in Medicine*, 59(1):181–189, January 2008.

[66] B. Lee, M. Litt, and G. Buchsbaum. Rheology of the vitreous body. Part I: Viscoelasticity of human vitreous. *Biorheology*, 29(5-6):521–533, December 1992.

[67] R. John Leigh and David S. Zee. *The Neurology of Eye Movements.* Oxford University Press, 2006.

[68] Jin Li and Thomas S. Denney. Left ventricular motion reconstruction with a prolate spheroidal B-spline model. *Physics in Medicine and Biology*, 51(3):517–537, February 2006.

[69] Ming Li, Paul Gamlin, Mark S. Bolding, Ronald J. Beyers, Nouha Salibi, Xiaoxia Zhang, and Thomas S. Denney. Measurement of the vitreous humour deformation and strain with tagged MR imaging. In *23rd Annual Meeting & Exhibition of International Society for Magnetic Resonance in Medicine*, 2015.

[70] Ming Li, Himanshu Gupta, Steven G. Lloyd, Louis J. Dell'Italia, and Thomas S. Denney. 3D+time left ventricular strain by unwrapping harmonic phase with graph cuts. *Medical Image Computing and Computer Assisted Intervention: MICCAI*, 17(Pt 2):578–585, 2014.

[71] Ming Li, Himanshu Gupta, Steven G. Lloyd, Louis J. Dell'Italia, and Thomas S. Denney. An integer optimization technique for measuring biventricular cardiac strain from tagged MR images. In *23rd Annual Meeting & Exhibition of International Society for Magnetic Resonance in Medicine*, 2015.

[72] Ming Li, Bharath Ambale Venkatesh, Himanshu Gupta, Steven G. Lloyd, Louis J. Dell'Italia, and Thomas S. Denney. Computer assisted branch cut placement for computing 3D+t biventricular strain from tagged MRI. In *21st Annual Meeting & Exhibition of International Society for Magnetic Resonance in Medicine*, 2013.

[73] Hong Liu, Jie Wang, Xiangyang Xu, Enmin Song, Qian Wang, Renchao Jin, Chih-Cheng Hung, and Baowei Fei. A robust and accurate center-frequency estimation (RACE) algorithm for improving motion estimation performance of SinMod on tagged cardiac MR images without known tagging parameters. *Magnetic Resonance Imaging*, 32(9):1139–1155, November 2014.

[74] Wei Liu, Junjie Chen, Songbai Ji, J. Stacy Allen, Philip V. Bayly, Samuel A. Wickline, and Xin Yu. Harmonic phase MR tagging for direct quantification of Lagrangian strain in rat hearts after myocardial infarction. *Magnetic Resonance in Medicine*, 52(6):1282–1290, December 2004.

[75] Xiaofeng Liu, Khaled Z. Abd-Elmoniem, Maureen Stone, Emi Z. Murano, Jiachen Zhuo, Rao P. Gullapalli, and Jerry L. Prince. Incompressible deformation estimation algorithm (IDEA) from tagged MR images. *IEEE Transactions on Medical Imaging*, 31(2):326–340, February 2012.

[76] Timo Makela, Patrick Clarysse, Outi Sipila, Nicoleta Pauna, Quoc Cuong Pham, Toivo Katila, and Isabelle E. Magnin. A review of cardiac image registration methods. *IEEE Transactions on Medical Imaging*, 21(9):1011–1021, September 2002.

[77] R. Mankad, C. J. McCreery, W. J. Rogers, R. J. Weichmann, E. B. Savage, N. Reichek, and C. M. Kramer. Regional myocardial strain before and after mitral valve repair for severe mitral regurgitation. *Journal of Cardiovascular Magnetic Resonance*, 3(3):257–266, 2001.

[78] E. R. McVeigh, F. W. Prinzen, B. T. Wyman, J. E. Tsitlik, H. R. Halperin, and W. C. Hunter. Imaging asynchronous mechanical activation of the paced heart with tagged MRI. *Magnetic Resonance in Medicine*, 39(4):507–513, April 1998.

[79] Christopher A. Miller, Alex Borg, David Clark, Christopher D. Steadman, Gerry P. McCann, Patrick Clarysse, Pierre Croisille, and Matthias Schmitt. Comparison of local sine wave modeling with harmonic phase analysis for the assessment of myocardial strain. *Journal of Magnetic Resonance Imaging*, 38(2):320–328, August 2013.

[80] Joel M. Miller. Functional anatomy of normal human rectus muscles. *Vision Research*, 29(2):223–240, 1989.

[81] Joel M. Miller. Understanding and misunderstanding extraocular muscle pulleys. *Journal of Vision*, 7(11):10.1–15, 2007.

[82] Joel M. Miller and David A. Robinson. A model of the mechanics of binocular alignment. *Computers and Biomedical Research*, 17(5):436–470, October 1984.

[83] E. Nagel, M. Stuber, M. Lakatos, M. B. Scheidegger, P. Boesiger, and O. M. Hess. Cardiac rotation and relaxation after anterolateral myocardial infarction. *Coronary Artery Disease*, 11(3):261–267, May 2000.

[84] Charles S. Nickerson, John Park, Julia A. Kornfield, and Hampar Karageozian. Rheological properties of the vitreous and the role of hyaluronic acid. *Journal of Biomechanics*, 41(9):1840–1846, 2008.

[85] N. F. Osman, W. S. Kerwin, E. R. McVeigh, and J. L. Prince. Cardiac motion tracking using CINE harmonic phase (HARP) magnetic resonance imaging. *Magnetic Resonance in Medicine*, 42(6):1048–1060, December 1999.

[86] N. F. Osman, E. R. McVeigh, and J. L. Prince. Imaging heart motion using harmonic phase MRI. *IEEE Transactions on Medical Imaging*, 19(3):186–202, March 2000.

[87] N. F. Osman, S. Sampath, E. Atalar, and J. L. Prince. Imaging longitudinal cardiac strain on short-axis images using strain-encoded MRI. *Magnetic Resonance in Medicine*, 46(2):324–334, August 2001.

[88] Li Pan, Jerry L. Prince, Joo A. C. Lima, and Nael F. Osman. Fast tracking of cardiac motion using 3D-HARP. *IEEE Transactions on Biomedical Engineering*, 52(8):1425–1435, August 2005.

[89] J. Park, D. Metaxas, and L. Axel. Analysis of left ventricular wall motion based on volumetric deformable models and MRI-SPAMM. *Medical Image Analysis*, 1(1):53–71, March 1996.

[90] Betty Pat, Yuanwen Chen, Cheryl Killingsworth, James D Gladden, Ke Shi, Junying Zheng, Pamela C Powell, Greg Walcott, Mustafa I Ahmed, Himanshu Gupta, Ravi Desai, Chih-Chang Wei, Naoki Hase, Tsunefumi Kobayashi, Abdelkarim Sabri, Henk Granzier, Thomas Denney, Michael Tillson, A Ray Dillon, Ahsan Husain, and Louis J

Dell'italia. Chymase inhibition prevents fibronectin and myofibrillar loss and improves cardiomyocyte function and LV torsion angle in dogs with isolated mitral regurgitation. *Circulation*, 122(15):1488–1495, Oct 2010.

[91] Marco Piccirelli, Oliver Bergamin, Klara Landau, Peter Boesiger, and Roger Luechinger. Vitreous deformation during eye movement. *NMR in Biomedicine*, 25(1):59–66, January 2012.

[92] Marco Piccirelli, Roger Luechinger, Andrea K. Rutz, Peter Boesiger, and Oliver Bergamin. Extraocular muscle deformation assessed by motion-encoded MRI during eye movement in healthy subjects. *Journal of Vision*, 7(14):5.1–10, 2007.

[93] Marco Piccirelli, Roger Luechinger, Veit Sturm, Peter Boesiger, Klara Landau, and Oliver Bergamin. Local deformation of extraocular muscles during eye movement. *Investigative Ophthalmology & Visual Science*, 50(11):5189–5196, November 2009.

[94] J. L. Prince and E. R. McVeigh. Motion estimation from tagged MR image sequences. *IEEE Transactions on Medical Imaging*, 11(2):238–249, 1992.

[95] K. Punithakumar, I. Ben Ayed, A. Islam, I.G. Ross, and Shuo Li. Tracking endocardial motion via multiple model filtering. *IEEE Transactions on Biomedical Engineering*, 57(8):2001–2010, August 2010.

[96] K. Punithakumar, I. Ben Ayed, I.G. Ross, A. Islam, J. Chong, and Shuo Li. Detection of left ventricular motion abnormality via information measures and Bayesian filtering. *IEEE Transactions on Information Technology in Biomedicine*, 14(4):1106–1113, July 2010.

[97] Zhen Qian, Dimitris N. Metaxas, and Leon Axel. A learning framework for the automatic and accurate segmentation of cardiac tagged MRI images. In Yanxi Liu, Tianzi

Jiang, and Changshui Zhang, editors, *Computer Vision for Biomedical Image Applications*, number 3765 in Lecture Notes in Computer Science, pages 93–102. Springer Berlin Heidelberg, January 2005.

[98] Zhen Qian, Dimitris N. Metaxas, and Leon Axel. Boosting and nonparametric based tracking of tagged MRI cardiac boundaries. *Medical Image Computing and Computer Assisted Intervention: MICCAI*, 9(Pt 1):636–644, 2006.

[99] Zhen Qian, Dimitris N. Metaxas, and Leon Axel. Extraction and tracking of MRI tagging sheets using a 3D Gabor filter bank. *Conf Proc IEEE Eng Med Biol Soc*, 1:711–714, 2006.

[100] Zhen Qian, A Montillo, D.N. Metaxas, and L. Axel. Segmenting cardiac MRI tagging lines using Gabor filter banks. In *Conf Proc IEEE Eng Med Biol Soc*, volume 1, pages 630–633 Vol.1, September 2003.

[101] P. Radeva, A. Amini, Jiantao Huang, and E. Marti. Deformable B-solids and implicit snakes for localization and tracking of SPAMM MRI-data. In *Proceedings of the Workshop on Mathematical Methods in Biomedical Image Analysis, 1996*, pages 192–201, June 1996.

[102] R. Repetto, J. H. Siggers, and A. Stocchino. Mathematical model of flow in the vitreous humor induced by saccadic eye rotations: effect of geometry. *Biomechanics and Modeling in Mechanobiology*, 9(1):65–76, February 2010.

[103] D. A. Robinson. A quantitative analysis of extraocular muscle cooperation and squint. *Investigative Ophthalmology*, 14(11):801–825, November 1975.

[104] D. Rueckert, L. I. Sonoda, C. Hayes, D. L. Hill, M. O. Leach, and D. J. Hawkes. Nonrigid registration using free-form deformations: application to breast MR images. *IEEE Transactions on Medical Imaging*, 18(8):712–721, August 1999.

[105] Andrea K. Rutz, Salome Ryf, Sven Plein, Peter Boesiger, and Sebastian Kozerke. Accelerated whole-heart 3D CSPAMM for myocardial motion quantification. *Magnetic Resonance in Medicine*, 59(4):755–763, April 2008.

[106] Salome Ryf, Marcus A. Spiegel, Michael Gerber, and Peter Boesiger. Myocardial tagging with 3D-CSPAMM. *Journal of magnetic resonance imaging*, 16(3):320–325, September 2002.

[107] Smita Sampath, J. Andrew Derbyshire, Ergin Atalar, Nael F. Osman, and Jerry L. Prince. Real-time imaging of two-dimensional cardiac strain using a harmonic phase magnetic resonance imaging (HARP-MRI) pulse sequence. *Magnetic Resonance in Medicine*, 50(1):154–163, July 2003.

[108] Smita Sampath, Nael F. Osman, and Jerry L. Prince. A combined harmonic phase and strain-encoded pulse sequence for measuring three-dimensional strain. *Magnetic Resonance Imaging*, 27(1):55–61, January 2009.

[109] Smita Sampath and Jerry L. Prince. Automatic 3D tracking of cardiac material markers using slice-following and harmonic-phase MRI. *Magnetic Resonance Imaging*, 25(2):197–208, February 2007.

[110] Chun G Schiros, Louis J Dell'Italia, James D Gladden, Donald 3rd Clark, Inmaculada Aban, Himanshu Gupta, Steven G Lloyd, David C McGiffin, Gilbert Perry, Thomas S Jr Denney, and Mustafa I Ahmed. Magnetic resonance imaging with 3-dimensional analysis of left ventricular remodeling in isolated mitral regurgitation: implications beyond dimensions. *Circulation*, 125(19):2334–2342, May 2012.

[111] Chun G Schiros, Ravi V Desai, Bharath Ambale Venkatesh, Krishna K Gaddam, Shilpi Agarwal, Steven G Lloyd, David A Calhoun, Thomas S Jr Denney, Louis J Dell'italia, and Himanshu Gupta. Left ventricular torsion shear angle volume analysis in patients

with hypertension: a global approach for LV diastolic function. *J Cardiovasc Magn Reson*, 16:70, 2014.

[112] Robert Sekuler, Key Dismukes, Donald Kline, and National Research Council (U S.) Committee on Vision. *Aging and human visual function.* A.R. Liss, 1982.

[113] Ihor Smal, Noemi Carranza-Herrezuelo, Stefan Klein, Piotr Wielopolski, Adriaan Moelker, Tirza Springeling, Monique Bernsen, Wiro Niessen, and Erik Meijering. Reversible jump MCMC methods for fully automatic motion analysis in tagged MRI. *Medical Image Analysis*, 16(1):301–324, January 2012.

[114] B. S. Spottiswoode, X. Zhong, A. T. Hess, C. M. Kramer, E. M. Meintjes, B. M. Mayosi, and Frederick H. Epstein. Tracking myocardial motion from cine DENSE images using spatiotemporal phase unwrapping and temporal fitting. *IEEE Transactions on Medical Imaging*, 26(1):15–30, January 2007.

[115] Bruce S. Spottiswoode, Xiaodong Zhong, Christine H. Lorenz, Bongani M. Mayosi, Ernesta M. Meintjes, and Frederick H. Epstein. 3D myocardial tissue tracking with slice followed cine DENSE MRI. *Journal of Magnetic Resonance Imaging*, 27(5):1019–1027, May 2008.

[116] Alessandro Stocchino, Rodolfo Repetto, and Chiara Cafferata. Eye rotation induced dynamics of a Newtonian fluid within the vitreous cavity: the effect of the chamber shape. *Physics in Medicine and Biology*, 52(7):2021–2034, April 2007.

[117] Katelyn E. Swindle, Paul D. Hamilton, and Nathan Ravi. In situ formation of hydrogels as vitreous substitutes: Viscoelastic comparison to porcine vitreous. *Journal of Biomedical Materials Research. Part A*, 87(3):656–665, December 2008.

[118] Sandra R. R. Tecelao, Jaco J. M. Zwanenburg, Joost P. A. Kuijer, and J. Tim Marcus. Extended harmonic phase tracking of myocardial motion: improved coverage of

myocardium and its effect on strain results. *Journal of Magnetic Resonance Imaging*, 23(5):682–690, May 2006.

[119] Nicholas J. Tustison and Amir A. Amini. Biventricular myocardial strains via nonrigid registration of anatomical NURBS model [corrected]. *IEEE Transactions on Medical Imaging*, 25(1):94–112, January 2006.

[120] Bharath Ambale Venkatesh, Himanshu Gupta, Steven G. Lloyd, Louis Dell 'Italia, and Thomas S. Denney. 3D left ventricular strain from unwrapped harmonic phase measurements. *Journal of Magnetic Resonance Imaging*, 31(4):854–862, April 2010.

[121] Bharath Ambale Venkatesh, Chun G. Schiros, Himanshu Gupta, Steven G. Lloyd, Louis Dell'Italia, and Thomas S. Denney. Three-dimensional plus time biventricular strain from tagged MR images by phase-unwrapped harmonic phase. *Journal of Magnetic Resonance Imaging*, 34(4):799–810, October 2011.

[122] L. K. Waldman, D. Nosan, F. Villarreal, and J. W. Covell. Relation between transmural deformation and local myofiber direction in canine left ventricle. *Circulation Research*, 63(3):550–562, September 1988.

[123] Kelly A. Walton, Carsten H. Meyer, Curtis J. Harkrider, Terry A. Cox, and Cynthia A. Toth. Age-related changes in vitreous mobility as measured by video B scan ultrasound. *Experimental Eye Research*, 74(2):173–180, February 2002.

[124] Hui Wang and Amir A. Amini. Cardiac motion and deformation recovery from MRI: a review. *IEEE Transactions on Medical Imaging*, 31(2):487–503, February 2012.

[125] Xiaoxu Wang, Ting Chen, Shaoting Zhang, Dimitris Metaxas, and Leon Axel. LV motion and strain computation from tMRI based on meshless deformable models. *Medical Image Computing and Computer Assisted Intervention: MICCAI*, 11(Pt 1):636–644, 2008.

[126] Xiaoxu Wang, Ting Chen, Shaoting Zhang, Joel Schaerer, Zhen Qian, Suejung Huh, Dimitris Metaxas, and Leon Axel. Meshless deformable models for 3D cardiac motion and strain analysis from tagged MRI. *Magnetic Resonance Imaging*, 33(1):146–160, January 2015.

[127] www.aireurbano.com 2015. Human heart diagram labeled. http://www.aireurbano.com/human-heart-diagram-labeled/human-heart-diagram-labeled/, May 2014.

[128] www.harvard-wm.org 2015. Eyes anatomy and how they work. http://www.harvard-wm.org/the-body-of-the-eye-model-human-model-anatomy/eyes-anatomy-and-how-they-work/#, October 2014.

[129] Chun Xu, James J. Pilla, Gamaliel Isaac, Joseph H. Gorman, Aaron S. Blom, Robert C. Gorman, Zhou Ling, and Lawrence Dougherty. Deformation analysis of 3D tagged cardiac images using an optical flow method. *Journal of Cardiovascular Magnetic Resonance*, 12:19, 2010.

[130] Lei Ying, Zhi-Pei Liang, David C. Munson, Ralf Koetter, and Brendan J. Frey. Unwrapping of MR phase images using a Markov random field model. *IEEE Transactions on Medical Imaging*, 25(1):128–136, January 2006.

[131] A. A. Young. Model tags: direct three-dimensional tracking of heart wall motion from tagged magnetic resonance images. *Medical Image Analysis*, 3(4):361–372, December 1999.

[132] A. A. Young and B. R. Cowan. Evaluation of left ventricular torsion by cardiovascular magnetic resonance. *Journal of Cardiovascular Magnetic Resonance*, 14:49, 2012.

[133] A. A. Young, S. Dokos, K. A. Powell, B. Sturm, A. D. McCulloch, R. C. Starling, P. M. McCarthy, and R. D. White. Regional heterogeneity of function in nonischemic dilated cardiomyopathy. *Cardiovascular Research*, 49(2):308–318, February 2001.

[134] A. A. Young, C. M. Kramer, V. A. Ferrari, L. Axel, and N. Reichek. Three-dimensional left ventricular deformation in hypertrophic cardiomyopathy. *Circulation*, 90(2):854–867, August 1994.

[135] Alistair A. Young. Assessment of cardiac performance with magnetic resonance imaging. *Current Cardiology Reviews*, 2(4):271–282, November 2006.

[136] E A Zerhouni, D M Parish, W J Rogers, A Yang, and E P Shapiro. Human heart: tagging with MR imaging–a method for noninvasive assessment of myocardial motion. *Radiology*, 169(1):59–63, October 1988.

[137] Wei Zha, Chun G. Schiros, Gautam Reddy, Wei Feng, Thomas S. Denney, Steven G. Lloyd, Louis J. Dell'Italia, and Himanshu Gupta. Improved right ventricular performance with increased tricuspid annular excursion in athletes heart. *Frontiers in Cardiovascular Medicine*, 2:8, 2015.

[138] R L Zimmerman. In vivo measurements of the viscoelasticity of the human vitreous humor. *Biophysical Journal*, 29(3):539–544, March 1980.